Investigation of Single-Section InAs/InP Quantum Dot Mode-locked Lasers

Zhejing Jiao

A Thesis

In the Department

of

Electrical and Computer Engineering

Presented in Partial Fulfillment of the Requirements

For the Degree of

Doctor of Philosophy (Electrical and Computer Engineering) at

Concordia University

Montreal, Quebec, Canada

September 2014

CONCORDIA UNIVERSITY
SCHOOL OF GRADUATE STUDIES

This is to certify that the thesis prepared

By: Zhejing Jiao

Entitled: Investigation of Single-Section InAs/InP Quantum Dot Mode-Locked Lasers

and submitted in partial fulfillment of the requirements for the degree of

Doctor of Philosophy

complies with the regulations of the University and meets the accepted standards with respect to originality and quality.

Signed by the final examining committee:

Dr. Mingyuan Chen — Chair

Dr. Zetian Mi — External Examiner

Dr. Pablo Bianucci — External to Program

Dr. Zahangir Kabir — Examiner

Dr. Mojtaba Kahrizi — Examiner

Dr. John Xiupu Zhang and Dr. Zhenguo Lu — Thesis Supervisor

Approved by

Dr. Abdel R. Sebak
Chair of Department or Graduate Program Director

September 23rd, 2014

Dr. Amir Asif
Dean of Faculty

ABSTRACT

Investigation of single-section InAs/InP quantum dot mode-locked lasers

Zhejing Jiao, Ph.D.
Concordia University, 2014

The study of mode-locking in generating short pulses began in the 1960s. Since then, the advances have been remarkable over almost 50 years and some of the mode-locked lasers (MLLs) have been commercialized. Short pulses from sub-picoseconds to femtoseconds have been successfully demonstrated from crystal and fiber based lasers. The diverse applications of MLLs have been pushing the development of MLLs in high bit rate transmission, optical time division multiplexed transmission, optical clock recovery, ultrafast signal processing and frequency comb, etc. Semiconductor lasers have advantages of simplicity, compactness and high efficiency. They have attracted interests in the application of optical communications. Until now, semiconductor MLLs are mainly based on bulk and quantum well (QW) structures. More recently, quantum dot (QD) based MLLs have attracted more and more attentions. The main characteristic of QD is the delta-function-like density of states with electrons confined in all three dimensions. It is promising in ultrashort and ultrafast pulse generations as a result of inhomogeneous gain broadening, broad gain bandwidth and fast carrier dynamics. In passive mode-locking, a two-section structure is usually used. A saturable absorber section is essential in the lasing cavity to initiate and shape pulses, which is also the case in almost all QD MLLs. However, without the absorber, passive mode-locking can also

be achieved in single-section QD cavity, which has not been well studied yet. This thesis focuses on investigating single-section InAs/InP QD MLLs. It aims at improving the laser performance by both experimental and theoretical analyses. The following works have been done in this thesis.

Firstly, as an important parameter of all semiconductor lasers, the linewidth enhancement factor is measured using two methods: the Hakki-Pauli method that is used for a laser below threshold and injection-locking technique for a laser above threshold. The results from the two methods agree with each other, and it is found that the linewidth enhancement factor of our QD lasers is much smaller than that of QW based lasers.

Secondly, the time-domain travelling-wave model is used to investigate the single-section QD MLLs. By introducing an equivalent saturable absorber, the pulse generation and evolution are successfully simulated. Furthermore, this model is improved by including the effects of group-velocity dispersion (GVD) and self-phase modulation. It is found that the GVD effect plays an important role in the pulse width evolution of our mode-locked lasers. The improved model can be widely extended to other types of semiconductor lasers and amplifiers.

Thirdly, high-repetition-rate pulse trains of up to 1 THz are generated from a QD laser combined with fiber-Bragg-grating (FBG) external cavities. The QD laser is used for multi-mode gain and several specific modes are selected by the FBGs. The pulse train is measured by using the time-domain autocorrelator, and the repetition rate is in agreement with the frequency spacing of the FBGs. Finally, tunable terahertz beat waves of up to 2.1 THz are generated also using FBG external cavities. This method may find applications for generating microwave, millimeter wave and terahertz wave.

Acknowledgements

I would like to express my sincere gratitude to my supervisor Prof. John X. Zhang for his guidance, advice and financial support for me to finish this thesis.

I would like to thank Dr. Zhenguo Lu and Dr. Jiaren Liu for their help and discussions on experimental lab work at the Information and Communications Technologies, National Research Council, Ottawa, Canada.

I would also like to thank my husband Dr. Rong Zhang for his help, encouragement and company during my PhD study.

Last but not the lease, I am very grateful to my mother for her love and support throughout my life.

Table of Contents

List of Figures

List of Tables

List of Acronyms

ASE	Amplified spontaneous emission
CBE	Chemical Beam Epitaxy
CDP	Carrier density pulsation
CH	Carrier heating
cw	Continuous wave
DDE	Delayed differential equation
DFB	Distributed feedback
DOS	Density of states
ECMLL	External cavity mode-locked laser
EDFA	Erbium-doped fiber amplifer
ES	Excited state
FBG	Fiber-Bragg grating
FCA	Free carrier absorption
fs	Femtosecond
FSR	Free spectral range
FWHM	Full width at half maximum
FWM	Four-wave mixng
GS	Ground state
GVD	Group-velocity dispersion
LD	Laser diode
LEF	Linewidth enhancement factor
MBE	Molecular Beam Epitaxy
MLL	Mode-locked laser
MOCVD	Metal-organic Chemical Vapor Deposition
MOVPE	Metal-organic Vapor Phase Epitaxy
MS-DDE	Multi-section delayed differential equation
MWL	Multi-wavelength laser
OSA	Optical spectrum analyzer
PL	Photoluminescence

PM	Polarization-maintaining
ps	Picosecond
QCL	Quantum cascade laser
QD	Quantum dot
QDash	Quantum dash
QW	Quantum well
RIN	Relative intensity noise
RF	Radio frequency
SA	Saturable absorber
SCH	Separate confinement heterostructure
SESAM	Semiconductor saturable absorber mirror
SHB	Spectral hole burning
SK	Stranski-Krastanow
SMSR	Side-mode suppression ratio
SOA	Semiconductor optical amplifier
SPM	Self-phase modulation
TBP	Time-bandwidth product
TDTW	Time-domain travelling wave
THz	Terahertz
TPA	Two-photon absorption
TW	Travelling-wave
WL	Wetting layer
XPM	Cross-phase modulation

Chapter 1 Introduction to Quantum Dot Mode-Locked Lasers

1.1 Introduction

1.1.1 Density of states in QDs

The word mode-locking describes fixed phase difference among longitudinal modes in a laser cavity. The mode-locking technique is used to generate very short pulses, from a few tens of picoseconds (ps) to femtoseconds (fs). It was first indicated on ruby lasers by Gürs and Müller [1] and on He-Ne lasers by Statz and Tang [2]. Mode-locked lasers are potential candidates for lots of applications in optical communications. Tremendous advances have been achieved in mode-locking over almost five decades. The earliest sub-ps pulses were generated with dye-lasers and the shortest pulses so far were achieved with Ti:sapphire lasers, with ultrashort pulse durations of less than 10 fs [3]. Semiconductor mode-locked lasers (MLLs) have advantages of compact size, high efficiency, and easy operation. Mode-locked semiconductor lasers have been investigated for over 20 years based on bulk and quantum well (QW) heterostructures. By restricting the carrier movement along one dimension, mode-locking was improved with modified density of states (DOS) in the QWs. Further improvements can be obtained in the structures of quantum dash (QDash) and quantum dot (QD), where electrons are confined in two dimensions and three dimensions, respectively.

The DOS is defined as the number of available electronic states per unit volume per unit energy around some energy E in a three-dimensional system. The DOS is a function of energy and reflects the energy distribution of allowed states. Fermi-Dirac distribution gives the electron occupation probability at a certain energy E. Thus the carrier

distribution in energy is given by the product of the DOS and the Fermi-Dirac distribution. The DOS is an important parameter as it determines many physical properties of materials. Electron confinement in dimensions can change the energy spectrum, resulting in the change of DOS.

The comparison of DOS in the four structures is shown in Fig. 1.1 [4]. In the bulk system, the DOS is proportional to $E^{1/2}$, where it is small at the bottom of the energy band. It is a step-like function in QW, and proportional to $E^{-1/2}$ in QDash (wire). With the three dimensional confinement, QDs have sizes of only a few nanometers and are usually referred to as artificial atoms. Carriers in QDs occupy only a set of discrete energy levels, where the DOS shows delta-function-like peaks. The shape of the DOS becomes more favorable for laser applications with the increase of confined dimensions due to accumulated carrier states at transition energy. The special DOS leads to unique characteristics of QD gain material compared to bulk and QW counterparts. For example, the gain spectrum becomes sharper with increasing confined dimensions due to the DOS as shown in Fig. 1.2. In QDs, the DOS is a delta function so the gain bandwidth is only determined by the relaxation broadening of QD, while for the other structures the shape of the DOS and thermal effect also have effect on carriers. Further calculations found that the gain of QD could reach 10 to 15 times of the bulk structure depending on the material [5]. In addition, significant advantages include low threshold current densities [6], low confinement factor, small linewidth enhancement factor (LEF or α), high temperature insensitivity [7], fast carrier dynamics and inhomogeneous broadband gain have also been explored in QD based optical devices. The first three properties are helpful in the

reduction of noise. And the last two properties are desirable for generating high repetition and short duration pulses.

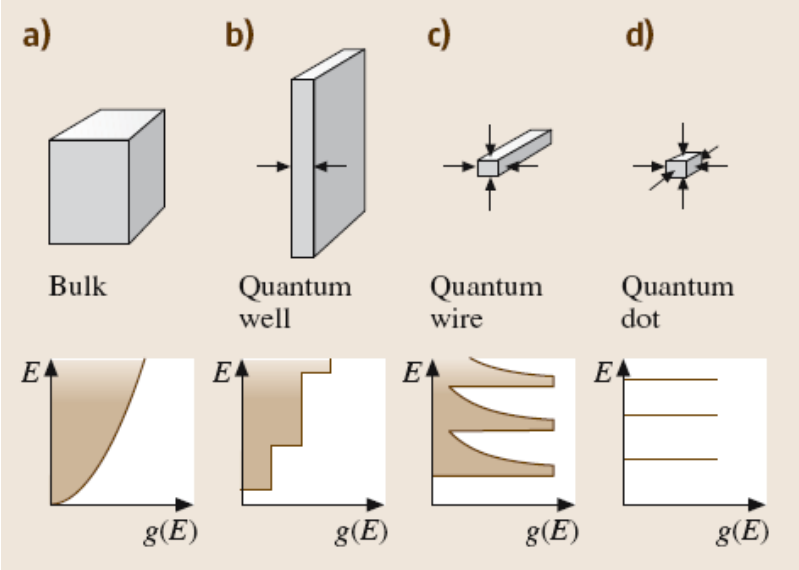

Fig. 1.1 DOS of bulk, QW, QDash and QD semiconductor structures with different confined dimensions [4].

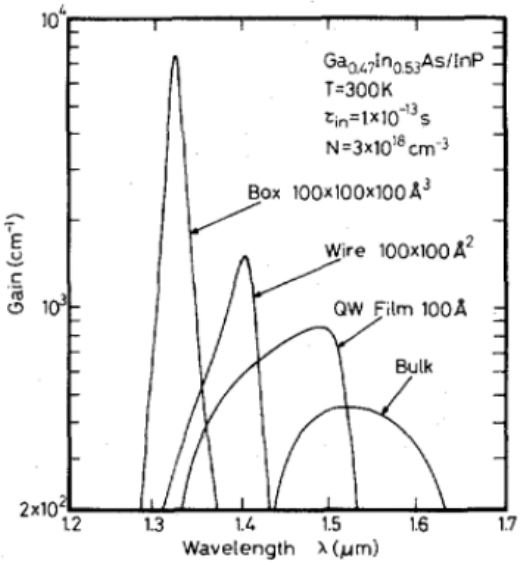

Fig. 1.2. Comparison of calculated gain spectra for four semiconductor structures: QD (box), QDash (wire), QW and bulk. The semiconductor material and sizes of the four structures are indicated in the figure. The intraband relaxation time τ_{in} is assumed to be the same of 1×10^{-13} s as the bulk value and N is the carrier density [5].

QDs can be formed and self-assembled during the 2D to 3D transition in the epitaxial growth. Defect-free self-organized QD islands have been obtained with III-V materials deposited on semiconductor substrates. For example, InGaAs/InAs QDs can be grown on a GaAs substrate with the emission wavelengths of 1.0-1.3 μm or an InP substrate with the emission wavelengths of 1.4-1.9 μm, where the latter one covers the important optical telecommunication band. The size, shape, density and composition of the QDs can be well controlled at growth, promising in making QD lasers, amplifiers, saturable absorbers (SAs), detectors and other optoelectronic devices. Another type is nitride-based, II-VI self-assembled QDs [8], such as CdSe, CdS, etc, which is not discussed in this thesis.

1.1.2 Development of QD lasers and QD MLLs

The idea of QD laser was proposed by Dingle *et al.* in 1976 [9]. The first QD lasers were demonstrated in the early 1990s [7, 10]. The first QD laser near 1.3 μm on the substrate of GaAs was obtained in 1998 [11]. With the modified DOS, the threshold current density J_{th} and the temperature sensitivity should be reduced [12]. A QD laser with single QD layer in the active region by the atomic-layer epitaxy was reported with the J_{th} of 25 A/cm^2 in the pulsed mode and 45 A/cm^2 in the continuous mode, for the first time breaking the record held a long time by the QW laser with the J_{th} between 40-50 A/cm^2 [13]. Later, the J_{th} of as low as 11.7 A/cm^2 and 10.4 A/cm^2 were achieved at the wavelength of 1.22 μm in the continuous mode at room temperature in 2008 [14] and in 2009 [15], respectively, which were also the lowest values among all types of semiconductor lasers. Fig. 1.3 shows J_{th} as a function of year in bulk, QW and QD lasers at room temperature.

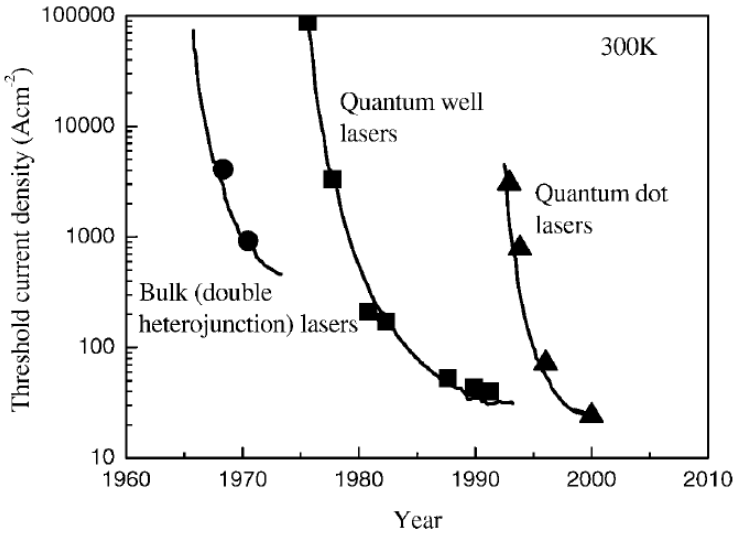

Fig. 1.3. The threshold current density at room temperature versus calendar year for bulk, QW and QD lasers with different confined dimensions in the active layer [16].

Besides the low threshold current density, QD based lasers also exhibit high temperature stability. The characteristic temperature of semiconductor lasers was firstly observed to enhance with carriers confined in two or three dimensions by Arakawa et al. in 1982 [17]. The temperature stability was improved from 45 to 84 K by increasing the number of QD layers from one to three [18]. With 10 layers of QDs, high characteristic temperature of 150 K was achieved in 2002 for the first time [19]. Further, significant improvement of the characteristic temperature was obtained through p-type doping of QD lasers where the characteristic temperature reached 161 K in the temperature range of 0 to 80^{o} C [12]. Extremely high operation temperature of up to 200^{o} C was reported in QD lasers with emission wavelength of around 1300 nm [20]. The threshold current increased from 5 to 75 mA with the temperature increased from 30 to 200ºC and the characteristic temperature was 170 K. The good performance is mainly due to the high saturation gain and large energy separation between ground state (GS) and excited state (ES).

Besides threshold current density and high characteristic temperature, large modulation bandwidth, low chirp and small LEF are also desirable for semiconductor lasers. In conventional In(Ga)As QD lasers at 1.0-1.3 μm, the modulation bandwidth is only 6-8 GHz, limited by the hot-carrier effects [21]. But using the tunnel injection and p-doping, the modulation bandwidth was increased to ~25 GHz [22]. The other parameters of QD lasers could be also improved with the new structure, such as differential gain, characteristic temperature, LEF and chirp, etc. The LEF is a key parameter of semiconductor lasers, where the laser linewidth is $1+\alpha^2$ times larger than the Schawlow-Townes linewidth limit, and the chirp is proportional to α. The LEF in QW lasers is typically larger than 2, which is expected to be reduced in QD lasers with their large differential gains. Nearly zero LEF is obtained in p-doped 1.1 μm tunnel injection QD lasers. The zero LEF was also obtained in 1.3 μm QD lasers around the lasing peak [22].

Due to the delta-like DOS and reduced active volume [23], QDs have attracted lots of attention in making MLLs. The first QD MLL laser was demonstrated by Huang *et al.* in 2001 with a repetition rate of 7.4 GHz at the wavelength of 1.3 μm [24]. The QD laser material was InAs/GaAs and the pulse duration was 17 ps under appropriate bias conditions. Since then, there have been many reports in QD based MLLs. In 2004, Fourier-transform-limited pulses from a passive QD MLL with repetition rate of 18 GHz was emitted at 1.3 μm [25]. At the same year, the first sub-ps pulses at the repetition rate of 21 GHz were demonstrated [26]. By optimizing the current/voltage parameters, the pulse width was decreased from 2 ps to as short as 390 fs. It is the shortest pulse generated directly from a monolithic laser source at that time. In 2005, stable mode-locking at 21 GHz was observed for a temperature range from 20ºC to 80ºC,

demonstrating good temperature stability for ultrafast optical communications [27]. The first colliding pulse mode-locking in QD lasers was demonstrated at 20 GHz with close to transform limited pulse of 7 ps, highlighting the potential for high repetition rate pulse generation using QD lasers [28]. The first single-section QD MLL was reported in 2005 by Renaudier et al. The laser was grown on an InP substrate, and the repetition rate was 45 GHz [29]. The first QD mode-locking from both GS and ES was obtained at 21 GHz and 20.5 GHz, where the switching between the two states was controlled by the biased current/voltage [30]. The first external cavity two-section QD MLL was reported with a low repetition rate of 5 GHz at 1.3 μm [31].

In 2006, harmonic mode-locking from QD lasers was realized from 39 to 238 GHz implementing a multi-contact configuration [32]. The lowest timing jitter of 7.5 fs was reported from active QD MLLs based on an external cavity structure, showing that QD MLLs are promising low noise pulse sources [33]. An external cavity QD MLL using a QD semiconductor saturable absorber mirror (SESAM) was first time demonstrated with high average power of up to 27 mW over a repetition frequency range of 350 MHz to 1.5 GHz [34]. A 53-GHz two-section QD MLL with pulse duration as short as 500 fs at 1.56 μm was demonstrated in 2006 [35]. Repetition rate of 134 GHz and near transform limited pulses were generated from a single-section QDash MLL emitting in the 1.5 μm range [36].

In the following years, many research groups were involved in the development of QD MLLs and have improved their performance on the aspects of output power [37-41], pulse duration [42-46], phase noise [47-50], repetition rate [51-55], dual-wavelength emission [56-59] and theoretical analysis [60-64], etc.

There are three main mode-locking techniques: active, passive and hybrid. In the active mode-locking, the gain section is modulated by an external electrical signal. In the passive mode-locking, a SA is usually used together with the gain in the cavity. And the hybrid mode-locking is the combination of the two techniques above. Passive mode-locking does not need any external sources and has been widely used to generate short pulses. Two sections are normally required in this type of mode-locking, which are gain and SA sections. The gain section is forward biased and the SA section is reversely biased. The saturable absorption in the absorber section has the effect of shortening the pulse while pulse broadening is mainly caused by the gain saturation in the gain section. The dynamics of the two sections is very crucial in pulse shaping. Stable mode-locking is achieved through balancing between pulse broadening and shortening in the two sections. The two-section structure is very typical, not only in QD but also in QW and bulk based passive mode-locked lasers. The locking mechanism of such structure has been extensively studied, and the SA plays an important role in the mode-locking. However, mode-locking in single-section QD lasers where the SA does not exist have also been realized using QDs. There is no interaction between the gain and the SA sections and the physical mechanism leading to locking in this structure is not clear yet.

1.1.3 Applications of QD MLLs

The MLLs can be used for local wireless sub-Terahertz (THz) communication systems as the local oscillators and carriers, Orthogonal Frequency Division Multiplexing systems as the multi-optical-carriers, or optical clock in the photonic assisted analog-digital-converters. The three applications are explained as follows.

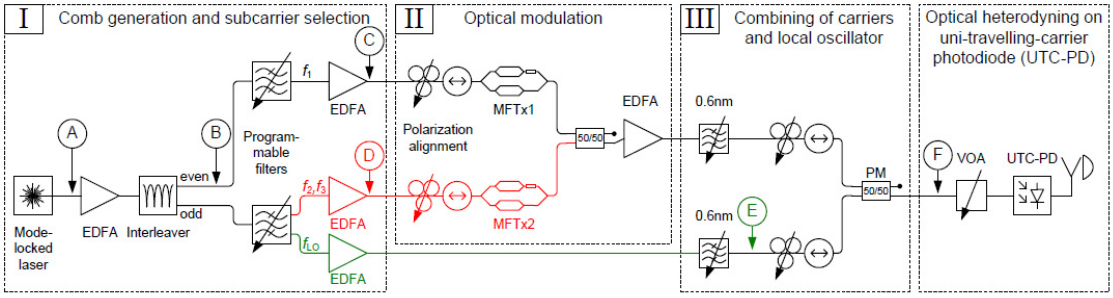

Fig. 1.4. Experimental setup for the generation of sub-THz beating signal at the transmitter side [65].

The data rates in wireless and fiber-optic communications have been increasing over the past decades. But the spectral sources are limited in the conventional frequency range of up to 60 GHz even with the quadrature amplitude modulation and multiple-input and multiple-output technology. Larger bandwidth is required for multi-gigabit or even terabit wireless transmission capacity. The frequency range of 100 GHz to 30 THz is an unexplored region, where the transmission window between 200 and 300 GHz has low atmospheric losses. A wireless communication system with single-input and single-output at 237.5 GHz with data rate of 100 Gb/s has been demonstrated for transmission over 20 m recently. An unmodulated comb line from a MLL acts as a local oscillator and two other selected carrier lines are modulated with data. By photomixing the local oscillator and the modulated carriers through a uni-travelling-carrier photodiode and radiated over an antenna, radio frequency (RF) signals are generated. The repetition rate of the MLL is 12.5 GHz. The carrier as the local oscillator is at 193.138 THz and the two optical carriers are at 193.3755±12.5 THz. The frequency spacing between the local oscillator and the optical carrier is 237.5 GHz [65]. The detailed experimental setup of the transmitter is shown in Fig. 1.4.

Multi-carriers are used to reduce symbol modulation rate for a given data rate in orthogonal frequency division multiplexing, coherent Wavelength Division Multiplexing and optical arbitrary waveform generation [66]. In the orthogonal frequency division multiplexing, the frequency spacing between the carriers is exactly $1/T_s$, where T_s is the symbol duration. The MLLs can be used as the multi-carriers with frequency spacing $1/T_s$ between longitudinal modes (carriers). The longitudinal modes in the MLLs are correlated, which makes it easier for filtering the noise and detecting the signal in the demodulation at the receiver side.

Optical pulses from MLLs can also be used as a clock to make optoelectronic switches in electronic sampling as shown in Fig. 1.5, which has the advantages of fast rise times and low timing jitter. But it has the difficulty of integrating a MLL into an analog to digital converter circuit [67].

In all, MLLs including QD MLLs have wide applications in high speed transmissions for optics, wireless communications as well as microwave photonics.

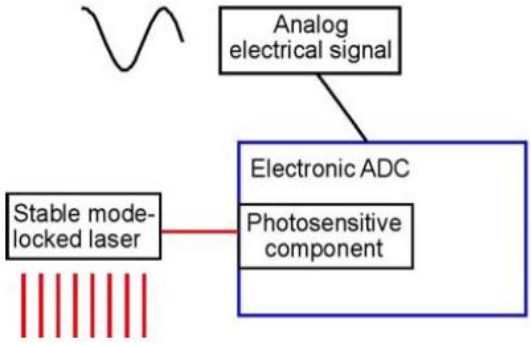

Fig. 1.5. An example of a photonics assisted analog to digital converter where a stable mode-locked laser is used as clock [67].

1.2 Motivations and contributions

High repetition rate and short duration pulses have been successfully generated from single-section QD MLLs. For example, the pulse width of a 92-GHz QD MLL at C band was as short as 312 fs [68]; the pulse width of a L-band 46-GHz QD MLL was 445 fs [69]. Pulse duration of ~590 fs with a repetition rate of 245 GHz was demonstrated in a single-section QDash MLLs [52]. A high repetition rate of 346 GHz with pulse width of ~560 fs was also reported from a single-section QDash MLLs at 1.55 μm [70]. The repetition rate is inversely proportional to the cavity length, which is shorter with only one section in the cavity. Because of no SA section, the pulse width is not affected by the group velocity dispersion (GVD) and the self-phase-modulation (SPM) in the absorber section. Considering both repetition rates and pulse widths, single-section MLLs are attractive in ultrafast and short pulse generation. In addition, they are easier to fabricate due to only one section in the cavity.

Most reported passive QD MLLs consist of two sections. The working mechanism and performance have been well investigated. The passive mode-locking with a SA is an established technique as it has been realized in dye, solid state and semiconductor lasers. The mode-locking properties have been improved by optimizing two-section driving conditions, i.e. drive current of the gain section and reverse-biased voltage of the SA section, modifying the ratio of the two-section lengths, and using external cavity methods, etc. However, researches on single-section QD MLLs are limited. There have been only a few demonstrations of this type of QD MLLs based on InAs QDashes on the substrate of InP [71], InAs QDs on the substrate of InP [72] and InAs QDs on the substrate of GaAs [43]. There have been also a few experimental reports on pulse width shortening by GVD

compensation [73-75], low timing jitter [76] and phase noise reduction [47]. Besides, the locking phenomenon has been attributed to high nonlinearity of the QD gain medium [68] or random population of carriers in QDs [77]. But there is still no theoretical study or explanation on the locking mechanism for this type of mode-locked lasers.

In this thesis, the research focuses on investigating and optimizing the mode-locking performance of single-section InAs/InP QD lasers. The main contributions include:

1) Measurement the LEF of our QD lasers, which is one of the key parameters of semiconductor lasers.
2) Simulation of single-section QD MLLs using time-domain travelling wave (TDTW) models. An equivalent SA is proposed to model the mode-locking in single-section QD MLLs.
3) Investigation of the GVD and SPM effects on the pulse evolution in single-section QD MLLs.
4) Demonstration of ultra-high repetition rate pulse generation of up to 1.01 THz using single-section QD lasers combined with external fiber-Bragg-grating (FBG) cavities.
5) Generation of tunable THz beating signal from 1 to 2.1 THz using single-section QD lasers combined with external cavities composed of two FBGs.

1.3 Organization of the thesis

In this chapter, the basic concept of mode-locking is introduced. The DOS in QDs is compared to bulk, QW and QDash structures, which leads to unique characteristics of QD based lasers and MLLs. The applications of QD MLLs are also briefly introduced. Then, the motivations and contributions of the research work are presented.

In chapter 2, the key properties of QD based amplifiers and lasers will be discussed. Then theoretical models used in simulating QD MLLs will be given, including the TDTW model and the delayed differential model. The TDTW model will be described in detail. Electric field and carrier dynamics are described by the TDTW equations and rate equations in this model, respectively. The inhomogeneous gain, homogeneous gain, and grouping of QDs are included too. Moreover, the experimental and theoretical work on QD MLLs will be reviewed.

In chapter 3, the LEF of our QD lasers will be measured using two methods, i.e. Hakki-Pauli and injection locking. The LEF is a fundamental parameter in all semiconductor lasers. The obtained small LEF indicates that our QD gain material is ideal for making QD lasers and amplifiers.

In chapter 4, the TDTW model is applied for single-section QD MLLs, and an equivalent SA will be proposed to deal with the mode-locking. With shorter and shorter pulses generated in QD MLLs, it is necessary to take GVD effect into consideration in modeling the pulse evolution in the cavity. And SPM may also be important due to the relative high power density in the laser cavity. Therefore, the TDTW model is improved by including both of the effects. To solve the improved model, numerical methods such as Taylor expansion and central difference approximation are adopted. The simulation results are compared with ours experimental results, and the effects of GVD and SPM on the pulse evolution are also discussed. Finally the nonlinear effect in the cavity is analyzed.

In chapter 5, ultrahigh-repetition-rate pulses generated from QD lasers combined with external cavities are demonstrated. Using the external cavity structure, the repetition rate

can be greatly increased and the limit of inadequate gain caused by short cavity is overcome. The external cavities consist of FBGs and the repetition rate can be varied by using FBGs with different frequency spacings. Repetition rates of 394 GHz, 403 GHz, 437 GHz and 1.01 THz have been realized using this structure. The FBG selected longitudinal modes are phase correlated and the FWM effect is observed on the spectra.

In chapter 6, QD laser with the external cavity structure is then used to generate tunable THz beating waves. THz beating from 1 to 2.1 THz is observed. Pulse trains are also observed using the autocorrelator, indicating phase correlation between selected modes. This method can be used to generate microwave signals for microwave photonic applications.

In chapter 7, a summary of the accomplished results are given. The potential applications are also concluded at last. Future research on single-section QD MLLs is suggested.

Chapter 2 Fundamental Properties and Theoretical Models

2.1 Introduction

Due to the delta-function-like DOS, QDs have shown some special properties, making them very attractive in the fabrication of amplifiers, lasers and MLLs. In this chapter, fundamental theory and experimental results obtained in QDs are given. Firstly in section 2.2, the growth of QDs is simply introduced. Then the fundamental properties of QD based optoelectronic devices are presented in section 2.3. After that, three types of passive QD MLLs are explained in section 2.4 and two numerical models are given in section 2.5, which are delayed differential model and TDTW model. The TDTW model is described in detail, where the QD homogeneous gain, inhomogeneous gain, optical susceptibility, spontaneous emission are fully included in the model. The electric field and carrier dynamics are obtained by solving the TDTW equations and rate equations together. Then, techniques for improving mode-locking performance in QDs, including pulse duration, repetition rate, phase noise, etc., are reviewed in section 2.6. A conclusion for this chapter is drawn in section 2.7 at last.

2.2 Growth of QDs

QDs can be fabricated by epitaxial techniques such as Chemical Beam Epitaxy (CBE), Molecular Beam Epitaxy (MBE) and Metal Organic Chemical Vapor Deposition (MOCVD). In the MBE, the thermally evaporated molecular beams are deposited onto the substrate to form thin epitaxial layers. It has high degree of control in the growth of semiconductor layers and is a good technology in developing sophisticated optoelectronic devices. In contrast to MBE, a series of chemical reactions but not physical deposition

occur in the process of MOCVD. And in the epitaxial growth, there are three modes of growth: Frank-van der Merwe, Volmer-Weber, and Stranski-Krastanow (SK). The growth mode is determined by the interface energies and lattice mismatch. By epitaxial growth of a semiconductor material on another material with a smaller lattice constant (such as In(Ga)As on GaAs), layer-by-layer occurs at first. Then when the planar layer gets thick enough, atoms tend to form clusters to release strain and self-assembled islands are formed. The self-assembled islands are QDs and the thin (a few monolayers) 2D layer formed before the islands is called the wetting layer (WL). This mode of growth is called SK. Using the SK method, the growth of InGaAs QDs on InGaAsP, InGa on GaAs, InGaAs on GaAs, InAs on InP, InP on GaInP etc. have all been realized. Using the same substrate, the size and shape of the QDs varies with the deposited dot material in a certain range. The energy states of QDs also change with different dot sizes and shapes due to the strain in the dots.

Besides, QDs have also been produced by etching QWs. However, surface states are created, leading to high threshold current density. The self-assembled QDs are defect-free and have shown excellent characteristics compared with the etched ones. The SK growth method makes QDs promising for laser applications. An atomic force microscopy of InAs QDs grown on InP (113)B by MBE is shown in Fig. 2.1 [73]. Multiple QD layers can be stacked to increase the QD area density, lower the threshold current and increase the modal gain in lasers. Electroluminescence and photocurrent spectroscopy are the techniques often used to determine the physical structure and transition energies of dots. Typical electroluminescence spectrum for two injection currents and photocurrent spectrum are shown in Fig. 2.2 [78]. Up to four QD transitions (E_0 to E_3) are observed on

the photocurrent spectrum, which corresponds to four interband transitions: GS, ES, and higher levels. The GS is the lowest energy state of QDs and ES is the higher QD state. More than one ES could be observed.

For the electroluminescence, only one emission peak at energy E_0 is observed at low current corresponding to GS, and when GS is fully occupied another peak at E_1 appears at higher current corresponding to ES. The transition states indicated by the above two methods are in coincidence with each other.

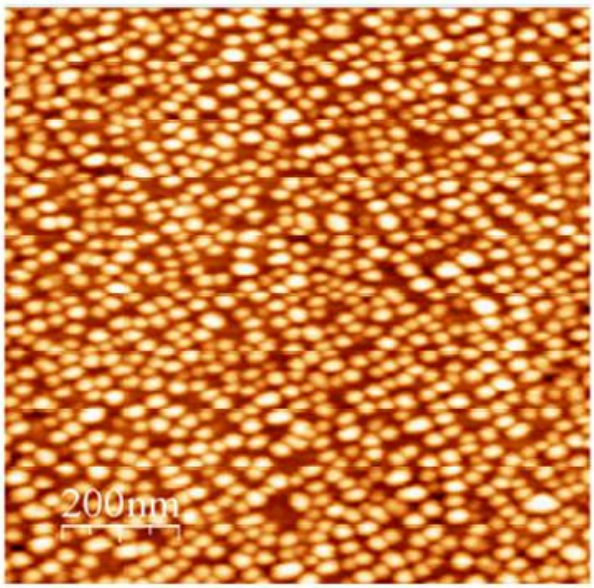

Fig. 2.1. Illustration of self-assembled InAs QDs grown on InP by MBE. The dot diameter is ~30 nm and dot density is 10^{11} cm^{-2} [73].

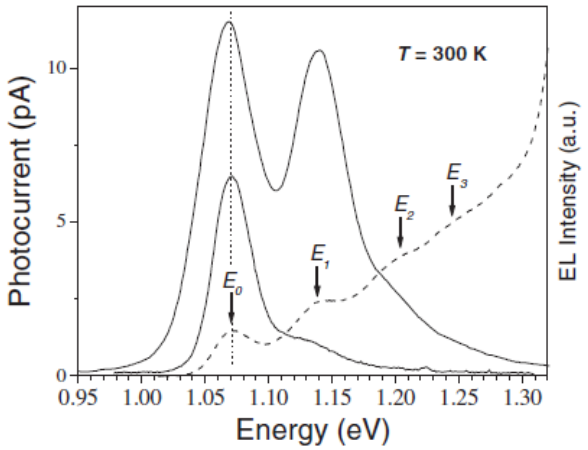

Fig. 2.2. Photoluminescence (dash line) and electroluminescence (solid line) spectra at room temperature for self-assembled QDs [78].

A schematic band structure of a typical QD laser is shown in Fig. 2.3. In the figure, the active layer consists of three QD layers surrounded by higher bandgap material (InGaAsP barrier) and the WL is formed between QDs and the barrier. Three layers of QDs are vertically aligned to increase the dot density and the modal gain. The emission wavelengths vary with different substrates and dot materials. Due to the dispersion of the dot sizes and shapes, the energy states of QDs are different, resulting in inhomogeneous gain broadening.

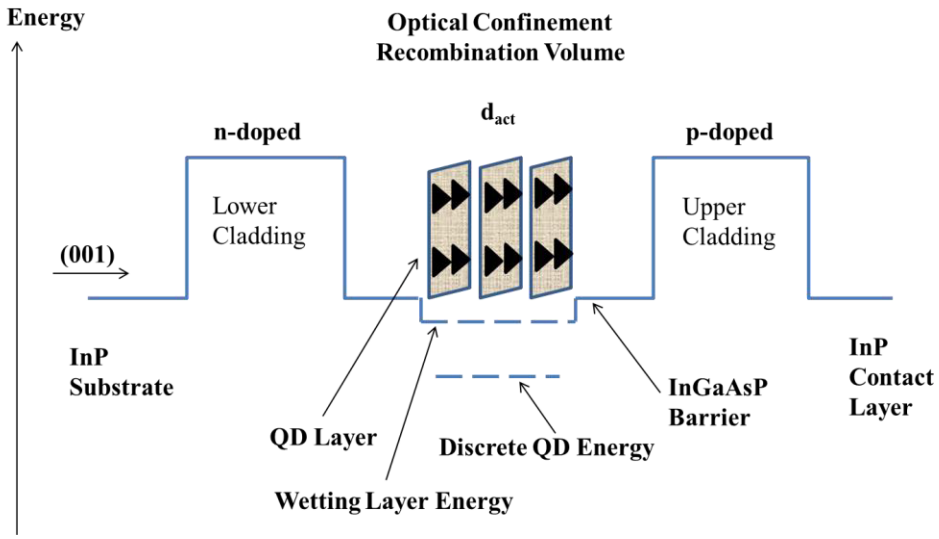

Fig. 2.3. Band structure of a typical QD laser. Three layers of self-assembled QDs with equal size and shape are illustrated in the figure.

2.3 Key properties

2.3.1 Small LEF

The LEF is one of the most important parameters in semiconductor lasers including QD lasers. It determines many fundamental properties of QD lasers, such as linewidth, feedback sensitivity, frequency chirp and timing jitter of MLLs.

The LEF is defined as [79]

$$\alpha = \frac{-4\pi}{\lambda}\frac{dn/dN}{dg/dN} = \frac{-4\pi n}{\lambda^2}\frac{d\lambda/dN}{dg/dN} \tag{2.1}$$

where n is the refractive index, g is the net modal gain, and N is the carrier density. It measures the coupling between the refractive index and the gain with the variation of carrier densities in the active region. It can be calculated directly from the gain spectrum below threshold using the equation above.

Ideally, the delta-function DOS in QDs results in a symmetrical gain spectrum where only one energy level exist in the gain spectrum and the differential refractive index

change is exactly zero at the lasing peak. Thus zero LEF value is expected at the gain peak [23]. However, due to the inhomogeneous broadening and the existence of ES, the LEF in QDs could not reach zero. But it is still smaller than in QWs [80]. Typical LEF values in bulk and QWs are about 3 and 2, respectively, whereas in QDs it is usually less than 1 [81]. The LEF value of as low as 0.1 has been reported in an InAs/GaAs QD laser emitting at 1.22 μm [82]. In p-doped tunnel injection QD lasers, almost zero LEF was found, and no wavelength shift with biased current was observed in the sub-threshold spectrum [22]. The chirp is the change of the carrier frequency with time in a signal, which is originated from and proportional to the LEF. The carrier induced refractive index change is reduced in QDs, leading to small frequency chirp in high bit rate data transmissions [80].

2.3.2 Inhomogeneous broadening gain

Due to the unique DOS of QDs, the original purpose was to design single wavelength lasers using QDs as the gain material. But real QD lasers show very broad spectral bandwidth compared with conventional QW lasers. Ideally, QDs have the same shape and size, corresponding to a single line in the emission spectrum representing either GS or ES (Fig. 2.4 (a)). However, it is impossible for QDs to be self-assembled at the same size and shape. Actually, the sizes of QDs follow the Gaussian distribution roughly (Fig. 2.4 (b)), leading to a broadband Gaussian shape gain spectrum, which is referred to as inhomogeneous gain broadening. This is a unique property of self-assembled QDs, which makes QDs very attractive for the generation of ultrashort ML pulses because the pulse width is inversely proportional to the gain bandwidth. Hence, shorter pulses are expected in QD MLLs compared to bulk and QW counterparts.

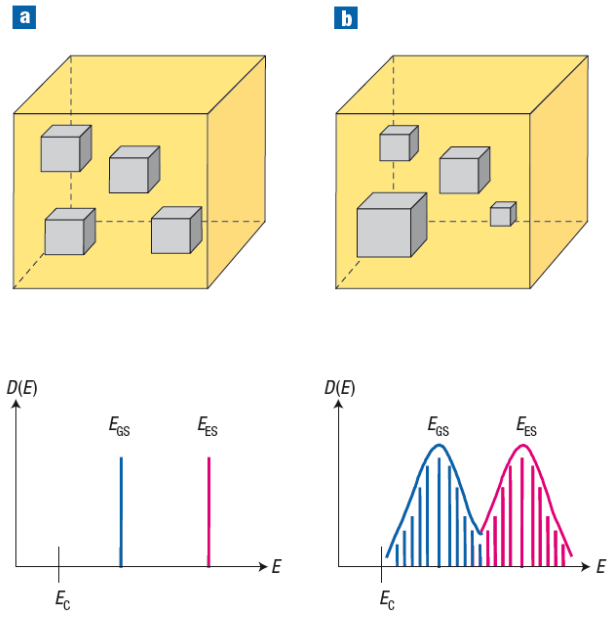

Fig. 2.4. Illustration of QDs growth and the corresponding DOS (D(E)) in (a) an ideal QD system and (b) a real QD system [83].

Due to the inhomogeneous gain broadening, the 3-dB and 10-dB bandwidth of a QD semiconductor optical amplifier (SOA) could reach 150 and 300 nm respectively [84]. In Fig. 2.5, the optical spectrum of the QD SOA is compared with QW SOAs and EDFAs. Obviously, the spectrum of the QD SOA is much broader than other broadband amplifiers. The centre wavelength and gain bandwidth can even be shifted/controlled at growth.

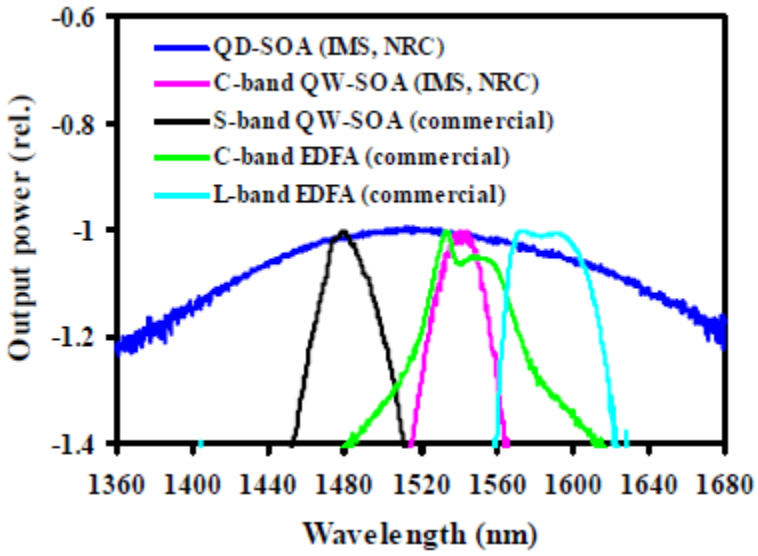

Fig. 2.5. Comparison of emission spectra of QD SOA, QW SOAs and EDFAs [84].

2.3.3 Fast carrier dynamics and gain /absorption recovery time

In zero-dimensional QDs, the electron-phonon scattering rate is reduced due to the delta-function-like DOS, which is known as phonon bottleneck effect [85]. Then it is predicted that the low scattering rate will lead to longer relaxation time (ps order) between QD states than in QW and bulk materials. The long relaxation time will strongly limit the application of QDs in lasers and amplifiers. But contrary to the predictions, fast carrier dynamics have been demonstrated by pump-probe experiments. In QDs, two distinct recovery times of the absorption exist. A fast recovery (1 ps) was found to be followed by a slow decay (100 ps) as shown in Fig. 2.6 [86]. An ultrafast recovery time of ~100 fs is also measured, attributed to Auger scattering, which provides a channel for carriers relaxing from ES into GS [87].

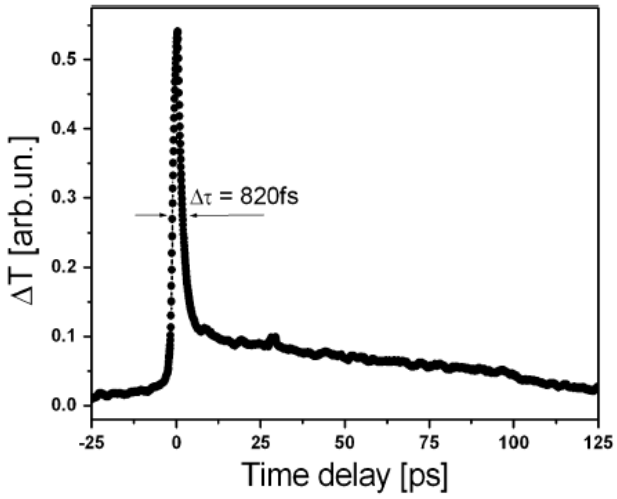

Fig. 2.6 Illustration of two recovery times of a QD-based device by pump-probe measurements [86]. ΔT is the change in the transmission of the probe due to absorption saturation of the pump.

In an experiment directly measuring the absorption recovery, the recovery time is decreased from 62 ps to 700 fs with the reversed bias changed from 0 to -10 V [88]. The fast recovery at higher applied bias is attributed to tunneling effect. The absorption recovery time is found to be an important parameter for pulse shaping. By increasing the reversed bias, the recovery is more efficient, which has the effect of further shortening the pulses. Ultrafast gain compression recovery of only ~100 fs was also measured in a QD SOA [89]. With fast carrier dynamics and gain/absorption recovery time, the QD based optoelectronic devices are promising for high speed applications and high repetition rate pulse generation.

2.4 Passive QD MLLs

2.4.1 Two-section QD MLLs

Two-section passive mode-locked semiconductor lasers usually have two sections: gain and SA as illustrated in Fig. 2.7. The gain section with length L_g is forward biased while

the SA section with length L_a is reversely biased. This is also the typical structure of two-section QD passive MLLs.

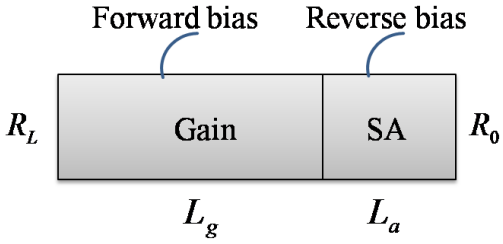

Fig. 2.7. A typical structure of two-section passive semiconductor MLLs. R_L and R_0 are the reflectivity at the two facets.

The working principle in the two-section structure is well-understood that the interaction of the two sections determines pulse formation. Pulse broadening and pulse shortening are governed by the gain and SA sections, respectively, the balancing of which leads to stable mode-locking.

The laser modes start from noisy bursts, the peak of which experience less attenuation and more amplification in the cavity due to the loss saturation. Then the bursts are further shaped by the saturation absorption when travelling back and forth in the cavity until stable mode-locked pulse train is formed at steady state [83]. The dynamics of gain and loss in the pulse shaping is shown in Fig. 2.8. At steady state, when the leading edge of the pulse reaches the cavity, the loss is unsaturated and higher than the gain. But the leading edge of the pulse saturates the absorber faster than the gain, leaving a net gain window around the pulse peak area. The absorber also recovers from saturation to highly loss state more quickly than the gain. Then the trailing edge of the pulse is attenuated by the absorber. A net gain window is formed around the peak area as shown in Fig. 2.8. The saturation power and recovery time of the absorber are two important parameters in

the pulse formation and shaping. With the reversely biased voltage, generated carriers can be swept out of the SA section quickly and thus the absorber recovery time is decreased. By increasing the reverse bias on the SA, pulse widths can also be shortened due to the reduction of the gain window.

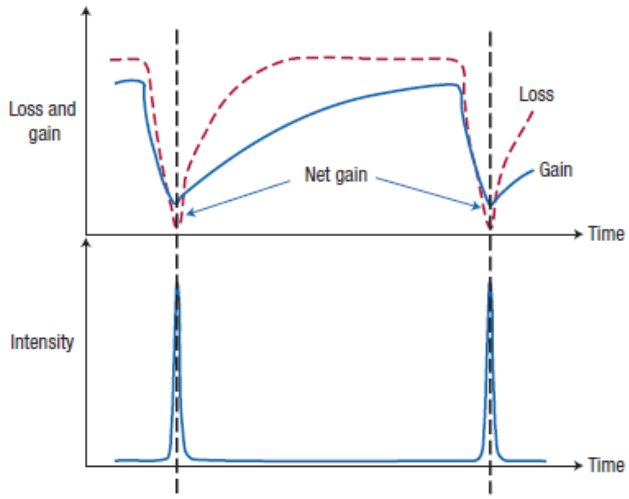

Fig. 2.8. Interaction of gain and saturable absorption for pulse generation in a two-section passive MLL [83].

2.4.2 Single-section passive QD MLLs

Without the SA section, mode-locking has also been realized in QDs. There is only a forward biased gain section. It is believed that the mode-locking principle is different from the two-section QD MLLs. No detailed theoretical analysis has been given based on this structure but four-wave mixing (FWM), Kerr-lens effect and random population model have been reported to be the possible mechanisms leading to the locking.

The FWM effect originates from the nonlinear response of the medium to the optical field where the medium plays a passive role. A wave at a new frequency ω_4 is generated by three optical fields at frequencies ω_1, ω_2 and ω_3. And the four frequencies have the relationship of $\omega_4 = \omega_1 \pm \omega_2 \pm \omega_3$. The momentum conservation should be satisfied for

this process to occur, which is referred as phase-matching condition. The relationship $\omega_4 + \omega_3 = \omega_1 + \omega_2$ corresponds to the case where two photons at frequencies ω_1 and ω_2 generate two new photons at frequencies ω_3 and ω_4. The phase-matching condition for this process to occur is $\Delta k = \left(n_4\omega_4 + n_3\omega_3 - n_1\omega_1 - n_2\omega_2\right)/c = 0$. For the specific case $\omega_1 = \omega_2$, $\omega_3 = \omega_1 + \Omega$, and $\omega_4 = \omega_1 - \Omega$, where Ω is the frequency difference, the phase-matching condition is relatively easy to be satisfied and the FWM is referred as degenerate FWM otherwise it is non-degenerate.

Non-degenerate FWM in semiconductor lasers and amplifiers is very promising for wavelength conversion in high-bit-rate optical transmission systems with a bit rate of 160 Gb/s to 1 Tb/s due to its fast speed and free modulation format [90]. But the conversion is usually asymmetry, and the efficiency is low at the long wavelength side in conventional bulk and QW based SOAs [91]. Due to the 3-D confinement and small active volume, high nonlinearity is expected in QDs. And QD based SOAs are very promising in symmetric and direction-independent conversion with smaller LEF value. The efficiency of non-degenerate FWM is often obtained by pump-probe experiment. In the experiment, a pump and a probe signal are injected into a laser to amplify the probe signal and generate FWM sidebands. The efficiency is defined as the FWM sideband power on the pump side (conjugate signal power) over the probe input power for a constant pump power. As an example in Fig. 2.9 [92], the negative detuning (longer wavelength side) is greatly improved in a QD SOA (Fig. 2.9 (a)) compared to a bulk SOA (Fig. 2.9 (b)). The positive detuning efficiency is also improved. The conversion slopes are almost identical for positive and negative detunings in the QD SOA. The symmetric conversion efficiency

has also been reported in other QD amplifiers and lasers [91, 93], indicating low LEF value in the QD gain material.

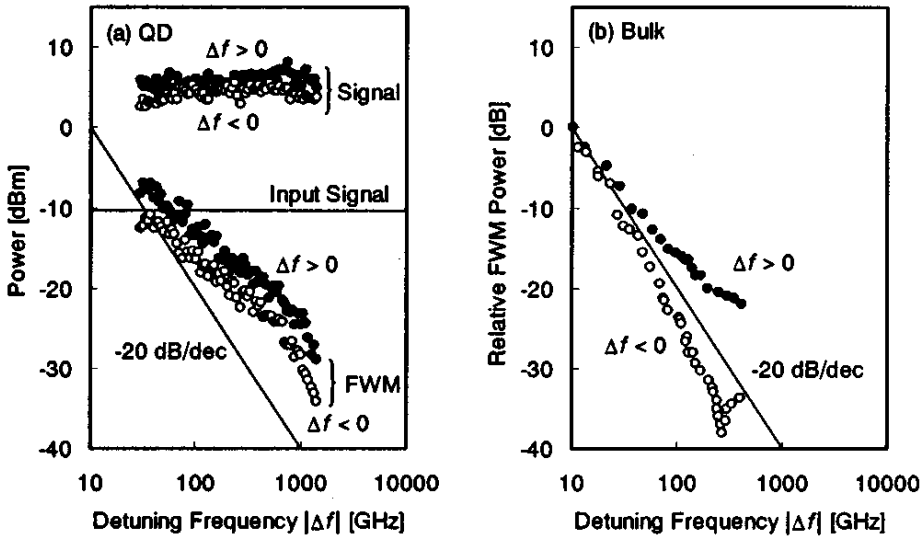

Fig. 2.9. Comparison of conversion efficiency and symmetry in QD and bulk based SOAs. Δf is the frequency detuning between the pump and the probe. Δf>0 when $\lambda_{pump} < \lambda_{probe}$; Δf<0 when $\lambda_{pump} > \lambda_{probe}$ [92].

The phase correlation in a single-section passively QD MLLs is measured through the spectral linewidth at half maximum of the RF spectrum [94]. Three different couples of modes are taken from the emission spectrum of a QD MLL and their mode-beating spectra are compared with RF spectrum of the whole spectrum. The measured spectral linewidth are the same for the four spectra, indicating that the modes have the same phase noise and are partly correlated through FWM in the QD laser. Besides, the mode-beating linewidth is much narrower than the linewidth of each single longitudinal mode, demonstrating the synchronization of the phase fluctuations of these longitudinal modes. Thus the phase correlation might be attributed to the FWM effect in the QD cavity.

The Kerr-lens effect is also a nonlinear effect working as an artificial SA in the Fabry-Perot cavity which imposes a spatial intensity dependent profile on the beam

propagating in the gain cavity. If we consider waveguides as thick hard apertures, random intensity spike will lead to periodic pulse trains by Kerr-lens effect due to self-focusing [58]. The random intensity spike will be focused and get enhanced in the cavity while low intensity light will be filtered out by the waveguide. The refractive index is given by $n = n_0 + n_2 I$, where n_2 is the nonlinear refractive index and *I* is the intensity. Assuming a Gaussian-shape laser beam, the centre is more intensive than the edge due to the nonlinear refractive index and thus experiences more gain by the waveguide as shown in Fig. 2.10 [3]. This way of producing mode-locking pulse trains is called Kerr-lens mode-locking.

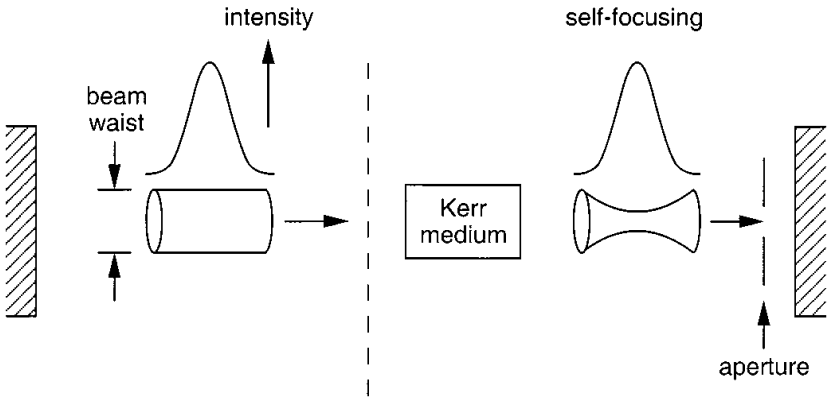

Fig. 2.10. Illustration of Kerr-lens mode-locking by an artificial SA [3].

In the random population model, even above the threshold, some QDs are considered as gain while the others are considered absorptive similar to the SA in two-section QD MLLs. In this model, self-pulsation or pulse trains can be obtained without the nonlinear effects mentioned above [77]. Further study is still required to explain mode-locking in single-section QD MLLs.

2.4.3 QDash MLLs

Besides QD, two-section and single-section MLLs have also been realized in QDash. Carriers in the QDash are two-dimensional confined and QDash is usually considered as elongated dot. They are usually formed by MBE epitaxial grown on InP (100) surface whereas QDs are usually fabricated by Metal-Organic Vapor Phase Epitaxy (MOVPE) or CBE techniques [71]. InAs QDash lasers and amplifiers at 1.4-1.6 μm wavelength range have been realized based on the substrate of InP [94, 95]. The typical thickness, width, and length of the dashes are about 2 nm, between 15 nm to 20 nm and between 40 nm and 300 nm, respectively. InAs/InP QDash MLLs at 1.55 μm have been realized in both single-section and two-section structures. Three types of grown structures have been studied: dots in a barrier, dots-in-a-well and tunnel injection as illustrated in Fig. 2.11 [96]. In the dots-in-a-well structure, QDs are surrounded by QW, which is helpful for capturing carriers into dots and lowering the threshold current [97]. High repetition rate pulses and short pulse widths have also been achieved in single-section QDash MLLs. It is suggested that there is no fundamental difference between QD MLLs and QDash MLLs [83].

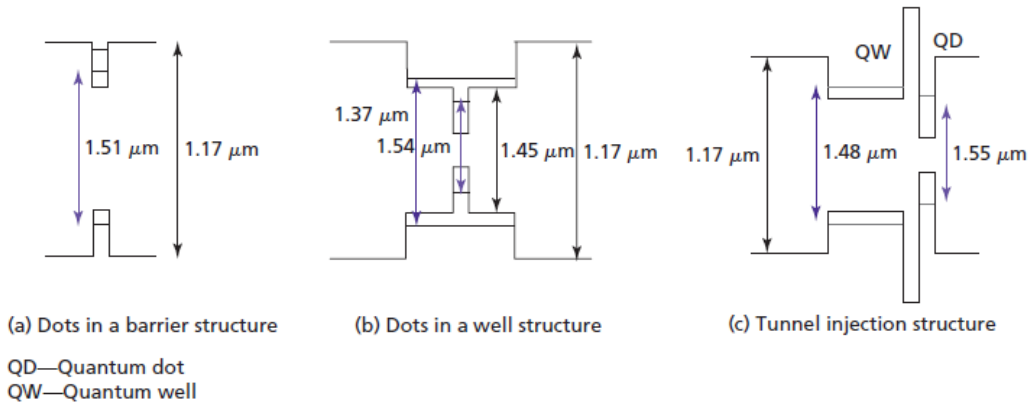

Fig. 2.11. Energy band diagrams of three structures of QDash lasers: (a) dots in a barrier structure, (b) dots in a well structure and (c) tunnel injection structure [96].

2.5 Modeling of QD lasers

For modeling QD lasers, rate equations are generally used to describe carrier dynamics in the laser cavity. To describe the electric field, different methods are used. In the following, two methods will be introduced: TDTW and delay differential. The equations for carrier dynamics and electric filed are combined together to model the performance of QD lasers.

2.5.1 Time-domain travelling wave model

2.5.1.1 TDTW equations

Semiconductor lasers and amplifiers can be described by TDTW equations for electric field and rate equations for carrier densities in the cavity.

The theory of calculating the electromagnetic field starts from the Maxwell equations for the electric field $\vec{E}$ and magnetic field $\vec{H}$ in the frequency domain.

$$\nabla \times \vec{E} = -j\omega\mu_0 \vec{H} \tag{2.2a}$$

$$\nabla \times \vec{H} = j\omega\varepsilon \vec{E} \tag{2.2b}$$

where μ_0 is the vacuum magnetic permeability and ε is the permittivity given by $\varepsilon = \varepsilon_0 \varepsilon_r(\omega, \vec{r})$. ε_0 is the vacuum permittivity and $\varepsilon_r(\omega, \vec{r})$ is the dielectric constant of the background medium, which is spatial ($\vec{r}$) and frequency (ω) dependent. Two additional terms need to be added into Eq. (2.2b) when electromagnetic field in the semiconductor active medium is considered. Then Eq. (2.2b) is changed to

$$\nabla \times \vec{H} = j\omega\varepsilon_0 \varepsilon_r(\omega, \vec{r})\vec{E} + j\omega\vec{P}(\omega, \vec{r}) + \vec{J}(\omega, \vec{r}) \tag{2.3}$$

where $\vec{P}$ is the additional polarization induced by the QD active medium and $\vec{J}$ is the stochastic current density due to the spontaneous emission noise from the QD active medium.

A few approximations and assumptions have to be made for getting the solution. In the equations, the vectors ($\vec{\mathrm{E}}, \vec{\mathrm{H}}, \vec{\mathrm{P}}, \vec{\mathrm{J}}$) can be decomposed into transverse (x-, y-) and propagation (z-) directions. In the transverse plane, x-axis is along the growth direction and y-axis is the lateral ridge direction. In the planar waveguide, two sets of orthogonal modes exist: TE (transverse electric) and TM (transverse magnetic) modes. Whereas in ridge waveguides, TE and TM modes cannot be strictly defined and only quasi-TE and quasi-TM modes with small electric or magnetic components on the z-direction are supported. In addition, as the predominant field in QD edge-emitting devices [98, 99], only quasi-TE field will be considered in the following. And the ridge waveguide is usually designed to support a single fundamental transverse mode transmission at the operating frequency. The propagation constant is given by $\beta(\omega)=\frac{\omega}{c}n$, where c is the speed of light and n is the refractive index.

Then a second-order differential equation can be obtained:

$$\frac{\partial^2 E}{\partial z^2}(z,\omega) = -\frac{\omega^2}{c^2} n^2 E(z,\omega) - \omega^2 \mu_0 \varepsilon_0 \chi(z,\omega) E(z,\omega) + j\omega\mu_0 J(z,\omega) \qquad (2.4)$$

The polarization P is expressed through electronic susceptibility $\chi(z,\omega)$ by

$$P(z,\omega) = \varepsilon_0 \chi(z,\omega) E(z,\omega) \qquad (2.5)$$

To solve Eq. (2.4), the electric field is decomposed into forward and backward propagation directions as

$$E(z,t)=\sqrt{\frac{\omega_0\mu_0}{\beta_0}}\left(E^{+}(z,t)e^{-j\beta_0 z}+E^{-}(z,t)e^{j\beta_0 z}\right)e^{j\omega_0 t} \tag{2.6}$$

where ω_0 is the centre reference frequency and β_0 is the corresponding propagation constant at ω_0 ($\beta_0=\beta(\omega_0)=\frac{\omega_0}{c}n(\omega_0)=\frac{\omega_0}{c}n_0$). The centre frequency ω_0 is usually chosen to be close to the lasing frequency and the slowly varying envelope approximation is applied, where the bandwidth of the electric field is much smaller than ω_0 . If the lasing wavelength is at 1550 nm, then ω_0 equals to 193.55 THz. If the inhomogeneous gain bandwidth is about 40 meV, the maximum frequency detuning from the centre is $|\Delta\omega|_{\max}\approx 9.67\,\text{THz}$, which is small compared with ω_0. The electric field in Eq. (2.6) is normalized so that the power flow in each direction is simply given by either $\left|E^{+}(z,t)\right|^2$ or $\left|E^{-}(z,t)\right|^2$.

Converting Eq. (2.6) into the frequency domain, we get

$$E(z,\omega_0+\Omega)=\sqrt{\frac{\omega_0\mu_0}{\beta_0}}\left(E^{+}(z,\Omega)e^{-j\beta_0 z}+E^{-}(z,\Omega)e^{j\beta_0 z}\right) \tag{2.7}$$

where Ω is the relative frequency to the centre frequency ω_0 ($\Omega=\omega-\omega_0$). Substituting Eq. (2.7) into Eq. (2.4) and assuming $\left|\frac{\partial^2 E}{\partial t^2}\right|\ll\left|\omega_0\frac{\partial E^{\pm}}{\partial t}\right|$ and $\left|\frac{\partial^2 E}{\partial z^2}\right|\ll\left|\beta_0\frac{\partial E^{\pm}}{\partial z}\right|$, we obtain

$$\begin{aligned}\pm\frac{\partial E^{\pm}}{\partial z}(z,\Omega)=&-j\frac{\Omega}{v_{g0}}E^{\pm}(z,\Omega)-j\frac{\omega_0}{2cn_g}\chi(z,\omega_0+\Omega)E^{\pm}(z,\Omega)\\&+\frac{1}{2}\sqrt{\frac{\mu_0\omega_0}{\beta_0}}J(z,\omega_0+\Omega)\end{aligned} \tag{2.8}$$

where v_{g0} is the group velocity and n_g is the group index. By converting Eq. (2.8) into the time-domain, we get

$$\pm\frac{\partial E^{\pm}(z,t)}{\partial z}+\frac{n_g}{c}\frac{\partial E^{\pm}(z,t)}{\partial t}=-\frac{\alpha_i}{2}E^{\pm}(z,t)-jP^{\pm}(z,t)+F^{\pm}(z,t), \qquad (2.9)$$

where the variables z and t represent wave transmission position and time, α_i is the intrinsic waveguide loss, and $P^{\pm}(z,t)$ and $F^{\pm}(z,t)$ are forward (+) / backward (-) modified polarization and spontaneous emission noise, respectively. Note that α_i is additionally introduced into Eq. (2.9) to account for the loss in the waveguide, which is not considered in Eq. (2.8).

The modified polarization $P^{\pm}(z,t)$ is given by

$$P^{\pm}(z,t)=\frac{\omega_0}{2cn_g}\int_{-\infty}^{t}\tilde{\chi}(z,t-\tau)E^{\pm}(z,\tau)d\tau, \qquad (2.10)$$

where $\tilde{\chi}(z,t)=\frac{1}{2\pi}\int_{-\infty}^{+\infty}\chi(z,\omega_0+\Omega)e^{j\Omega t}d\Omega=\chi(z,t)e^{-j\omega_0 t}$ is the modified optical susceptibility.

And the spontaneous emission noise is defined as

$$F^{\pm}(z,t)=\frac{1}{2}\sqrt{\frac{\mu_0\omega_0}{k_0}}\frac{1}{2\pi}\int_{-\infty}^{+\infty}J(z,\omega_0+\Omega)e^{j\Omega t}d\Omega=\frac{1}{2}\sqrt{\frac{\mu_0\omega_0}{k_0}}J(z,t)e^{-j\omega_0 t} \qquad (2.11)$$

Eq. (2.9) is the TDTW equation in forward and backward propagation directions. It is widely applied to model electric field in edge-emitting optical devices. For the Fabry-Perot cavity, two additional boundary conditions are required:

$$\begin{aligned}E^{+}(0,t)&=r_r E^{-}(0,t)\\ E^{-}(L,t)&=r_l E^{+}(L,t)\end{aligned} \qquad (2.12)$$

where L is the cavity length, and r_r and r_l are the amplitude reflectivity at the two facets.

2.5.1.2 Inhomogeneous and homogeneous gain

Due to the size and shape fluctuation of QDs at growth, inhomogeneous line broadening of 30-70 meV has been measured [100]. The inhomogeneous bandwidth is expressed by a Gaussian distribution function as

$$G_i = \frac{1}{A}\exp\left(-4\ln 2 \times \frac{\left(\hbar\omega_i - \hbar\omega_0\right)^2}{\Delta E^2}\right), \tag{2.13}$$

where i is the group number from 1 to N, ΔE is energy of the full-width at half-maximum (FWHM), $\hbar\omega_0$ is transition energy at the gain peak frequency, $\hbar\omega_i$ is the transition energy of each QD group, and A is a normalization constant such that $\sum_{i=1}^{N} G(i) = 1$. QDs are divided into N groups, and within each group QDs are assumed to have the same transition energy and carrier density. After normalization, $G(i)$ represents the growth probability of QDs belonging to the i-th group. For each QD group, there is a Lorentzian shape linewidth corresponding to homogeneous broadening due to interband polarization dephasing process. The complex Lorentzian function in the frequency and time domains is given by

$$L_i(\Omega) = \frac{1}{1 + j\dfrac{\Omega - \left(\omega_i - \omega_0\right)}{\Gamma}}, \tag{2.14a}$$

$$L_i(t) = \Gamma \exp\left(j\left(\omega_k - \omega_0\right)\right)\exp\left(-\Gamma t\right) \tag{2.14b}$$

where $1/\Gamma$ is the characteristic dephasing time of the interband transition, ω_i is the centre frequency of the i-th QD group. The FWHM of the homogeneous linewidth is $2\hbar\Gamma$ where Γ is the dephasing rate. A homogeneous broadening model was used to explain the emission spectra of QD lasers. Due to the delta-function like DOS and spatial localization,

QDs with different transition energies lase independently at low temperature and the spectra is very broad by inhomogeneous linewidth. While at room temperature, QDs with different transition energies interact with each other through homogeneous broadening and the lasing spectra is narrowed by increased temperature [101]. The two cases are shown in Fig. 2.12. In Fig. 2.12 (a), homogeneous linewidth is very narrow compared with inhomogeneous linewidth at low temperature, and in Fig. 2.12 (b), they are comparable at room temperature. The optical spectra as a function of current for the two cases are shown in Fig. 2.13. At the low current of 1.5 mA, the spectrum is very broad due to spontaneous emission in both Fig. 2.13 (a) and (b). At $\hbar\Gamma_{cv} = 1$ meV (homogeneous linewidth), all dots start lasing independently if the gain is larger than the loss, leading to a very broad spectrum of over 25 meV at 10 mA. At $\hbar\Gamma_{cv} = 10$ meV, dots compete within the range of the homogeneous linewidth and lasing occurs only at the centre modes, resulting into a narrow peak in the spectrum. At 80 K, the broad band emission of over 50-60 meV has been found. At room temperature (298 K), the homogeneous broadening could reach 16-19 meV, corresponding to the dephasing time of 70-80 fs [102].

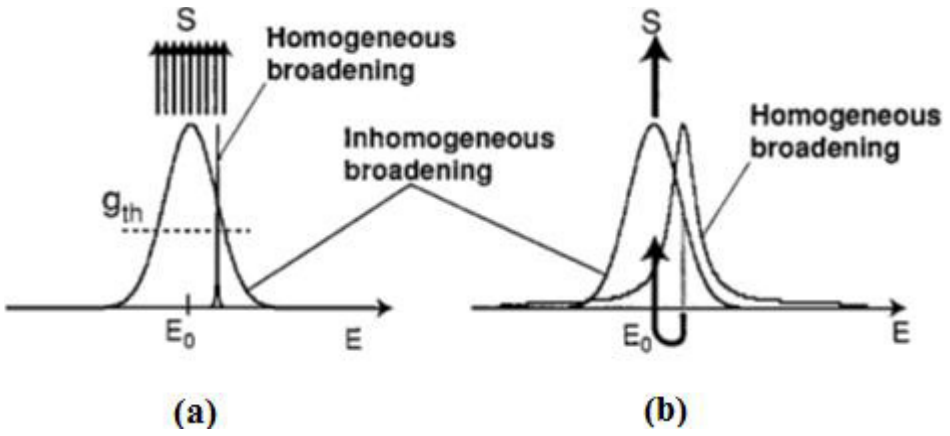

Fig. 2.12. Inhomogeneous and homogeneous broadening at (a) low temperature and (b) room temperature [101].

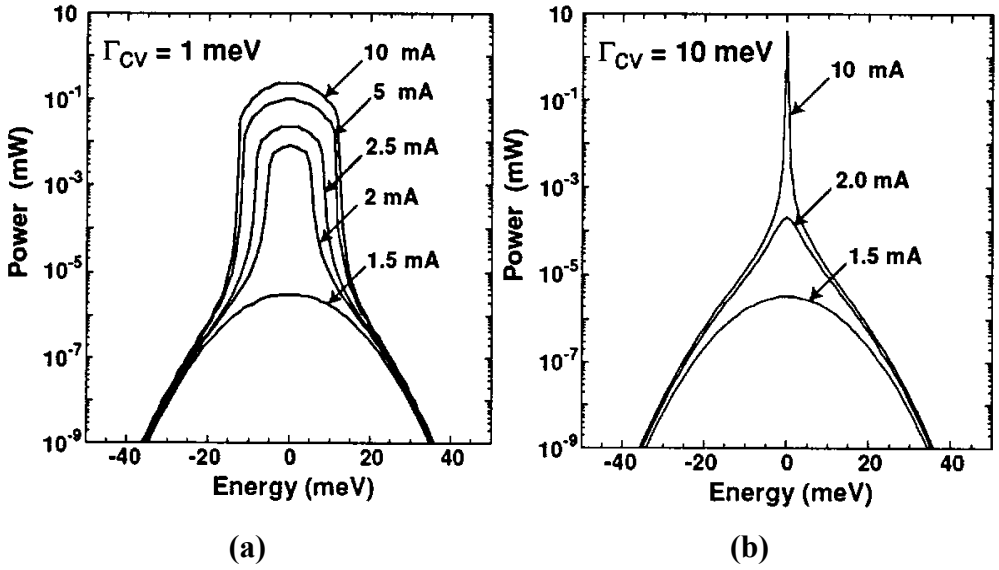

Fig. 2.13. Emission spectra change with the increase of current for homogeneous linewidth of (a) 1 meV and (b) 10 meV. The inhomogeneous broadening is 20 meV [101].

The total gain in the frequency domain can be expressed through dipole matrix element as [103]

$$g(E) = \sum_k \sum_i \frac{\omega_0 D_k G_i N_d}{cnH_w \varepsilon_0} \frac{\left|d_k^i\right|^2 \left(f_{c,k}^i - f_{v,k}^i\right)}{\hbar\Gamma} \mathrm{Re}\left\{L\left(E - \left(E_k^i - E_0\right)\right)\right\} \qquad (2.15)$$

where N_d is the dot density per unit area, D_k is the degeneracy of QD state, G_i is growth probability of the *i*-th QD group, *n* is the refractive index, H_w is the QD height, d_k^i is the dipole matrix element, $f_{c,k}^i$ is the electron occupation probability in the conduction band, $f_{v,k}^i$ is the electron occupation probability in the valence band, the subscript *k* represents energy states of QDs (GS, ES etc.), *i* represents QD group number, and the real part of the L function represents the homogeneous broadening given above. The homogeneous gain of each group and the total gain are illustrated in Fig. 2.14. Each Lorentzian curve at the lower part of the figure corresponds to homogeneous gain of each QD group *i* with centre frequency ω_i. The total gain equals to the sum of all QD contributions. The real part of the Lorentzian function for each QD group centred at $E_k^i - E_0$ is illustrated in Fig. 2.15 (a). The total gain $g(E)$ at energy E receives gain not only from local group but also from other groups of dots within the broadening range, weighted by the occupation probability and the Lorentzian function.

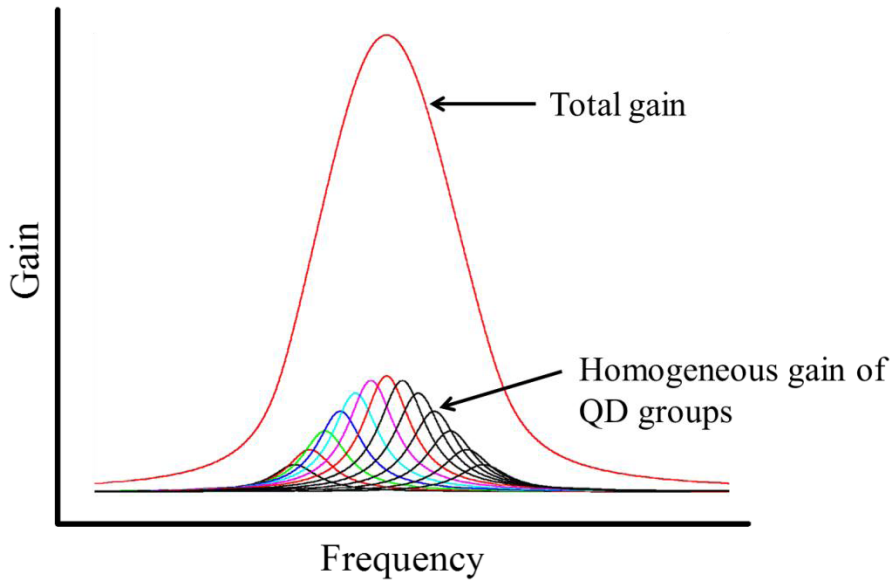

Fig. 2.14. Illustration of the contribution of gain from each QD group to the total gain.

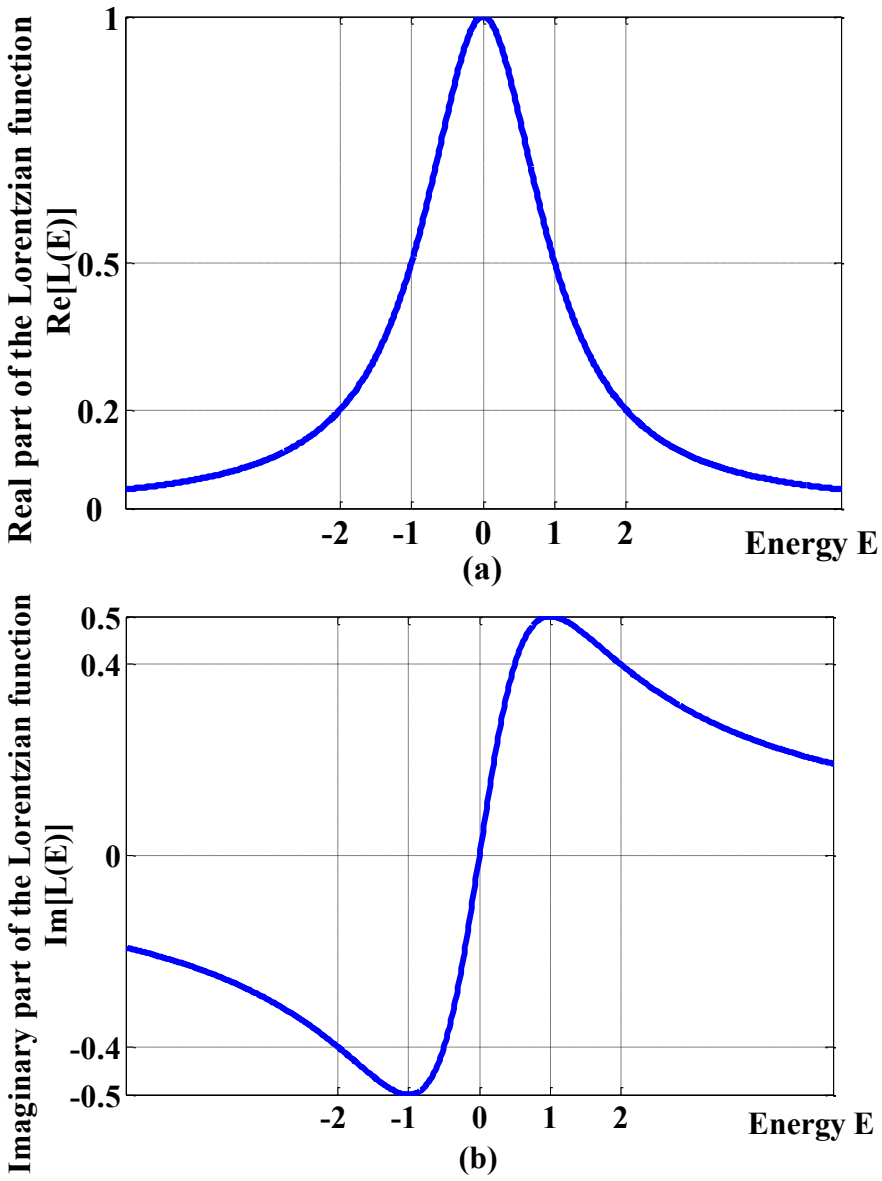

Fig. 2.15. (a) The real part of the Lorentzian function in the expression of gain in Eq. (2.15). (b) The imaginary part of the Lorentzian function in the expression of refractive index in Eq. (2.17). The x-axis is normalized by $\hbar\Gamma$ and the centre is shifted by $E_k^i - E_0$.

2.5.1.3 Polarization

The polarization can be expressed through the electronic susceptibility χ. The optical susceptibility is given as [61]

$$\chi(E) = \Gamma_{xy} \sum_k \sum_i \frac{\omega_0 D_k G_i N_d}{H_w \varepsilon_0} \frac{j\left|d_k^i\right|^2 \left(f_{c,k}^i - f_{v,k}^i\right)}{\hbar\Gamma} L\left(E - \left(E_k^i - E_0\right)\right) \qquad (2.16)$$

The QD gain and refractive index are related to the imaginary and real parts of the susceptibility, respectively. Similarly, the refractive index change can be expressed in the same way as gain as

$$\begin{aligned} \Delta n(E) &= \frac{1}{2n} \mathrm{Re}\left\{\chi\left(E\right)\right\} \\ &= \Gamma_{xy} \sum_k \sum_i \frac{D_k G_i N_d}{n H_w \varepsilon_0} \frac{\left|d_k^i\right|^2 \left(f_{c,k}^i - f_{v,k}^i\right)}{\hbar\Gamma} \mathrm{Im}\left\{L\left(E - \left(E_k^i - E_0\right)\right)\right\} \end{aligned} \qquad (2.17)$$

where $\mathrm{Im}\{L\}$ represents the imaginary part of the Lorentzian function, which is responsible for the broadening of the refractive index. The imaginary part of the Lorentzian function versus energy is plotted in Fig. 2.15 (b). The refractive index at the lasing energy E will be affected by the carrier density variation in the state E_k^i due to this broadening effect. By comparing Fig. 2.15 (a) and (b), it is seen that the broadening effect of the refractive index given by $\mathrm{Im}\{L\}$ is much broader than that of the gain given by $\mathrm{Re}\{L\}$. Due to the broadness, LEF and frequency chirp at GS will be affected by the ES even no stimulated emission occurs at the ES.

By replacing Eq. (2.16) into the modified polarization, Eq. (2.10) is written as

$$P^{\pm}\left(z,t\right) = \frac{\omega_0}{2cn_g} \tilde{\chi}\left(z,t\right) \otimes E^{\pm}\left(z,t\right) = \sum_i \sum_k p_{i,k}^{\pm}\left(z,t\right) \qquad (2.18)$$

where $p_{i,k}^{\pm}\left(z,t\right)$ is the polarization contributed from each QD group and is written as

$$p_{i,k}^{\pm}(z,t) = \Gamma_{xy} \frac{\omega_0 D_k G_i N_d}{2cnH_w \varepsilon_0} \frac{j\left|d_k^i\right|^2 \left(f_{c,k}^i - f_{v,k}^i\right)}{\hbar\Gamma} \left\{L_{i,k}\left(t\right) \otimes E^{\pm}\left(z,t\right)\right\} \qquad (2.19)$$

where Γ_{xy} is the confinement factor in the QD layers and the symbol $\otimes$ represents convolution between the Lorentzian function and the electric field in the time-domain. Note that the occupation probability term $\left(f_{c,k}^{i}-f_{v,k}^{i}\right)$ is not included in the convolution integral by the adiabatic approximation because the probability dynamics is much slower than the polarisation dephasing time (1/Γ). The optical response of the QD medium to the electric field is described by filtering the electric field through the Lorentzian function with different interband transitions.

In the literature, charge neutrality approximation is often assumed for all QD states (GS, ES), QW and barrier. Then the probability expression changes to

$$f_{c,k}^{i}-f_{v,k}^{i}=f_{c,k}^{i}-\left(1-f_{c,k}^{i}\right)=2f_{c,k}^{i}-1=2f_{i,k}-1 \tag{2.20}$$

where $f_{i,k}$ gives the probability to find an electron in the state *k* for the *i*-th group of QDs. This is referred as excitonic model which describes the behaviours of the electron-hole pairs in the cavity [104].

By introducing Eq. (2.18) into the travelling wave equation Eq. (2.9), the polarization term can be eliminated.

Then the TDTW equation Eq. (2.9) can be solved by finite difference scheme. The whole cavity is divided into sections with unit step Δz, and the corresponding unit time step is Δt. They have the relationship as $\Delta t=\frac{\Delta z}{v_g}$. The Δz should be small enough so that the electric field and carrier dynamics within each section does not change.

Eq. (2.9) in the frequency domain is a non-homogeneous equation, the solution of which can be written as the sum of a general solution corresponding to the homogeneous part and a particular solution corresponding to the non-homogeneous part. The step-by-

step solution is as follows. By replacing the polarization expression into the TDTW equation, using Fourier transform and the finite difference method, we get

$$E^{\pm}\left(z\pm\Delta z,\Omega\right)\cong\exp\left(-jn_g\frac{\Omega}{c}\Delta z\right)\left\{1-j\frac{\omega_0}{2cn_g}\tilde{\chi}\left(z,\Omega\right)\Delta z\right\}E^{\pm}\left(z,\Omega\right)+\Delta zF^{\pm}\left(z,\Omega\right) \quad (2.21)$$

where a 1st order expansion is taken in the derivation.

Converting back into the time-domain, we get

$$E^{\pm}\left(z\pm\Delta z,t+\Delta t\right)\cong E^{\pm}\left(z,t\right)-jP^{\pm}\left(z,t\right)\Delta z+F^{\pm}\left(z,t\right)\Delta z-\frac{\alpha_i}{2}E^{\pm}\left(z,t\right)\Delta z \quad (2.22)$$

where α_i is an additional term introduced to account for the cavity loss. For each Δz section, the electric field at time $t+\Delta t$ can be calculated from the field at the previous time point t.

The convolution term in the polarization expression in Eq. (2.19) needs to be further simplified. Use $I_{i,k}^{\pm}\left(z,t\right)$ to represent the convolution:

$$\begin{aligned}
I_{i,k}^{\pm}\left(z,t\right)&=L_{i,k}\left(t\right)\otimes E^{\pm}\left(z,t\right)=\Gamma\int_{-\infty}^{t}e^{j\left(\omega_{i,k}-\omega_0\right)t}e^{-\Gamma\left(t-\tau\right)}E^{\pm}\left(z,\tau\right)d\tau\\
&\simeq\Gamma\int_{-\infty}^{t-\Delta t}e^{j\left(\omega_{i,k}-\omega_0\right)\left(t-\tau\right)}e^{-\Gamma\left(t-\tau\right)}E^{\pm}\left(z,\tau\right)d\tau\\
&\quad+\frac{1}{2}\Gamma\Delta te^{j\left(\omega_{i,k}-\omega_0\right)\Delta t}e^{-\Gamma\Delta t}E^{\pm}\left(z,t-\Delta t\right)+\frac{1}{2}\Gamma\Delta tE^{\pm}\left(z,t\right)\\
&=e^{j\left(\omega_{i,k}-\omega_0\right)\Delta t}e^{-\Gamma\Delta t}I_{i,k}^{\pm}\left(z,t-\Delta t\right)+\frac{1}{2}\Gamma\Delta t\left[E^{\pm}\left(z,t\right)+e^{j\left(\omega_{i,k}-\omega_0\right)\Delta t}e^{-\Gamma\Delta t}E^{\pm}\left(z,t-\Delta t\right)\right]
\end{aligned} \quad (2.23)$$

Eq. (2.23) allows us to calculate the convolution at time t from the value at the previous time point t-Δt.

2.5.1.4 Spontaneous emission

The spontaneous emission rate is given by $R_k^{sp}\left(f_{c,k}^i, f_{v,k}^i\right) = \frac{1}{\tau_{sp,k}} f_{i,k}$, where $\tau_{sp,k}$ is the characteristic spontaneous emission time constant and can be calculated from Einstein approach as $\left(\tau_{sp,k}\right)^{-1} = \frac{\left|d_k^i\right|^2 n\omega_{i,k}{}^3}{\pi c^3 \varepsilon_0 h}$.

The spontaneous emission power per unit length, per unit bandwidth generated and coupled into the guided mode can be simply obtained by Einstein approach [105]:

$$\left|F^{\pm}\left(z,\Omega\right)\right|^2 = \frac{\beta_{sp}}{2} N_d W N_l \sum_{i=1,\ldots N} \sum_k G_i D_k \frac{\Gamma \hbar \omega_{i,k}}{\pi} R_k^{sp}\left(z,t\right) \mathrm{Re}\left\{L_{i,k}\left(\Omega\right)\right\} \qquad (2.24)$$

where β_{sp} is the spontaneous emission coupling factor accounting for the coupling of the total emission into the active region. The spontaneous emission generated in different slices of the cavity is random and independent. Assuming a group of independent complex random processes $\exp\left(j\varphi_{i,k}^{\pm}\left(z,t\right)\right)$ with zero mean and unit variance, where $\varphi_{i,k}^{\pm}\left(z,t\right)$ is uniformly distributed between 0 and 2π and are uncorrelated in time. To have the power spectral density given by Eq. (2.24), $\exp\left(j\varphi_{i,k}^{\pm}\left(z,t\right)\right)$ is filtered by the Lorentzian function $L_{i,k}$ and then the spontaneous emission noise term in the travelling wave equation is written as

$$F^{\pm}\left(z,t\right)\Delta z = \sum_{i=1,\ldots N} \sum_k \sqrt{\frac{\hbar \omega_{i,k}}{\pi \Gamma \Delta t} \frac{\beta_{sp} N_{i,k}\left(z,t\right)}{2\tau_k^{sp}}} I_{i,k}^{sp^{\pm}}\left(z,t\right) \qquad (2.25)$$

where $N_{i,k}\left(z,t\right)$ is the number of carriers in each Δz section, $I_{i,k}^{sp^{\pm}}\left(z,t\right)$ is the convolution of the Lorentzian function and the random process. The expression for $I_{i,k}^{sp^{\pm}}\left(z,t\right)$ is

$$I_{i,k}^{sp\pm}(z,t) = L_{i,k}(t) \otimes \mathrm{e}^{j\varphi_{i,k}^{\pm}(z,t)} = \Gamma \int_{-\infty}^{t} e^{j(\omega_{i,k}-\omega_0)(t-\tau)} e^{-\Gamma(t-\tau)}\, \mathrm{e}^{j\varphi_{i,k}^{\pm}(z,\tau)} d\tau$$
$$= e^{j(\omega_{i,k}-\omega_0)\Delta t} e^{-\Gamma\Delta t} I_{i,k}^{sp\pm}(z,t-\Delta t) + \frac{1}{2}\Gamma\Delta t\left[e^{j\varphi_{i,k}^{\pm}(z,t)} + e^{j(\omega_{i,k}-\omega_0)\Delta t} e^{-\Gamma\Delta t} e^{j\varphi_{i,k}^{\pm}(z,t-\Delta t)} \right] \quad (2.26)$$

2.5.1.5 Rate equations in the gain section

The electric field in the Fabry-Perot cavity is described by forward and backward travelling-wave equations combined with two boundary conditions of the two facets of the Fabry-Perot cavity. The electric field changed by the gain and refractive index is expressed through the polarization term. The gain, refractive index and the spontaneous emission is tightly related to the carrier distributions in the QD active medium. So the carrier dynamics described by the rate equations will be introduced in this section.

Since charge neutrality is assumed in all states, rate equations actually describe the dynamics of electron-hole pairs in the active medium, where the number of electrons in the conduction band equals to the number of holes in the valence band. The model is referred to as excitonic model. There is one rate equation for the separate confinement heterostructure (SCH) state, one for the WL and *N* for each confined QD state (GS, ES). The SCH state is a 3D bulk state where carriers are injected and the WL is a 2D state as a carrier reservoir. The QDs in the same group have the same characteristics and are described by one rate equation. Following the works in ref. [103, 106], the capture and escape of carriers exist only between two adjacent levels, such as SCH to WL, WL to ES_2, ES_2 to ES_1 and ES_1 to GS. The energy levels and time constants are illustrated in Fig. 2.16.

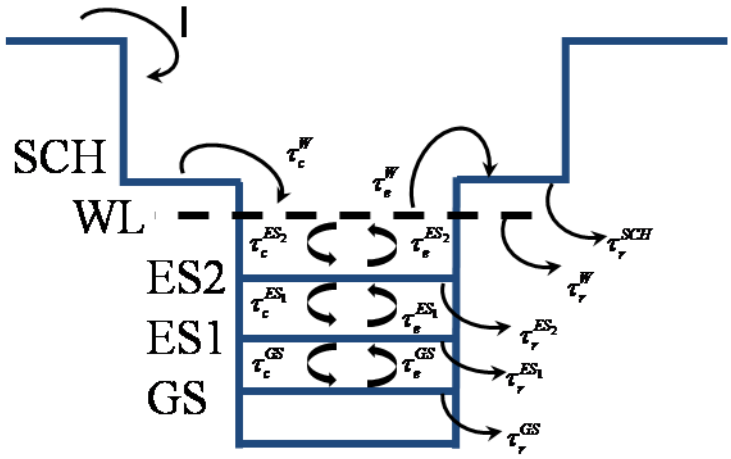

Fig. 2.16. Schematic of the energy band diagram of the active region of a typical QD laser. Intraband transitions are illustrated in the figure. *I* is the injected current, τ_r^k is the interband recombination time, including radiative and non-radiative recombinations, τ_c^k is the capture time to the state k and τ_e^k is the escape time from the state k.

The whole set of equations describing the carrier dynamics in the QD gain section is as follows [61]:

SCH state:
$$\frac{dN_{SCH}}{dt} = \eta_i \frac{J}{e}\Delta z W - \frac{N_{SCH}}{\tau_r^{SCH}} - \frac{N_{SCH}}{\tau_c^W} + \frac{N_W}{\tau_e^W} \tag{2.27}$$

WL:
$$\frac{dN_W}{dt} = \frac{N_{SCH}}{\tau_c^W} - \frac{N_W}{\tau_e^W} - \frac{N_W}{\tau_r^W} - \sum_{i=1}^{N}\frac{G_i}{\tau_c^{ES_2}} N_W\left(1-f_{iES_2}\right) + \sum_{i=1}^{N}\frac{N_{iES_2}}{\tau_e^{ES_2}} \tag{2.28}$$

ES2:
$$\begin{aligned}\frac{dN_{iES_2}}{dt} = {} & \frac{G_i}{\tau_c^{ES_2}} N_W\left(1-f_{iES_2}\right) - \frac{N_{iES_2}}{\tau_e^{iES_2}} - \frac{N_{iES_2}}{\tau_s^{iES_2}} \\ & - \frac{N_{iES_2}}{\tau_c^{ES_1}}\left(1-f_{iES_1}\right) + \frac{N_{iES_1}}{\tau_e^{iES_1}}\left(1-f_{iES_2}\right)\end{aligned} \tag{2.29}$$

ES1:
$$\begin{aligned}\frac{dN_{iES_1}}{dt} = {} & \frac{N_{iES_2}}{\tau_c^{ES_1}}\left(1-f_{iES_1}\right) - \frac{N_{iES_1}}{\tau_e^{iES_1}}\left(1-f_{iES_2}\right) - \frac{N_{iES_1}}{\tau_s^{iES_1}} - \frac{N_{iES_1}}{\tau_c^{GS}}\left(1-f_{iGS}\right) + \frac{N_{iGS}}{\tau_e^{iGS}}\left(1-f_{iES_1}\right) \\ & - \frac{j\Delta z}{\hbar\omega_{iES_1}}\left[\left(E^+ f_{iES_1}^{+\,*} - E^{+*} f_{iES_1}^{+}\right) + \left(E^- f_{iES_1}^{-\,*} - E^{-*} f_{iES_1}^{-}\right)\right]\end{aligned} \tag{2.30}$$

GS:
$$\frac{dN_{iGS}}{dt}=\frac{G_i}{\tau_c^{GS}}N_W\left(1-f_{iGS}\right)-\frac{N_{iGS}}{\tau_e^{iGS}}-\frac{N_{iGS}}{\tau_s^{iGS}} -\frac{j\Delta z}{\hbar\omega_{iGS}}\left[\left(E^+f_{iGS}^{+\,*}-E^{+*}f_{iGS}^{+}\right)+\left(E^-f_{iGS}^{-\,*}-E^{-*}f_{iGS}^{-}\right)\right] \tag{2.31}$$

where the subscript i is the group number, η_i is the internal quantum efficiency and J is the applied current density. Note that N_k and $N_{i,k}$ are the total carrier numbers per square meters at state k and group i within each longitudinal slice of size Δz. They are related with the occupation probabilities as [61]

$$N_{i,k}\left(z,t\right)=N_IN_DG_iD_kf_{i,k}\left(z,t\right)W\Delta z. \tag{2.32}$$

The last terms in Eq. (2.30) and Eq. (2.31) represent the stimulated emission and absorption in the GS and ES_1 states, respectively. Here the stimulated emission occurs in these two states but not the state ES_2. These last terms connect carrier dynamics with electric field and thus TDTW equations.

In the rate equations, the capture and escape rates strongly depend on the occupation probabilities of the initial and final states. They follow Pauli exclusion principle as

$$R_{k'\to k}\left(f_{i,k'},f_{i,k}\right)=\frac{f_{i,k'}\left(1-f_{i,k}\right)}{\tau_{k'\to k}} \tag{2.33}$$

where $\tau_{k'\to k}$ is the time constant defined as:

τ_r^k is the recombination time within each state k, k=SCH and WL

τ_c^k is the carrier capture time to the state k, k=WL, ES_2, ES_1, and GS

τ_e^k is the carrier escape time to the state k, k=WL, ES_2, ES_1, and GS

τ_r^k is the spontaneous emission recombination time in the state k, k=ES_2, ES_1, and GS

The carrier capture from SCH to WL has two parts: diffusion across the SCH region and the capture in the WL, that is $\tau_c^{WL} = \tau_{SCH \to WL} = \tau_{diff} + \tau_{cap}$. For other intraband transitions, the capture and relaxation times of electrons between other states are in the range of hundreds of fs to a few ps and are assumed to be constant, independent of carrier densities, to reduce the calculation complexity. With no external perturbations, quasi-equilibrium distribution holds for electrons in the conduction band and holes in the valence band. With this distribution, the relation between carrier capture and escape times involved in the same transition states is

$$\frac{\tau_{k \to k'}}{\tau_{k' \to k}} = \exp\left(\frac{\hbar\omega_{k'} - \hbar\omega_k}{k_B T} \right) \tag{2.34}$$

Thus the escape times are given by [103]

$$\tau_e^W = \tau_c^W \frac{DOS_W N_l}{DOS_{SCH} h_{SCH}} \exp\left(\frac{\Delta E_{SCH-W}}{k_B T} \right) \tag{2.35a}$$

$$\tau_e^{iES_2} = \tau_c^{iES_2} \frac{D_{ES_2} N_D}{DOS_W} \exp\left(\frac{E_W - \hbar\omega_{iES_2}}{K_B T} \right) \tag{2.35b}$$

$$\tau_e^{iES_1} = \tau_c^{iES_1} \frac{D_{ES_1}}{D_{ES_2}} \exp\left(\frac{\hbar\omega_{iES_2} - \hbar\omega_{iES_1}}{K_B T} \right) \tag{2.35c}$$

$$\tau_e^{iGS} = \tau_c^{iGS} \frac{D_{GS}}{D_{ES_1}} \exp\left(\frac{\hbar\omega_{iES_1} - \hbar\omega_{iGS}}{K_B T} \right) \tag{2.35d}$$

where DOS_{SCH} is the effective DOS per volume in the SCH, DOS_W is the effective DOS per area in the WL, D_{ES_2} is the degeneracy in the ES_2 state, D_{ES_1} is the degeneracy in the ES_1, D_{GS} is the degeneracy in the GS, N_l is the number of QD layers, N_D is the QD surface density and h_{SCH} is the thickness of the SCH.

The effective DOS in the SCH and the WL can be calculated as [103]

$$DOS_{SCH} = 2(2\frac{\pi m^*_{SCH} k_B T}{h^2})^{3/2} \tag{2.36a}$$

$$DOS_W = \frac{m^*_W k_B T}{\pi \hbar^2} \tag{2.36b}$$

where m^*_{SCH} and m^*_W are the electron effective masses in the SCH and WL, respectively.

2.5.1.6 Rate equations in the SA section

The travelling wave equations describing the electric field are applicable to the whole Fabry-Perot cavity. However, to describe a two-section MLL, additional rate equations are required for the reverse biased SA section. As shown in Fig. 2.17, due to the applied static electric field, the carrier dynamics and electric field change significantly in this section [88]. The applied electric field can lower the barrier height and enhance carrier escape rates from QD states to WL and WL to SCH. It can also lead to the formation of a triangular barrier, which allows for carrier tunnelling from confined QD states to SCH directly at high applied field. The carriers can be more efficiently swept out of the active region. Besides, the red shift of the carrier confined energies is observed due to the quantum confined stark effect. This effect is negligible compared to the other two and is not considered here.

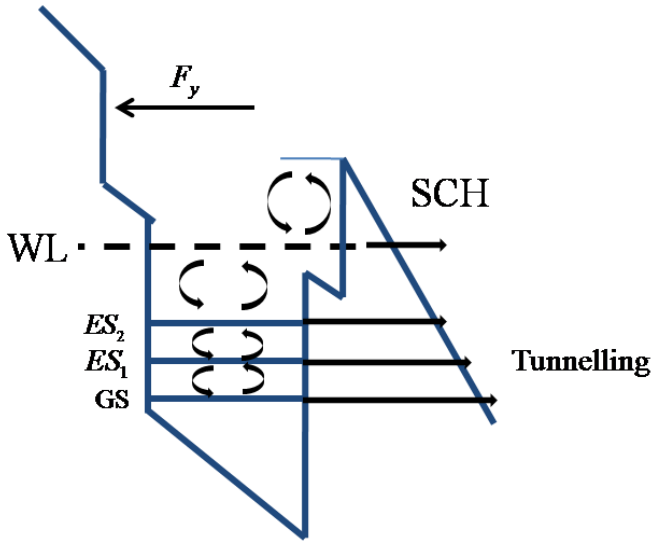

Fig. 2.17. Energy diagram with reverse biased voltage applied in the SA section. Barrier height reduction and tunneling process through the triangle barrier are indicated in the plot.

The barrier height can be lowered by $\Delta E = h_W |e| F_y / 2$, where h_W is width of the WL, e is the electron charge, and F_y is the reverse biased voltage caused electric field perpendicular to the p-i-n junction as shown in Fig. 2.17. F_y is calculated as $F_y = \frac{V + V_{bi}}{h_{SCH}}$, where V is the reverse biased voltage, V_{bi} is the built-in electric field of the junction [88].

Then the escape times become reverse-voltage-dependent. They are calculated as [88]

$$\tau_e^{iES_2}\left(F_y\right) = \tau_e^{iES_2}\left(0\right)\exp\left(-\frac{eF_y h_W}{k_B T}\right) \tag{2.37a}$$

$$\tau_e^{W}\left(F_y\right) = \tau_e^{W}\left(0\right)\exp\left(-\frac{eF_y h_W}{k_B T}\right) \tag{2.37b}$$

where $\tau_e^{iES_2}\left(0\right)$ and $\tau_e^{W}\left(0\right)$ are the escape times at zero reverse voltage ($F_y = 0$). The modified escape times are applied to the rate equations of ES_2 and WL for the SA section.

The tunnelling rates from the QD states and WL directly to SCH state can be calculated as the barrier collision frequency multiplying barrier transmission probability. The barrier transmission probability can be estimated by the Wentzel-Kramer-Brillouin approximation [88].

$$R_{tun,k} = f_{tun} \exp\left(-\frac{4}{3} \frac{\sqrt{2m^*_{SCH}} \left(\Delta E_{SCH-k}\right)^{\frac{3}{2}}}{e\hbar F_y} \right) N_k \tag{2.38a}$$

$$R_{tun,W} = f_{tun} \exp\left(-\frac{4}{3} \frac{\sqrt{2m^*_{SCH}} \left(\Delta E_{SCH-W}\right)^{\frac{3}{2}}}{e\hbar F_y} \right) N_W \tag{2.38b}$$

where the subscript k represents QD states, $f_{tun} = \dfrac{\hbar\pi}{2m^*_k h_w^2}$ is the barrier collision frequency and N_W (N_k) is the carrier density in the WL (QD states).

With this newly introduced parameter, we can now update rate equations for the SCH state in the SA section.

$$\frac{dN_{SCH}}{dt} = -\mu_d N_{SCH} \frac{V + V_{bi}}{h_{SCH}^2} - \frac{N_{SCH}}{\tau_{nr}^{SCH}} - \frac{N_{SCH}}{\tau_c^W} + \frac{N_W}{\tau_e^W} + R_{tun,W} + \sum_k R_{tun,k} \tag{2.39}$$

where μ_d is the electron mobility of the barrier material. This equation and rate equations of the WL and confined QD states with modified carrier escape times can be applied to describe carrier dynamics in the SA section.

Up to now, complete description of TDTW equations for propagation electric fields and rate equations for carrier dynamics has been presented. In the next section, the numerical method for solving the whole set of equations will be given.

2.5.1.7 Reference frequency ω_0 and the time step Δt

The reference frequency ω_0 is chosen to ensure the validity of the slow varying envelope approximation. It is usually chosen to be close to the lasing frequency. If both GS and ES are lasing, the reference frequency ω_0 can be set to the centre of the two emission peaks, i.e. $\omega_0 = \left(\omega_{(N+1)/2,GS} + \omega_{(N+1)/2,GS}\right)\Big/2$. If only GS level is lasing, it can be set to the GS emission peak of the central QD group, i.e. $\omega_0 = \omega_{(N+1)/2,GS}$. But additional contribution from the ES to the refractive index at the GS is required to be considered in the TDTW equation. With the unit time step Δt, the simulation bandwidth is then in the range of $[\omega_0 - \frac{\pi}{\Delta t}, \omega_0 + \frac{\pi}{\Delta t}]$. The simulation bandwidth needs to cover all QD transitions. Besides, the Lorentzian function describing the homogeneous broadening has long tails in the frequency domain (see Fig. 2.15) that may be beyond the bandwidth $\pi/\Delta t$ when Δt is not chosen small enough. Thus a small time step of Δt is required for simulation accuracy. However, computation cost is increased accordingly.

2.5.1.8 Numerical model implementation

With the unit step of the time Δt selected, the unit step Δz along the Fabry-Perot cavity can be fixed. Then the whole cavity is discretized into $L/\Delta z$ subsections and each subsection is either forward or reverse biased. After initializing the parameters, the following steps are performed.

1. $f_{i,k}(z,t), z = 1...L, k = ES_2, ES_1, GS$

The probabilities of ES_2, ES_1 and GS states for each group of QDs at time t are obtained through carrier densities $N_{i,k}(z,t)$ at time t by Eq. (2.32)

2. $P^{\pm}(z,t)$

The polarization terms are calculated according to Eq. (2.18)

3. $F^{\pm}(z,t)\Delta z$

The spontaneous emission in each Δz section is computed by Eq. (2.25)

4. $E^{\pm}(z,t+\Delta t)$

The forward and backward electric field at the next time $t+\Delta t$ can be calculated according to TDTW equation Eq. (2.22).

5. $N_k(z,t+\Delta t), k = SCH, WL$ and $N_{i,k}(z,t+\Delta t), k = ES_2, ES_1, GS$

The carrier densities at the next time $t+\Delta t$ can be updated by solving the rate equations using the first-order finite difference method. The rate equations for the gain and SA sections include Eqs. (2.27) to (2.31) and Eq. (2.39).

The above steps are repeated to compute the electric field and carrier dynamics until steady state is achieved.

2.5.2 Delayed differential model

The delayed differential equations (DDE) describing electric field in the cavity are directly derived from the TDTW equations. As shown in Fig. 2.18, the whole Fabry-Perot cavity is considered as a unidirectional ring cavity with three sections: the SA section from Z_2 to Z_3, the gain section from Z_3 to Z_4, and a filter as the bandwidth limiting element from Z_5 to Z_1+L, where L is the cavity length [107]. The electric field starting from the SA section is [108]

$$\gamma^{-1}\frac{\partial E(t)}{\partial t} + E(t) = \sqrt{a}e^{(1-i\alpha_g)G(t-T)/2-(1-i\alpha_q)Q(t-T)/2}E(t-T) \qquad (2.40)$$

where $E(t)$ is the normalized envelope of the electric field, γ is the dimensionless bandwidth of the filter, α_g is the LEF in the gain section, α_q is the LEF in the SA section, T is the cavity round trip time given by $T = L_{Ring}/v_g$ and a is the round trip cavity loss. Carrier dynamics in each section is described by the rate equations.

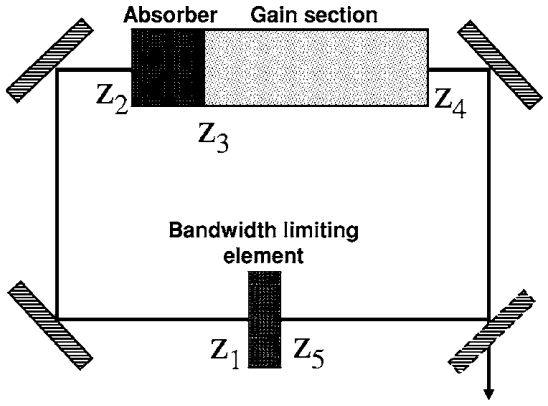

Fig. 2.18. Illustration of the ring cavity structure in the delayed differential model. Three sections are shown in the cavity [107].

$$\partial_t \rho_g = -\gamma_g \rho_g + F_g\left(\rho_g, N_g\right) - e^{-Q}\left(e^{G}-1\right)|E|^2 \tag{2.41a}$$

$$\partial_t \rho_q = -\gamma_q \rho_q + F_q\left(\rho_q, N_q\right) - s\left(1-e^{-Q}\right)|E|^2 \tag{2.41b}$$

$$\partial_t N_g = N_{g0} - \Gamma_g N_g - 2F_g\left(\rho_g, N_g\right) \tag{2.42a}$$

$$\partial_t N_q = N_{q0} - \Gamma_q N_q - 2F_q\left(\rho_q, N_q\right) \tag{2.42b}$$

where the subscript g represents the gain section, q represents the SA section, $N_{g,q}(t)$ is the carrier density in the WL, $\rho_{g,q}(t)$ is the occupation probability of the QD state and the function $F_{g,q}\left(\rho_{g,q}, N_{g,q}\right)$ describes carrier exchange between the WL and the QD layer. G and Q are dimensionless saturable gain and absorption given as

$$G(t) = 2g_g L_g\left[2\rho_g(t) - 1\right] \tag{2.43a}$$

$$Q(t) = -2g_q L_q \left[2\rho_q(t) - 1 \right] \tag{2.43b}$$

The definition of other parameters can be found in ref. [108]. The function $F_{g,q}\left(\rho_{g,q}, N_{g,q}\right)$ describes carrier exchange between carrier capture and escape and is written as

$$F_{g,q}\left(\rho_{g,q}, N_{g,q}\right) = R_{g,q}^{cap}\left(1-\rho_{g,q}\right) - R_{g,q}^{esc}\rho_{g,q} = B_{g,q}N_{g,q}\left(1-\rho_{g,q}\right) - R_{g,q}^{esc}\rho_{g,q} \tag{2.44}$$

where $B_{g,q}$ is the capture rate, $1-\rho_{g,q}$ is the Pauli blocking factor, and $R_{g,q}^{cap,esc}$ is the carrier capture and escape between the WL and the QD state. Carrier escape is a linear process proportional to the occupation probability $\rho_{g,q}$ while the capture process is nonlinearly proportional to $B_{g,q}N_{g,q}\left(1-\rho_{g,q}\right)$. The competing of the two processes results in the fast and slow recovery stages of the saturable gain and absorption. The two-recovery stage is a distinct feature in QD states. In the WL, however, the recovery is slow and almost linear, similar to that of QW lasers. The model can describe some general properties in QD mode-locking, especially the gain and absorber recovery processes. Additional effects can be easily included into the model to be studied.

In this delayed differential model, only two energy levels can be included, WL and GS. Then, a more generalized model, multi-section delayed differential equation (MS-DDE) model, was proposed to simulate ML in QD lasers as shown in Fig. 2.19 [109]. In the MS-DDE, the ring cavity is composed of a number of isolated sections either forward or reversely biased; intrinsic waveguide losses are treated within each section; and lasing from both GS and ES_1 states can be considered.

The equation for the electric field is [109]

$$E_k(\tau) = \left(\Gamma \exp\left(-\Gamma\tau\right)\right) \otimes \left(R_k(t-T)E_k(t-T)\right) \tag{2.45}$$

where τ is the coordinate given as $\tau = t - z/v_g$, $R_k(\tau - T)$ is the round trip gain and the first term is the Lorentzian bandwidth limiting filter. $R_k(\tau)$ is the product of gain and loss of all the F sections, including both amplitude and phase changes and it can be calculated as

$$R_k(\tau) = \prod_{i=1\sim F} B_{ki} M_i \tag{2.46}$$

where the subscript i is the subsection number, k is the QD state (GS or ES), the B_{ki} is the round trip gain/loss, M_i is the intrinsic waveguide loss. A stable ML is achieved when

$R_i(\tau - T) = R_i(\tau) = 1$ if $V_i(\tau) \neq 0$

$R_i(\tau - T) = R_i(\tau) < 1$ if $V_i(\tau) = 0$

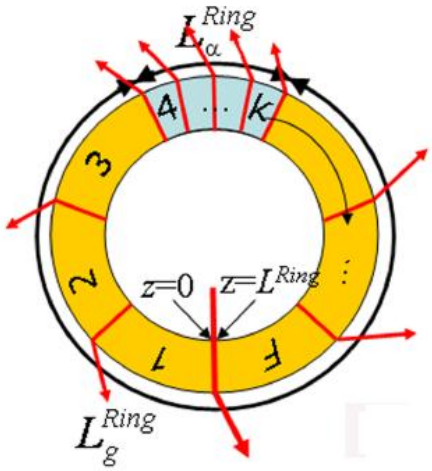

Fig. 2.19. Ring cavity structure in the MS-DDE model. Filter effect is modeled at z=0. Waveguide losses are considered at the interface between each two sections as indicated by the red lines. there are F sections in the figure where the yellow and blue areas represent gain and SA sections, respectively [109].

The gain/absorption can be expressed by the density matrix element, the same as in the TDTW model. The rate equations in the MS-DDE model are also the same as in the TDTW model except the stimulated emission rate which is calculated as

$$R_{k,i}^{stim}(\tau)=\left(\left|B_{ki}(\tau)\right|^2-1\right)\left(\prod_{m=1\sim k-1}\left|B_{ki}(\tau)\right|M_m^2\right)\frac{\left|E_k(\tau)\right|^2}{\hbar\omega_k L_i} \tag{2.47}$$

The MS-DDE model is then applied to an Fabry-Perot MLL and compared to the TDTW model. Differences are observed in optical power, pulse peak power and light-current efficiency. They are caused by the intrinsic discrepancy between the two modeling approaches [109]. However, the pulse widths as a function of injection currents are in good agreement for the two methods. Moreover, and the discrepancy is much reduced compared to the standard DDE model. Although not as precise as the TDTW model, the MS-DDE model is effective and accurate in modeling Fabry-Perot MLLs. And the computation cost is much lower which allows for extensively studying and analyzing parameters of QD MLLs.

2.6 Techniques for improvement of mode-locking performances

2.6.1 GS and ES switching

In the two-section laser, by altering the DC current of the gain section and the reverse bias of the absorber section, QD laser can switch operation between GS and ES. The lasing starts from the GS and is followed by the ES when the intensity of the GS becomes saturated. Stable mode-locking is demonstrated through both GS (1260 nm) and ES (1190 nm) in a two-section QD laser, with repetition frequencies of 21 and 20.5 GHz, respectively [110]. However, GS-lasing suppression or quench has been observed in a few experiments on 1.3 μm InAs/InGaAs QD lasers. As plotted in Fig. 2.20, the GS starts lasing at first. With the increase of the current, the total emission power is increased. However, once ES starts to lase, the GS emission is suppressed and gradually decreased to zero. Some possible explanations have been reported: self-heating leads to the increase

of substrate temperature and causes the degradation of GS emission [111]; electron-hole distribution asymmetry causes the transition from two states to single ES [112]; the homogeneous broadening leads to the decrease of optical gain with increased current; and slower capture rates in holes than in electrons combined with electron-hole distribution asymmetry [113].

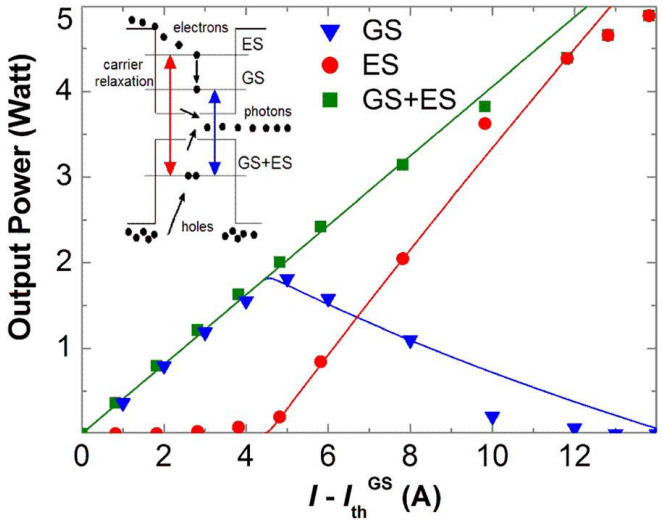

Fig. 2.20. GS-lasing suppression and quenching as a function of biased current. Energy bands and transitions are simply shown in the inset [113].

In order to independently study the lasing properties of each transition state, grating based external cavity could be applied to select GS or ES [114]. By changing the angle of the grating, pulse widths from the two states were measured to be 14 ps and 10.8 ps before dispersion compensation, in which the lasing from ES is not affected by the GS.

2.6.2 Pulse duration shortening

In the two-section QD MLLs, the absorption in the SA section provides the dominant pulse shortening mechanism. Pulse widths can be shortened by increasing the applied reverse bias to speed up the recovery of the SA. The pulse duration is shortened from 2 ps to 390 fs by optimizing the current/voltage parameters at the repetition rate of 21 GHz by

Rafailov et al in 2005 [115]. On the contrary, the average output power and pulse durations increase with the increase of the biased gain-section current. The lengths of the two sections also affect mode-locking pulses. Pulse shortening could be realized by using smaller gain-to-absorber length ratio to increase the absorption but at the expense of decreased peak power [116]. Additional pulse shortening may be obtained by increasing the carrier escape rate out of the QDs. The shortest pulse width at 30ºC is 5.1 ps while at 60ºC is 3.2 ps possibly by thermal-induced faster rate of carrier escape [117].

Besides, the pulse can be further shortened with external structures, such as dispersion compensation fibers and grating based dispersion compensator in the external cavity. In both methods, linear chirp is compensated. By using a 90-m single mode fiber, the pulse from a 42.72 GHz QDash MLL was compressed from 4.7 ps to 1.1 ps [118]. The pulse width of 15 ps was compressed to 1.2 ps by using a dual grating dispersion compensator [31]. And the time-bandwidth product (TBP) is decreased from 6 to 0.69 after the chirp compensation. The larger TBP value before the compression implies highly chirped pulses generated in the cavity. The large chirp in the device can also be decreased by the bias condition of the two sections. By using the same dual-grating, the pulse width was also compressed to 970 fs from 14 ps for the GS transition and 1.2 ps from 10.8 ps for the ES transition [114].

2.6.3 Repetition rate

The lowest repetition rate reported from monolithically passive QD MLLs is 2.1 GHz [53]. To achieve even lower repetition rate, external cavity combined with QD gain material has been employed. Then the total cavity length equals to the QD cavity plus the external cavity length. Although the external cavity configuration increases the

complexity, it has advantages of repetition rate tunability, wavelength selection and dispersion compensation. The configuration of a typical external cavity mode-locked laser (ECMLL) is illustrated in Fig. 2.21, where the light emitting from the gain facet is focused on a reflection element through a lens fiber. The first external cavity laser was reported by Choi et al. in 2005 where low repetition rate of 5 GHz was demonstrated. To construct the external cavity, one facet of the two-section laser is curved to reduce back reflection and an external mirror is used instead. The ECMLL can improve noise performance with reduced active length for the same repetition rate generated from a monolithic laser [31]. Low repetition rate of 1.14 GHz with an average power of 23.2 mW, and 2.4 GHz with an average power of 60 mW were demonstrated using an ECMLL including a 96% coupler and a two-section QD laser with one antireflection coated facet and bending ridge waveguide [39]. Alternatively, a semiconductor SESAM that contains 35 layers of InAs QDs is used as the SA in the external cavity to generate pulses with repetition rates from 350 MHz to 1.5 GHz. The SESAM has the function of both reflection mirror and SA. It has fast recovery time for ultra-short pulse generation [119]. By the same group, tuning range of 1 GHz to record-low value of 191 MHz was reported from an ECMLL with cavity length from 15 to 78.5 cm [120]. To get stable fundamental rather than harmonic ML, the external reflection back to the QD cavity should be adjusted for each operation case. And at the repetition rate of 281 MHz, the 3-dB RF linewidth was measured to be ~30 Hz at the current of 300 mA and the reverse biased voltage of 8V, which is the narrowest value ever in passive mode-locked semiconductor lasers. The narrow RF linewidth indicates low noise and high stability in the ECMLL.

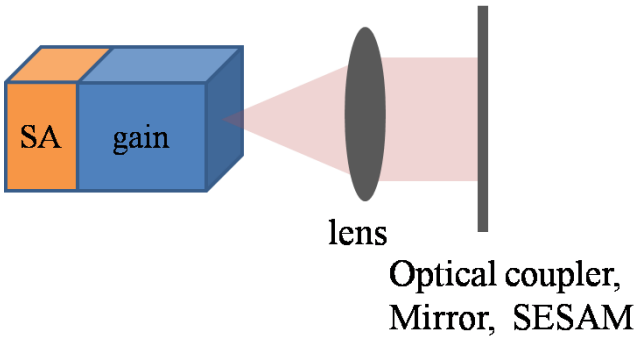

Fig. 2.21. Configuration of an external cavity QD MLL. The elements include a two-section QD laser, a coupling lens/an optical coupler and a mirror or SESAM (no SA required in the QD cavity for SESAM).

On the other hand, the direct way to increase the repetition rate is to decrease cavity length. The highest repetition rate generated is 80 GHz from a two-section passive QD MLL and 346 GHz from a single-section QDash MLL by exploiting a higher optical confinement factor. The repetition rate is inversely proportional to the cavity length, which imposes a limit for realizing higher repetition rates due to reduced gain from short cavities. The higher repetition rate is also limited by the absorber recovery time in two-section QD MLLs. In two-section QD MLLs, harmonic mode-locking is another effective method for high repetition rate pulse generation without the challenge of reduced gain. In order to support multiple pulses circulating in the cavity, higher drive current is required to increase the gain. Harmonic repetition rates of 2.2, 3.3, and 4.4 GHz were generated with increased drive currents based on the fundamental ML of 1.1 GHz with a 14-cm-long cavity [51]. In a colliding pulse MLL, the SA is placed in the centre of the cavity and the second harmonic is excited. The 1st colliding pulse ML was demonstrated by M. Thompson et al. using a 3.9 mm-long cavity with a 245-µm-long absorber, and the obtained repetition rate was 20 GHz, twice of the 10-GHz fundamental resonance [28, 121]. Mode-locking at the 1st, 2nd, 3rd, 6th harmonics was demonstrated by Rae et al. in

2006, which correspond to repetition rates from 39 GHz to 238 GHz. In the device, the p-contact is divided into a number of multi-contact isolated sections and the SA section can be placed at the position corresponding to the desired harmonic [32].

In addition, higher repetition rates of up to 1.1 THz have been demonstrated in InAs/InP single-section QD MLLs [55, 122, 123].

2.6.4 Injection locking

Injection locking is often applied to improve the performance of single mode lasers. Its effect on QD MLLs has also been studied. It is found that single-tone injection can significantly narrow the optical spectrum of QD MLLs but has almost no effect on the pulse width [124]. The TBP, given by the product of the two parameters, is thus reduced. When close to the injection wavelength, the longitudinal modes are locked to the injected light and the mode linewidth is reduced as well as phase noise. But the linewidth of the longitudinal modes is not reduced when far from the injection wavelength.

To further improve the noise performance of QD MLLs, dual-tone injection locking is used. Dual-mode light, separated by the resonance frequency of the QD MLL, was injected into a QD MLL and close to a pair of its longitudinal modes. Then the emission spectrum of the QD MLL was narrowed and moved with the injection wavelength. The TBP is reduced by 10 to 15 times compared to the free-running one. The linewidth of free-running QD MLL has a parabolic dependence on the mode wavelength, varying from 10 to 40 MHz while the dual-injection locked linewidth is about 100 kHz for all longitudinal modes. The timing jitter is also greatly decreased from 11~21 ps to 1~300 fs in the range of 20 kHz-80 MHz. The chirp, optical linewidth and phase noise of the MLL has been significantly improved by this method [50]. And the reduction is also observed

at triple-tone injection or when the dual-mode separation is increased to three times of the resonance frequency [124].

Injection locking has also been applied between two separate QD MLLs. The repetition rates of the two lasers are the same and the spectrum of the master laser is partially overlapped with the slave laser. Due to the overlap, coherent coupling occurs between the two spectra, and the bandwidth of the slave laser is expanded resulting in pulse width shortening. And the TBP is not significantly changed [125].

2.6.5 Noise reduction

Noise performance in QDs is improved due to reduced spontaneous emission, high gain saturation energy, and small LEF, etc. Spontaneous emission in QDs is greatly reduced, which suppresses fluctuations in the carrier density, refractive index and thus the round-trip time. The RF linewidth is also related to the laser cavity configurations. For example as illustrated in Fig. 2.22, the RF linewidth increases with the decreased gain-to-absorber length ratio from 7:1 to 3:1. It is impossible to obtain the minimum pulse durations and lowest RF linewidth at the same time. The pulse width shows an opposite tendency [116] in Fig. 2.22. There is a trade-off between the two parameters in the design.

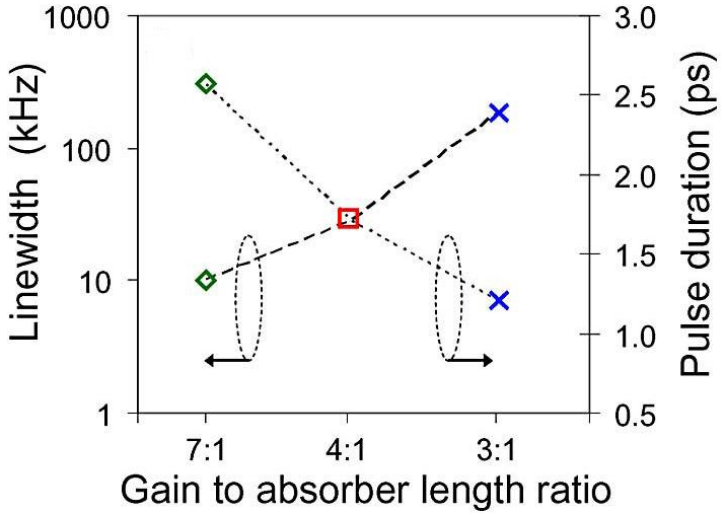

Fig. 2.22. RF linewidth and pulse duration at different gain-to-absorber length ratios of a 20 GHz QD MLL [116].

It has also been shown that external optical feedback or injection can largely improve the RF linewidth/timing jitter of MLLs. And the improvement is sensitive to both the feedback level and the fiber loop length of the external cavity [126]. The RF linewidth was narrowed from 1 MHz to 500 Hz with external optical feedback [127]. The lowest RF linewidth reported so far is 350 Hz which is reduced from 8 KHz by using the optical feedback. The RF principal peak in the spectrum can be stabilized by an external optical fiber cavity [128]. Besides, significant improvement in RF linewidth was demonstrated by phase-locking a QD MLL to a master laser using dual-mode optical injection [50].

2.7 Conclusion

This chapter provides an extensive review on the basic characteristics of QDs and QD lasers. The delayed differential and TDTW models have been widely applied in theoretically analyzing mode-locking performance in two-section semiconductor MLLs including QD MLLs. The TDTW model will be improved and applied to our single-

section QD MLLs in Chapter 4. The external cavity structure combined with QD cavity has demonstrated low repetition rate pulses and reduced phase noise. It will be used to increase the pulse repetition rate in our experimental work in Chapters 5 and 6.

In the following chapters, our research work on single-section QD MLLs will be given in detail.

Chapter 3 Investigation of Linewidth Enhancement Factor of InAs/InP QD Lasers

3.1 Introduction

As introduced in the previous chapter, the LEF is an important parameter of semiconductor lasers. It determines many fundamental properties of QD lasers, such as linewidth, filamentation in high power lasers [129], feedback sensitivity [130], frequency chirping and timing jitter of mode-locked lasers [76]. The LEF value can be measured by methods of Hakki-Pauli [79] and injection locking [131]. Small LEF values of less than 1 in InAs/GaAs QD lasers and SOAs have been obtained [82, 132, 133]. To reach the most important 1.5 μm wavelength range for telecommunication applications, many efforts have been put to develop QD lasers [134, 135] and SOAs [84] operating around 1.5 μm. However, only a few groups have reported their experiments to quantify LEF of InAs/InP QD lasers, and the LEF are in the range of 2.2 to 7.6 [136, 137].

In this chapter, the LEF parameter of an InAs/InP QD multi-wavelength laser (MWL) with the centre wavelength of 1.53 μm is investigated for the first time. The injection locking technique is used to evaluate the above-threshold LEF. The LEF can be directly deduced from the positive and negative locking bandwidth without using other fitting parameters. The LEF is found to be only 1.37 at the gain peak of 1.53 μm. Then the result is confirmed by the Hakki-Pauli method which shows a reduced LEF of less than 1 just below threshold. The measured small LEF values have indicated that our developed InAs/InP QD gain materials will lead to ultra-narrow linewidth of QD distributed feedback (DFB) lasers [138], much less sensitivity of QD MWLs [139] to optical

feedback [140], and also lead to a lower frequency chirp and timing jitter of QD MLLs [69, 84] which are suitable for very high data rate transmission systems [141].

3.2 Injection locking method

3.2.1 Experimental setup

The InAs/InP QD laser wafers used in this study were grown by CBE on exactly (100) oriented n-type InP substrates. The undoped active region of the QD sample consisted of five stacked layers of InAs QDs with $In_{0.82}Ga_{0.18}As_{0.39}P_{0.61}$ (1.15Q) barriers. The QDs were tuned to operate in the desirable operation wavelength range by using a QD double cap growth procedure and a GaP sublayer [142]. In the double cap process the dots are partially capped with a thin layer of the barrier material, followed by a 30 second growth interruption and then complete capping. The thickness of the partial cap controls the height of the dots, and hence their emission wavelengths. It also helps to control the height distribution of the dots, and therefore control the 3-dB spectral bandwidth of the gain spectrum. Growing the dots on a thin GaP layer allows a high dot density to be obtained and improves layer uniformity when stacking multiple layers of dots, providing maximum gain. This active layer was embedded in a 355 nm thick 1.15Q waveguiding core, providing both carrier and optical confinement. An average dot density of approximately 4×10^{10} cm^{-2} per layer was obtained according to our atomic force microscopy measurement on uncapped stacked dot samples. The waveguiding core was surrounded by p-doped (top) and n-doped (bottom) layers of InP and capped with a heavily doped thin InGaAs layer to facilitate the fabrication of low resistance Ohmic

contacts. The sample was fabricated into single lateral mode ridge waveguide lasers with a ridge width of 3 μm, and then cleaved to form an Fabry-Perot laser cavity.

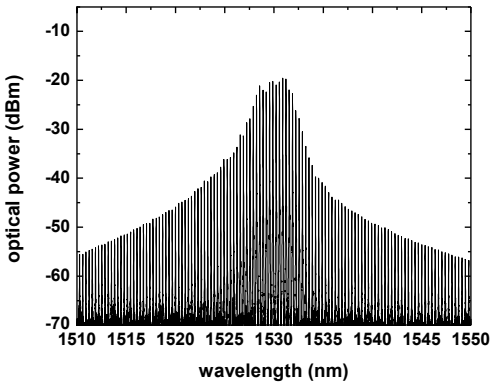

Fig. 3.1. Typical spectrum of an InAs/InP QD multi-wavelength laser with the injection current of 60 mA at 18°C.

The laser was driven by a DC current, and tested on a heat sink maintained at 18°C. The threshold current is 45.5 mA under CW operation. Fig. 3.1 shows the typical spectrum of a C-band QD MWL with DC current of 60 mA. The experimental setup used in the LEF measurement by injection locking method is shown in Fig. 3.2. A tunable laser (Agilent 8164B) worked as the master laser is used to lock the QD MWL (slave laser). The master laser has a wavelength accuracy of 0.1 pm. Output light from the master laser is injected into the slave laser through one port of a polarization-maintaining (PM) circulator. A single mode lensed fiber is used to lead light from the master laser into the slave laser and receive light from the slave laser after locking. The PM circulator ensures light transmission in only one direction. A power meter and a high resolution (10 pm) optical spectrum analyzer (OSA) are connected to two ports of a 3-dB coupler to monitor the power and the spectrum simultaneously.

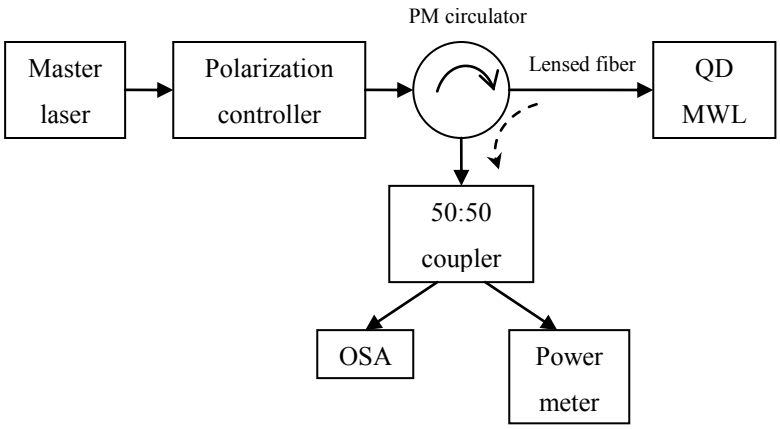

Fig. 3.2. Schematic diagram of measuring the LEF factor using injection locking method.

When light from the master laser is injected into the QD MWL, i.e. the slave laser, the injected light competes with all longitudinal modes of the slave laser. At the locked state, the slave laser emits at the injected wavelength of the master laser while gain at other wavelengths is highly suppressed. While at the unlocked state, the total spectrum shows the sum of the two. The locked and unlocked conditions are dependent on power of the injected light and frequency detuning from the closest longitudinal mode of the slave laser. The locking bandwidth is given by the formula [143]

$$r\sqrt{1+\alpha^2} = \Delta\omega_{negative} < \Delta\omega < \Delta\omega_{positive} = r \tag{3.1}$$

where $r = (c/2nL)(P_i/P)^{1/2}$ is the injection rate, P_i is the injected power from the master laser, P is the power of the slave laser, n is the refractive index and α is the LEF of the slave laser. Locking is achieved within the detuning range given in Eq. (3.1). It is obvious that the positive and negative locking range is asymmetric, which can be used to calculate the LEF. It is given by [143]

$$\alpha = \sqrt{\left(\frac{\Delta\omega_{negative}}{\Delta\omega_{positive}}\right)^2 - 1} \tag{3.2}$$

3.2.2 Experimental results

In the experiment, the slave laser was pumped by a CW injection current of 60 mA and the temperature was controlled at 18°C. Three different wavelengths at 1524.24 nm, 1529.53 nm and 1535.52 nm are selected to measure the LEF which cover the main gain region as shown in Fig. 3.3. The locking condition is reached when at least 30 dB side-mode suppression ratios (SMSRs) are observed on the OSA for each injected power. The detuning frequency at both positive and negative sides increases with injected power of the master laser as shown in Fig. 3.3. By linear fitting, the LEF is calculated as the ratio of the two slopes of detuning ranges [131] using Eq. (3.2). The LEF values at the three wavelengths are 1.63, 1.37 and 1.59, respectively. To our best knowledge, it is the lowest values reported so far for QD lasers emitting around 1.5 μm based on the substrate of InP.

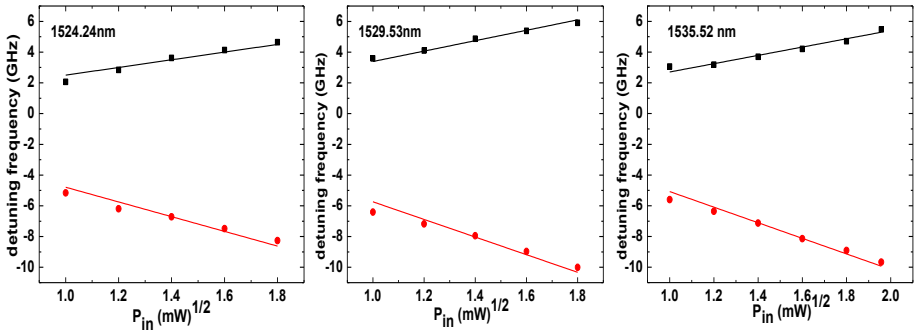

Fig. 3.3. Positive detuning and negative detuning as function of square root of injected power from the ML at three different wavelengths. The solid lines are linear fitting of experimental results.

3.3 Hakki-Pauli method

The LEF obtained by the injection locking technique is a reflection of the laser's working performance at lasing while the Hakki-Pauli method is the one to know the key properties of lasers. In order to remove the influence of heating to the change of refractive index, a

pulse generator (Agilent 8114A) was taken to provide pulsed current. Pulse width of 400 ns and duty cycle of 2.5% were used in the experiment. In this method, the LEF is calculated as [79]

$$\alpha = \frac{-4\pi}{\lambda}\frac{dn/dN}{dg/dN} = -\frac{4\pi n}{\lambda^2}\frac{d\lambda/dN}{dg/dN} \tag{3.3}$$

where n is the refractive index, g is the net modal gain, and N is the carrier density. It shows the relationship between change of refractive index and gain caused by the variation of carrier density in the active region. The net modal gain is given by $g = \frac{1}{L}\ln\frac{\sqrt{r}-1}{\sqrt{r}+1}$, where L is the cavity length and r is the peak to valley ratio of each longitudinal mode in the amplifier spontaneous emission (ASE) spectrum of the QD MWL. And the refractive index change can be obtained by measuring the frequency shift of each peak in the ASE spectrum. Under pulsed condition, output power is low below threshold so only 1 nm of the ASE spectrum around the gain peak was analyzed to get gain and wavelength shift. Three peaks are observed within the 1 nm range from 1529.5 to 1530.5 nm. Blue shift of wavelength and increase of gain are observed with increased current. Wavelength shifts against gains at the three peaks are shown in Fig. 3.4 for injection currents from 42 to 44 mA ($I_{th} \approx 45.5\ mA$) with 0.5-mA step.

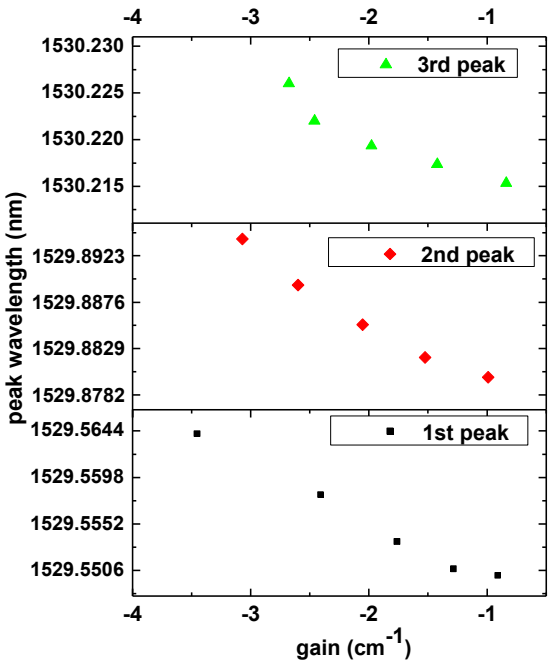

Fig. 3.4. Wavelength shift as a function of gain for three longitudinal modes within the spectrum span of 1 nm around the gain peak. In each graph, five points correspond to five current levels from 42 mA to 44 mA by 0.5-mA step.

The refractive index n is determined by the channel spacing between two longitudinal modes and is about 3.52 for the cavity length of 1 mm. Then the LEF calculated by Eq. (3.3) is shown in Fig. 3.5. The LEF value decreases with increased current [82, 144] and is reduced to be less than 1 at 43.5 mA. The smaller α factor below the threshold as compared with LEF value above the threshold is consistent with the other analysis [145].

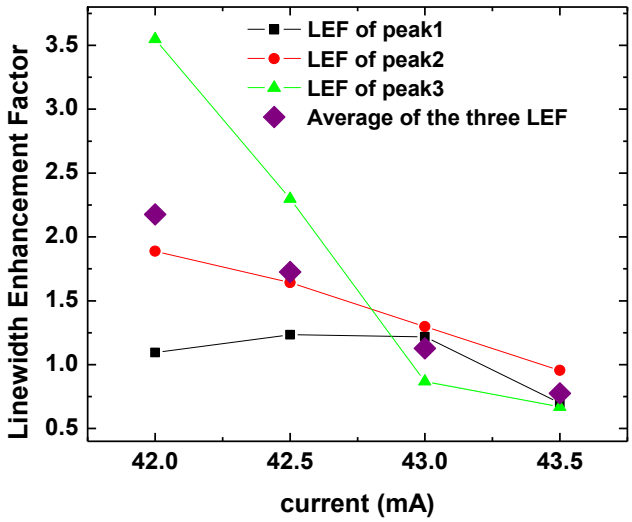

Fig. 3.5. LEF obtained for three peaks at the 1 nm range. Averaged LEF among the three peaks is also shown.

3.4 Conclusion

We have reported LEF measurement of InAs/InP QD lasers. The obtained LEF above threshold is 1.37 at the gain peak and maintains to be less than 2 in the main gain region from 1524 to 1535 nm. The LEF below threshold is found to decrease with increased current and to be less than 1 with current increasing to 43.5 mA by Hakki-Pauli method. To our best knowledge, they are the lowest values reported so far for InAs/InP QD lasers emitting around 1.5 μm. Our LEF is smaller than the other reported values on InAs/InP QDs [136, 137] and may be attributed to the nearly symmetric gain spectrum [84], less sensitive refractive index change with carrier density and larger differential gain in our QD lasers. Therefore, our InAs/InP QDs with small LEF are perfect gain materials for QD MWLs, QD MLLs and QD DFB lasers around 1.5 μm.

Chapter 4 Modeling of Single-Section InAs/InP QD MLLs

4.1 Introduction

In two-section QD MLLs, the low saturation energy and fast recovery time of the QD absorber leave a narrow net gain window for the pulse shaping and amplification [53, 83, 116]. In single-section QD MLLs, the SA section does not exist and thus there is no interplay for evolving pulses in gain and saturation absorber sections [55, 68, 69]. In both types of lasers, pulse durations from ps to hundreds of fs have been reported. As the pulses become shorter and shorter [72] [115], the GVD impact will be more and more significant and cannot be ignored. Some techniques mitigating the dispersion effect have already been developed to compress the pulse width. For example, by using a dual grating dispersion compensator, the pulse width is reduced from 14 ps to 970 fs [114]. With the help of a 1200-meter-long single mode compensation fiber, the pulse width of 770 fs has also been obtained [43]. These works indicate that the pulse evolution is strongly affected by the GVD in the laser cavity. On the other hand, due to the relative high peak power density in the laser cavity, the nonlinearity induced SPM is another important factor that affects the pulse evolution. Thus, it is essential to include the GVD and SPM in modeling to accurately model the pulse evolution in QD MLLs, especially when the pulses have width of hundreds of fs and the pulse peak power is high.

Travelling-wave (TW) model is a popular method to solve the electromagnetic wave propagation in optical fibers, semiconductor lasers and amplifiers. A TDTW model for QD MLLs, which was proposed by Rossetti [61] and introduced in section 2.4.2, has been successfully used in the simulations of two-section QD MLLs [61, 62, 109, 146]. This TDTW model, coupled with rate equations, can give an accurate description of the

spatiotemporal electric field and carrier dynamics in the cavity. And the QD carrier dynamics in all states and the QD optical susceptibility are fully accounted in this model. However, the GVD effect was not included in the model. Although two different group velocities for GS and ES were applied [62], the GVD effect was neglected within each state (one state includes multiple longitudinal modes). Here, we will establish a TDTW model that includes the GVD and SPM effect to accurately model the evolution of pulses generated from the QD MLLs. To our knowledge, it is the first time that the effects of both GVD and SPM are directly involved in the dynamic lasing process of QD MLLs. The nonlinearity in a laser system includes two aspects: 1) the nonlinearity from the material itself; and 2) the nonlinearity induced by the confined (interband/intraband) energy levels. In our improved model, the 1^{st} part is considered as the SPM term, and the 2^{nd} part, which is complex but especially important in the mode-locking, is treated as an equivalent SA. Careful and detailed discussions on the above nonlinearities will be presented.

For numerical techniques, we will adopt the first-order Taylor expansion and the central difference approximation to deal with the GVD term, and then the whole model is solved iteratively. To verify the accuracy of the first-order Taylor approximation, the second-order Taylor expansion is also applied for comparison. It is found that our presented model can be used to successfully simulate the pulse evolution of QD MLLs. The effects of GVD and SPM on the pulse evolution are discussed.

This chapter is organized as follows. The device structure in the simulation is simply introduced in section 4.2. Also in this section, the TDTW model is modified by taking into account the GVD and SPM, and then it is applied to a single-section QD MLL. We

approximate the GVD term by first-order Taylor series expansion and then the modified model can be solved directly by finite-difference method. In section 4.3, pulse evolution as a function of GVD is analyzed, with comparison to experimental results. The second-order Taylor expansion is further applied to the modified model and compared with the first-order expansion. The effects of GVD and SPM are also compared. The chirp and TBP value are then given. In section 4.4, nonlinear effects and the effect of the equivalent SA are discussed. In section 4.5, a conclusion is drawn.

4.2 Modified TDTW model including GVD and SPM

4.2.1 Device structure

The grown structure of the InAs/InP QD laser used in the simulation is shown in Fig. 4.1. Lattice matched InGaAsP cladding layer is grown on the substrate InP with width of 155 nm. The photoluminescence (PL) peak of this layer appears at 1.15 μm at 300 K (referred as 1.15Q layer). The InAs QDs are directly grown on the 1.15Q or a thin GaP layer to control the centre emission wavelength [142]. Multiple layers of QD are repeated with 9 nm InGaAsP spacer layers between each two layers.

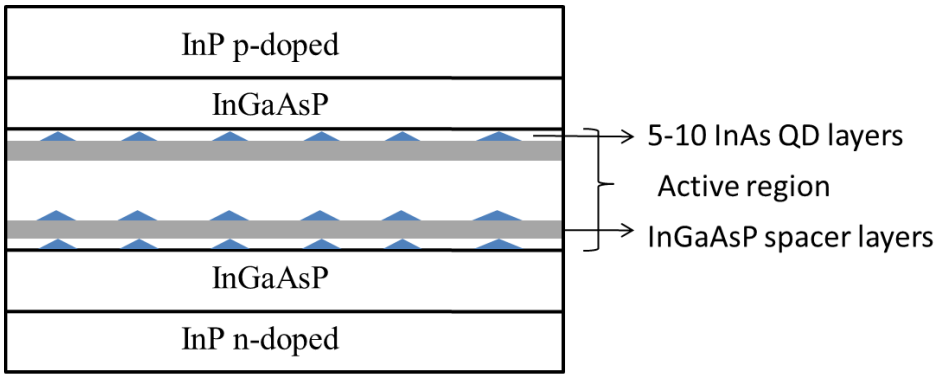

Fig. 4.1. Schematic diagram of the simulated InAs/InP QD laser. The triangles in the figure represent QDs.

The active region usually consists of 5 to 10 layers of QDs. And in the growth, the InAs dots are directly deposited on the InGaAsP barrier (dot-in-a-barrier structure) and only GS (no ES) is observed in the 300 K PL curve of our InAs/InP QD lasers. The energy diagram is simply plotted in Fig. 4.2.

The inhomogeneous gain bandwidth is about 60-70 nm (FWHM), corresponding to 31.4 and 36.6 meV in energy.

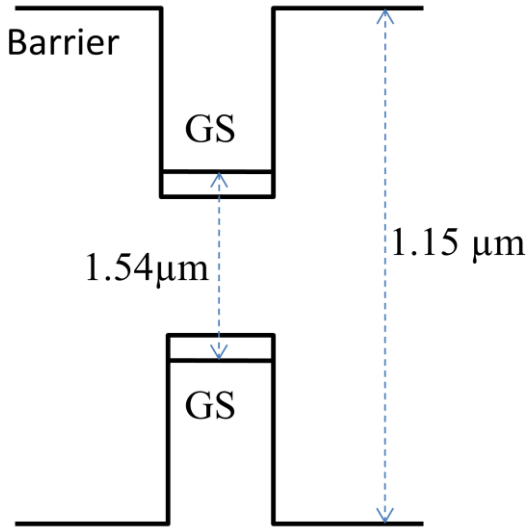

Fig. 4.2. Energy diagram of the InAs/InP QD laser used in the simulation. Only GS is observed in the PL peak. The emission centre is at about 1.54 μm.

4.2.2 GVD and SPM expression in the TDTW model

The propagation constant β can be expanded by Taylor series as

$$\beta(\omega)=n(\omega)\frac{\omega}{c}=\beta_0+\beta_1(\omega-\omega_0)+\frac{\beta_2}{2}(\omega-\omega_0)^2+\ldots, \qquad (4.1)$$

where $\beta_m=\left(\frac{d^m\beta}{d\omega^m}\right)_{\omega=\omega_0}$ $m=0,1,2\ldots$

The parameters β_1 and β_2 are referred as group velocity and GVD parameter. They are related to the refractive index n and its derivatives as

$$\beta_1 = \frac{1}{v_g} = \frac{n_g}{c} = \frac{1}{c}\left(n + \omega\frac{dn}{d\omega}\right) \tag{4.2}$$

$$\beta_2 = \frac{d\beta_1}{d\omega} = -\frac{\lambda^2}{2\pi c^2}\frac{dn_g}{d\lambda} = \frac{1}{c}\left(2\frac{dn}{d\omega} + \omega\frac{d^2n}{d\omega^2}\right) \tag{4.3}$$

where n_g is the group index, and v_g is the group velocity. The envelope of pulse moves at the speed of v_g during which the pulse is broadened because of GVD. The cubic and higher-order terms $\beta_m, m > 2$ in the Taylor expansion are usually negligible. When lower-order terms are close to zero, high-order terms need to be included, which can also lead to pulse distortion in the propagation. By the Fourier-transform, the term $\frac{\beta_2}{2}(\omega - \omega_0)^2$ is replaced by the second-order differential operator $-\frac{\beta_2}{2}\left(\partial^2 \big/ \partial t^2\right)$ in the time domain, which represents the GVD effect in the TDTW model.

The SPM is a nonlinear effect leading to the intensity dependence of the refractive index in the cavity. It can induce optical spectral broadening and frequency chirp. The intensity dependent nonlinear phase shift by SPM is $\phi_{NL} = n_2 k_0 L|E|^2$, where n_2 is the nonlinear refractive index, $k_0 = 2\pi/\lambda$, L is the interaction length and E is the electric field. The SPM effect in the TDTW equations are $\delta|E|^2 = \frac{n_2\omega_0}{cA_{eff}}|E|^2$, where A_{eff} is the effective area in m^2, $|E|^2$ is optical power, and δ is the Kerr-nonlinear coefficient.

The gain and refractive index both change with carrier densities and the two quantities are related via the LEF parameter. According to the expressions in Eq. (2.16), carrier dynamics lead to the dynamics of gain and refractive index in the cavity. The

nonlinear refractive index leads to therefore the variation of the carrier frequency with time along the pulse envelope, which is usually referred as carrier dynamics induced SPM. Carrier dynamics induced SPM is already included in the model but n_2 induced SPM needs to be additionally considered in the following.

4.2.3 Modified TDTW model

The details of TDTW model were given in section 2.4.2. The laser system can be described by forward and backward propagation equations, two boundary conditions, one rate equation for the WL and N rate equations for the GS. Note that for our considered lasers, WL and GS are only considered. And the equations are given as follows:

$$\text{WL:}\quad \frac{dN_W}{dt}=\eta_i\frac{J}{e}\Delta zW-\frac{N_W}{\tau_r^W}-\sum_{i=1}^{N}\frac{G_i}{\tau_c}N_W\left(1-f_i\right)+\sum_{i=1}^{N}\frac{N_{iGS}}{\tau_e^i}, \tag{4.4a}$$

$$\begin{aligned}\text{GS:}\quad \frac{dN_{iGS}}{dt}&=\frac{G_i}{\tau_c}N_W\left(1-f_i\right)-\frac{N_{iGS}}{\tau_e^i}-\frac{N_{iGS}}{\tau_s}\\&\quad-\frac{j\Delta z}{\hbar\omega_i}\left[\left(E^+p_i^{+*}-E^{+*}p_i^+\right)+\left(E^-p_i^{-*}-E^{-*}p_i^-\right)\right],\end{aligned} \tag{4.4b}$$

The definition of parameters can be found in section 2.4.2.

When the GVD and SPM effects are included, Eq. (2.9) is modified into

$$\pm\frac{\partial E^\pm}{\partial z}+\frac{1}{v_g}\frac{\partial E^\pm}{\partial t}-j\frac{\beta_2}{2}\frac{\partial^2E^\pm}{\partial t^2}=-\frac{\alpha_i}{2}E^\pm-j\delta\left|E\right|^2E^\pm-jP^\pm\left(z,t\right)+F^\pm\left(z,t\right), \tag{4.5}$$

where the SPM effect is included by $-j\delta\left|E\right|^2E$ and the GVD effect is included by $j\left(\beta_2/2\right)\left(\partial^2E/\partial t^2\right)$. $\delta=2\pi n_2/A_{\text{eff}}$ is the Kerr-coefficient, where n_2 is the nonlinear refractive index and A_{eff} is the effective cross-sectional area. β_2 is the dispersion coefficient of laser waveguide given by $\beta_2=-\left(\lambda^2/2\pi c^2\right)\left(dn_g/d\lambda\right)$ and $v_g=c/n_g$ is the

group velocity. To obtain the solution of Eq. (4.5), the effect of SPM can be included in the simulation by considering the phase change of $e^{-j\delta|E|^2 E\Delta z}$ in each time step. However, when the effect of GVD, represented by a second-order derivative in Eq. (4.3), is included, it is difficult to deduce Eq. (4.5) into an analytical expression as Eq. (2.22) by using the inverse Fourier transform. The following method is proposed to solve Eq. (4.5). Converting Eq. (4.5) into the frequency domain, we get

$$\begin{aligned}&\pm\frac{\partial E^{\pm}(z,\omega)}{\partial z}+j\omega\frac{1}{v_g}E^{\pm}(z,\omega)+j\omega^2\frac{\beta_2}{2}E^{\pm}(z,\omega)\\&=-\frac{\alpha_i}{2}E^{\pm}(z,\omega)-j\frac{\omega_0}{2cn_g}\tilde{\chi}(z,\omega)E^{\pm}(z,\omega)+F^{\pm}(z,\omega).\end{aligned}\tag{4.6}$$

A term containing ω^2 (the 3rd term) appears at the left side of the equation. Take the forward electric field as an example in deriving the following equations. The backward propagation field can be obtained in the same way. We rearrange the terms of Eq. (4.6),

$$\begin{aligned}\frac{\partial E^{+}(z,\omega)}{\partial z}&=-j\left(\omega\frac{1}{v_g}+\omega^2\frac{\beta_2}{2}\right)E^{+}(z,\omega)-\frac{\alpha_i}{2}E^{+}(z,\omega)\\&\quad-j\frac{\omega_0}{2cn_g}\tilde{\chi}(z,\omega)E^{+}(z,\omega)+F^{+}(z,\omega)\\&=-j\left(\omega\frac{1}{v_g}+\omega^2\frac{\beta_2}{2}\right)E^{+}(z,\omega)+\kappa(z,\omega)E^{+}(z,\omega)+F^{+}(z,\omega),\end{aligned}\tag{4.7}$$

where $\kappa(z,\omega)=-\alpha_i/2-j\left(\omega_0/2cn_g\right)\tilde{\chi}(z,\omega)$. Eq. (4.7) is a non-homogeneous equation. By taking a small step of Δz, the solution can be written as

$$\begin{aligned}E^{+}(z+\Delta z,\omega)&=E^{+}(z,\omega)e^{-\left(j\frac{\omega}{v_g}+j\omega^2\frac{\beta_2}{2}\right)\Delta z}e^{\kappa(z,\omega)\Delta z}+F^{+}(z,\omega)\Delta z\\&=E^{+}(z,\omega)e^{-j\frac{\omega}{v_g}\Delta z}e^{-j\omega^2\frac{\beta_2}{2}\Delta z}e^{\kappa(z,\omega)\Delta z}+F^{+}(z,\omega)\Delta z.\end{aligned}\tag{4.8}$$

The GVD operator was Fourier transformed to $e^{-j\omega^2\beta_2\Delta z/2}$ in the frequency domain. Due to existence of this term, we cannot get a time-domain expression analytically by directly using the inverse Fourier transform. This is the main difference between the models with and without the GVD effect. To get the solution, the Taylor expansion approximation is used in the following derivations.

4.2.4 Numerical methods

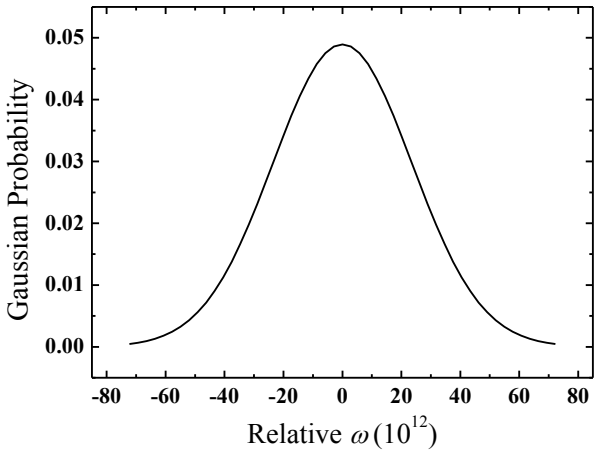

Fig. 4.3. The Gaussian distribution of QD growth/size probability. The y-axis shows relative values.

To ensure the accuracy of the approximation, several quantities should be estimated. For our considered QD MLL, the FWHM of the inhomogeneous gain broadening is ~60 nm (47.66 THz). And the Gaussian distribution of QDs is shown in Fig. 4.3, where the centre is assumed at around 1540 nm. At $\left|\Delta\omega_{\max}\right| = 72.25\times10^{12}$ Hz, the Gaussian distribution is close to zero, and beyond that the QD growth probability is almost zero. The value of β_2 is given by $\beta_2 = -\left(\lambda^2/2\pi c^2\right)\left(dn_g/d\lambda\right) = 2.139\times10^{-24}$ s^{2}m^{-1}, where $dn_g/d\lambda = -5.1\times10^5$ m^{-1} is taken from [134]. If the simulation time step is set $\Delta t = 10$ fs

and thus $\Delta z = v_g \Delta t = \left(c/n_g\right)\Delta t = 8.3904\times10^{-7}$ m, then the estimated maximum value of the GVD operator is $\left(e^{-j\omega^2\beta_2\Delta z/2}\right)_{\max} = e^{-j0.0047}$, which is a very small quantity. Therefore, the first-order Taylor expansion of $e^{-j\omega^2\beta_2\Delta z/2} \approx 1 - j\omega^2\beta_2\Delta z/2$ is used. Taking this approximation into Eq. (4.8), we can get

$$\begin{aligned} E^+\left(z+\Delta z,\omega\right) &= E^+\left(z,\omega\right)e^{-\left(j\frac{\omega}{v_g}+j\omega^2\frac{\beta_2}{2}\right)\Delta z}e^{\kappa(z,\omega)\Delta z} + F^+(z,\omega)\Delta z \\ &\approx E^+\left(z,\omega\right)e^{-j\frac{\omega}{v_g}\Delta z}\left(1-j\omega^2\frac{\beta_2}{2}\Delta z\right)e^{\kappa(z,\omega)\Delta z} + F^+(z,\omega)\Delta z \\ &= E^+\left(z,\omega\right)e^{-j\omega\Delta t}e^{\kappa(z,\omega)\Delta z} + F^+(z,\omega)\Delta z \\ &\quad - j\omega^2\frac{\beta_2}{2}\Delta z E^+\left(z,\omega\right)e^{-j\omega\Delta t}e^{\kappa(z,\omega)\Delta z}. \end{aligned} \tag{4.9}$$

The first two terms on the right side of Eq. (4.9) are the same as the ones in the TDTW model without GVD, which can be converted back to the time-domain directly. The third item requires further approximation. It can be written as

$$\begin{aligned} &-j\omega^2\frac{\beta_2}{2}\Delta z E^+\left(z,\omega\right)e^{-j\omega\Delta t}e^{\kappa(z,\omega)\Delta z} \\ &\approx -j\frac{\beta_2}{2}\Delta z\omega^2 e^{-j\omega\Delta t}E^+\left(z,\omega\right)\left(1-\frac{\alpha_i}{2}\Delta z - j\frac{\omega_0}{2cn_g}\tilde{\chi}\left(z,\omega\right)\Delta z\right) \end{aligned} \tag{4.10}$$

Eq. (4.10) can be transformed into the time-domain as

$$j\frac{\beta_2}{2}\Delta z\frac{\partial^2 E^+\left(z,t-\Delta t\right)}{\partial\left(t-\Delta t\right)^2}\left(1-\frac{\alpha_i}{2}\Delta z\right) - \frac{\beta_2}{2}\Delta z^2\frac{\partial^2 P^+\left(z,t-\Delta t\right)}{\partial\left(t-\Delta t\right)^2}$$

Using the above expression, Eq. (4.9) can be converted into the time-domain as

$$
\begin{aligned}
&E^{+}\left(z+\Delta z,t+\Delta t\right)\\
&\cong E^{+}\left(z,t\right)-jP^{+}\left(z,t\right)\Delta z+j\frac{\beta_2}{2}\Delta z\frac{\partial^2 E^{+}\left(z,t\right)}{\partial t^2}\left(1-\frac{\alpha_i}{2}\Delta z\right)\\
&-\frac{\beta_2}{2}\Delta z^2\frac{\partial^2 P^{+}\left(z,t\right)}{\partial t^2}+F^{+}\left(z,t\right)\Delta z-\frac{\alpha_i}{2}E^{+}\left(z,t\right)\Delta z\\
&\cong E^{+}\left(z,t\right)-jP^{+}\left(z,t\right)\Delta z+j\frac{\beta_2}{2}\Delta z\frac{\partial^2 E^{+}\left(z,t\right)}{\partial t^2}\left(1-\frac{\alpha_i}{2}\Delta z\right)\\
&+F^{+}\left(z,t\right)\Delta z-\frac{\alpha_i}{2}E^{+}\left(z,t\right)\Delta z\\
&\cong E^{+}\left(z,t\right)-jP^{+}\left(z,t\right)\Delta z+F^{+}\left(z,t\right)\Delta z-\frac{\alpha_i}{2}E^{+}\left(z,t\right)\Delta z\\
&+j\left(1-\frac{\alpha_i}{2}\Delta z\right)\frac{\beta_2}{2}\Delta z\frac{E^{+}\left(z,t+\Delta t\right)-2E^{+}\left(z,t\right)+E^{+}\left(z,t-\Delta t\right)}{\Delta t^2},
\end{aligned}
\tag{4.11}
$$

where the central difference approximation was adopted with $\partial^2 E/\partial t^2=\left[E^{+}\left(z,t+\Delta t\right)-2E^{+}\left(z,t\right)+E^{+}\left(z,t-\Delta t\right)\right]/\Delta t^2$. The item $\left(\beta_2/2\right)\Delta z^2\left(\partial^2 P\left(z,t\right)/\partial t^2\right)$ was omitted due to the small quantity of Δz^2. Eq. (4.11) is the final solution we derive for the modified TDTW model that includes GVD. The backward propagation optical field can be acquired in the same way, given by

$$
\begin{aligned}
&E^{-}\left(z-\Delta z,t+\Delta t\right)\\
&\cong E^{-}\left(z,t\right)-jP^{-}\left(z,t\right)\Delta z+F^{-}\left(z,t\right)\Delta z-\frac{\alpha_i}{2}E^{-}\left(z,t\right)\Delta z\\
&+j\left(1-\frac{\alpha_i}{2}\Delta z\right)\frac{\beta_2}{2}\Delta z\frac{E^{-}\left(z,t+\Delta t\right)-2E^{-}\left(z,t\right)+E^{-}\left(z,t-\Delta t\right)}{\Delta t^2}
\end{aligned}
\tag{4.12}
$$

For the model without GVD, $E^{\pm}\left(z\pm\Delta z,t+\Delta t\right)$ can be directly calculated from Eq. (2.22) with given $E^{\pm}\left(z,t\right)$. However, in Eqs. (4.11) and (4.12), $E^{\pm}\left(z,t+\Delta t\right)$ is also pre-required for calculating $E^{\pm}\left(z\pm\Delta z,t+\Delta t\right)$ in addition to $E^{\pm}\left(z,t\right)$. Thus, iterations are used to calculate $E^{\pm}\left(z,t+\Delta t\right)$at each time step. The steps for the iterations are

(1) At time t, we have all the values of $E^{\pm}(z,t), z = 0,1...\mathrm{L}$;

(2) At time $t+\Delta t$, the initial values are calculated without considering the GVD. That is to say, we can get the initial values $E^{\pm}(z,t+\Delta t)_{\mathrm{ini}}, z = 0,1...\mathrm{L}$ by Eqs. (2.22) and (2.12);

(3) Take the initial value $E^{\pm}(z,t+\Delta t)_{\mathrm{ini}}$ from step 2 into Eqs. (4.11) and (4.12). Sweeping z, then all the values of $E^{\pm}(z,t+\Delta t), z = 0,1...\mathrm{L}$ can be renewed, given by $E^{\pm}(z,t+\Delta t)_1, z = 0,1...\mathrm{L}$;

(4) Take $E^{\pm}(z,t+\Delta t)_1, z = 0,1...\mathrm{L}$ into Eqs. (4.11) and (4.12), then we can get $E^{\pm}(z,t+\Delta t)_2$;

(5) Compare $E^{\pm}(z,t+\Delta t)_1$ and $E^{\pm}(z,t+\Delta t)_2$ to check if converged or not; if not converged, take $E^{\pm}(z,t+\Delta t)_2$ into Eqs. (4.11) and (4.12) again, then we can get $E^{\pm}(z,t+\Delta t)_3$;

(6) Repeat the above steps until the solutions are converged.

4.3 Simulation results and discussions

4.3.1 Equivalent saturable absorber

The modified model is applied to a single-section InAs/InP QD MLL previously demonstrated by our group [68]. The ridge width is 2.5 μm, and the cavity length is 456 μm. The parameters used in the simulation are listed in Table 4.1. One facet of the waveguide is highly coated and the other is cleaved. The QD active core consists of five stacked layers of self-assembled InAs QDs in an InGaAsP matrix on a n-type InP substrate and covered by a p-type InP top layer. The QD growth probability is

approximately expressed by a Gaussian distribution as shown in Fig. 4.3. The gain center is at 1540 nm.

As stated in the prior publications [57, 58, 68], FWM and Kerr-lens effect are considered the possible mechanisms leading to mode-locking in single-section QD MLLs. To realize mode-locking, these two effects should also be considered in our model. Recently, the random population model was used to explain the mode-locking in single-section QD MLLs, where part of the QD medium is considered absorptive [77]. Since the mechanisms of both Kerr-lens mode-locking and the random population distribution induced mode-locking are equivalent to a SA, we simply take the expression of a SA in our modeling [3]:

$$s(t) = \frac{s_0}{1 + I(t)/I_{sat}}, \tag{4.13}$$

where s_0 is the unsaturated loss, $I(t)$ is the laser intensity and I_{sat} is the saturation intensity of the saturable absorber.

Table 4.1 Laser parameters used in the simulation

Parameters	values
Cavity length L (μm)	456
Ridge width W (μm)	2.5
Refractive index n	3.5755
Number of QD layers N	5
QD surface density N_D (m^{-2})	3×10^{14}
Number of QD groups	15
State degeneracy	2
Homogeneous linewidth (meV)	8
FWHM of the inhomogeneous broadening (meV)	36.6

Waveguide loss α (m^{-1})	1700
Energy separation between groups (meV)	5.7
Interband recombination time of the WL τ_r^W (ps)	500
Spontaneous emission time of GS τ_s (ns)	1.2
Capture time from WL to GS τ_c (ps)	2
QD height (nm)	1
Facet refractivity	99%, 33%
Simulation center wavelength (nm)	1540
WL energy (meV)	1.0789
GS center energy (meV)	0.8056

According to Eq. (4.13), this self-focusing effect can be included into the TDTW model as:

$$E^+(L,t) = \left(1 - \frac{s_0}{1 + \frac{\left|E^+(L,t)\right|^2}{I_{sat}}}\right) E^+(L,t), \tag{4.14}$$

where $E^+(L,t)$ is the amplitude of the forward electrical field at the facet.

The unsaturated loss s_0 is related to the nonlinear refractive index n_2, the confinement factor and the pulse peak intensity, etc. And I_{sat} is related to the dipole moment of the transitions, the carrier lifetime and the confinement factor, etc [147]. In the simulation, s_0 and I_{sat} are fitting parameters. If s_0 is fixed at 0.35, stable mode-locked pulses can be obtained for I_{sat} from 0.01 to about 0.14 W, and the pulse width decreases from about 230 to 190 fs (with GVD and SPM considered which will be discussed in the following section). Further change of (increase or decrease) I_{sat} results in unstable locking or unlocked state. If I_{sat} is fixed at 0.08 W, stable mode-locked pulses can be obtained for s_0 from 0.34 to 0.375. The pulse width is 197 fs at s_0=0.34 and at 185 fs at s_0=0.375.

Unstable mode-locking is observed for s_0 decreased to be less than 0.34, and unlocked state is observed for s_0 below 0.32. No lasing occurs for s_0 larger than 0.375. In addition, the pulse width is found to increase with the decrease of s_0. The s_0 and I_{sat} values within the range of leading to mode-locked state do not affect the prediction of the pulse evolution. Therefore s_0=0.35 and I_{sat}=0.08 W are used in the simulation.

4.3.2 GVD and SPM effects on the pulse evolution

In the following, we will concentrate on the GVD and SPM effects on the pulse evolution. The simulated time-domain pulse trains for the cases with and without the GVD and SPM effects are shown in Fig. 4.4. Pulse trains with repetition rate of 92 GHz are successfully simulated at current density of $\mathrm{J} = 850\ \mathrm{A/cm^2}$ in the two cases as shown in Fig. 4.4. Without the GVD ($\beta_2 = 0$) and SPM effects, the pulse width is ~104.8 fs as plotted in black. With the GVD ($\beta_2 = 2.139\times10^{-24}\ \mathrm{s^2/m}$) and SPM effects included, ~192.1 fs pulse width is obtained as shown in red. For the SPM effect, the Kerr coefficient $\delta = 14.8018\ \mathrm{W^{-1}m^{-1}}$ was used by taking $n_2 = 7.8\times10^{-18}\ \mathrm{m^2/W}$ and $A_{eff} = 2.15\times10^{-12}\ \mathrm{m^2}$ [148]. It is seen that the pulses are broadened by the GVD and SPM effects. The optical spectra are shown in Fig. 4.5. It is obvious that the optical spectrum is narrowed with the two effects included. The 3-dB bandwidths are ~30.5 and ~20.3 nm, respectively.

To further demonstrate the effect of dispersion, pulse widths at various values of β_2 are evaluated. The intensities and widths of the pulses for different β_2 are shown in Fig. 4.6. It is seen that pulse peak decreases and pulse width broadens with the increase of β_2. And the FWHM of pulses are compared in Fig. 4.6 (b).

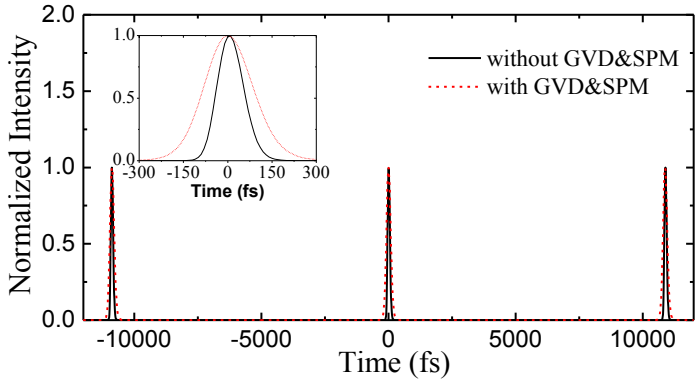

Fig. 4.4. Mode-locking pulse trains with and without GVD and SPM effects.

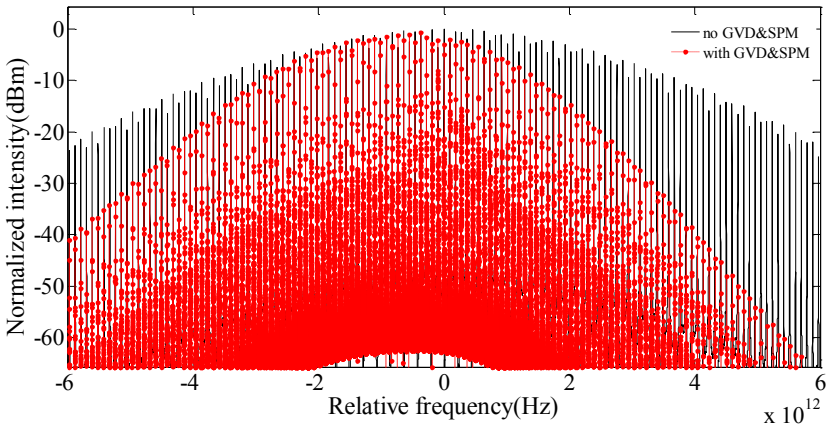

Fig. 4.5. Optical spectra without and with GVD and SPM effects. The center is at 1540 nm.

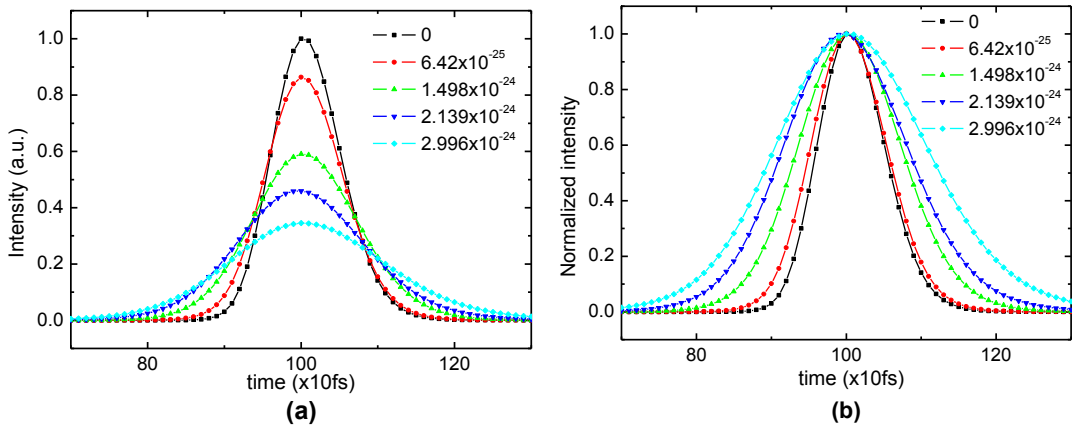

Fig. 4.6. Pulse shape at different β_2 values indicated in the figures. (a) Intensity normalized to the value of pulse peak at β_2=0. (b) All pulse peaks are normalized to 1.

4.3.3 Second-order Taylor expansion

To verify the accuracy of the first-order expansion, we extend the Taylor series to second-order. The second-order expansion of the exponential term in the frequency domain is

$$e^{-j\omega^2\frac{\beta_2}{2}\Delta z} \approx 1 - j\omega^2\frac{\beta_2}{2}\Delta z - \frac{1}{2}\left(\frac{\beta_2}{2}\Delta z\right)^2\omega^4.$$

Then Eq. (4.9) becomes

$$\begin{aligned}
&E^+\left(z+\Delta z,\omega\right) = E^+\left(z,\omega\right)e^{-\left(j\frac{\omega}{v_g}+j\omega^2\frac{\beta_2}{2}\right)\Delta z}e^{\kappa(z,\omega)\Delta z} + F^+(z,\omega)\Delta z \\
&\approx E^+\left(z,\omega\right)e^{-j\frac{\omega}{v_g}\Delta z}\left(1 - j\omega^2\frac{\beta_2}{2}\Delta z - \frac{1}{2}\left(\frac{\beta_2}{2}\Delta z\right)^2\omega^4\right)e^{\kappa(z,\omega)\Delta z} + F^+(z,\omega)\Delta z \\
&= E^+\left(z,\omega\right)e^{-j\omega\Delta t}e^{\kappa(z,\omega)\Delta z} + F^+(z,\omega)\Delta z - j\omega^2\frac{\beta_2}{2}\Delta z E^+\left(z,\omega\right)e^{-j\omega\Delta t}e^{\kappa(z,\omega)\Delta z} \\
&\quad -\frac{1}{2}\left(\frac{\beta_2}{2}\Delta z\right)^2\omega^4 E^+\left(z,\omega\right)e^{-j\omega\Delta t}e^{\kappa(z,\omega)\Delta z}.
\end{aligned} \tag{4.15}$$

By converting Eq. (4.15) into the time-domain, the third term of Eq. (4.9) is changed to

$$\begin{aligned}
&\left(1-\frac{\alpha_i}{2}\Delta z\right)\left(j\frac{\beta_2}{2}\Delta z\frac{\partial^2 E^+\left(z,t\right)}{\partial t^2} - \frac{1}{2}\left(\frac{\beta_2}{2}\Delta z\right)^2\frac{\partial^4 E^+\left(z,t\right)}{\partial t^4}\right) \\
&\approx\left(1-\frac{\alpha_i}{2}\Delta z\right)\left[j\frac{\beta_2}{2}\Delta z\frac{E^+\left(z,t+\Delta t\right)-2E^+\left(z,t\right)+E^+\left(z,t-\Delta t\right)}{\Delta t^2}\right. \\
&\left.-\frac{1}{2}\left(\frac{\beta_2}{2}\Delta z\right)^2\frac{E^+\left(z,t+\Delta t\right)-4E^+\left(z,t\right)+6E^+\left(z,t-\Delta t\right)-4E^+\left(z,t-2\Delta t\right)+E^+\left(z,t-3\Delta t\right)}{\Delta t^4}\right]
\end{aligned} \tag{4.16}$$

where $\dfrac{\partial^4 E}{\partial t^4} = \dfrac{E^+\left(z,t+\Delta t\right)-4E^+\left(z,t\right)+6E^+\left(z,t-\Delta t\right)-4E^+\left(z,t-2\Delta t\right)+E^+\left(z,t-3\Delta t\right)}{\Delta t^4}$

is applied.

With the second-order approximation, the pulse widths for various β_2 are also simulated for comparison with the previous results. The first-order solution becomes unstable when β_2 is increased to a certain value. But by applying the second-order Taylor

expansion, we are able to get stable results at large β_2 values. The simulated pulse widths in the two approximations are shown in Fig. 4.7. They are matched very well. The 3-dB bandwidth of the optical spectra as a function of β_2 is also shown in Fig. 4.7. The bandwidth becomes narrower with the increase of dispersion in the cavity.

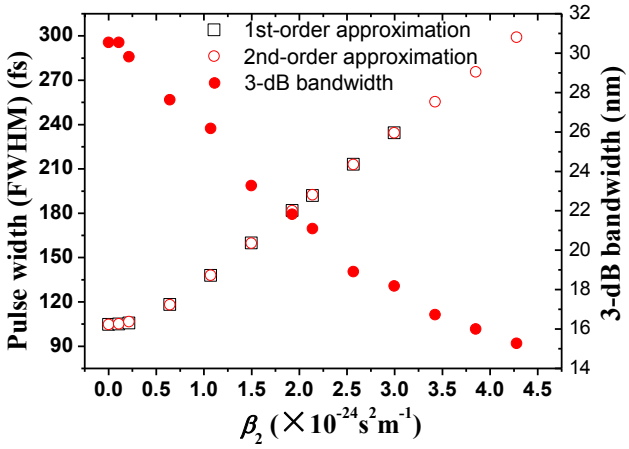

Fig. 4.7. Comparison of pulse width at different β_2 values using 1st- and 2nd-order approximations (left axis) and the 3-dB optical bandwidth as a function of β_2 values (right axis).

We have recently found that the dispersion of group index $dn_g/d\lambda$ may be up to $-8\times10^5/m$ in our QD lasers, corresponding to β_2 of 3.4224×10^{-24} s^2/m. If taking the value of β_2=3.4224×10^{-24} s^2/m, the pulses are broadened to 256 fs, and the 3-dB bandwidth is narrowed to 16.7 nm. In comparison, experimentally [68] for this laser they are 312-fs pulse width and 11.6-nm 3-dB bandwidth. Therefore, the simulation results are in reasonable agreement with the experimental data. The broader pulses from the experiments are mainly due to the following reasons: we used about 1 m standard single-mode fiber pigtail and EDFA at the output of the QD laser and before the optical auto-correlator, both of which definitely broaden the pulses, particularly for pulses with hundreds of fs width.

4.3.4 Contributions of GVD and SPM

In the following, we will analyze the contributions of the GVD and SPM effects in the laser cavity. When both the two effects are included, either GVD or SPM may be dominant, depending on the initial pulse width T_0 and peak power P_0. Two length scales are employed [149], the dispersion length L_D and the nonlinear length L_{NL}. They can measure dispersion and nonlinear effects on pulse evolution. They are given by $L_D = T_0^2 / |\beta_2|$, and $L_{NL} = 1/(\gamma P_0)$. In our case, T_0 (pulse width) equals to ~105 fs for the case of without GVD and SPM and $P_0 = 0.1\,\mathrm{W}$, then $L_D = 0.0052\,\mathrm{m}$ and $L_{NL} = 0.6756\,\mathrm{m}$. The ratio $N^2 = L_D / L_{NL} = 0.0077 \ll 1$. N^2 governs the importance of the SPM effect over GVD effect on the pulse evolution. If $N^2 \ll 1$, the GVD dominates; if $N^2 \gg 1$, the SPM effect dominates; and if $N \sim 1$, they are of equal importance [149]. In our case, $N^2 \ll 1$, the GVD is the dominant effect on pulse evolution and broadening. We have simulated pulse evolution including GVD but no SPM. It is found that the pulse width is slightly decreased from 192.109 fs to 191.706 fs when β_2 equals to $2.139 \times 10^{-24}\ \mathrm{s^2 m^{-1}}$, indicating the dominant effect of GVD in the QD cavity.

4.3.5 Chirp in the pulses

As indicated before, chirp in the pulses can be described by the parameter TBP. The TBP is defined as the product of pulse width (FWHM) and 3 dB bandwidth of the optical spectrum. From Fig. 4.7, we can calculate TBP as a function of β_2 and the results are plotted in Fig. 4.8.

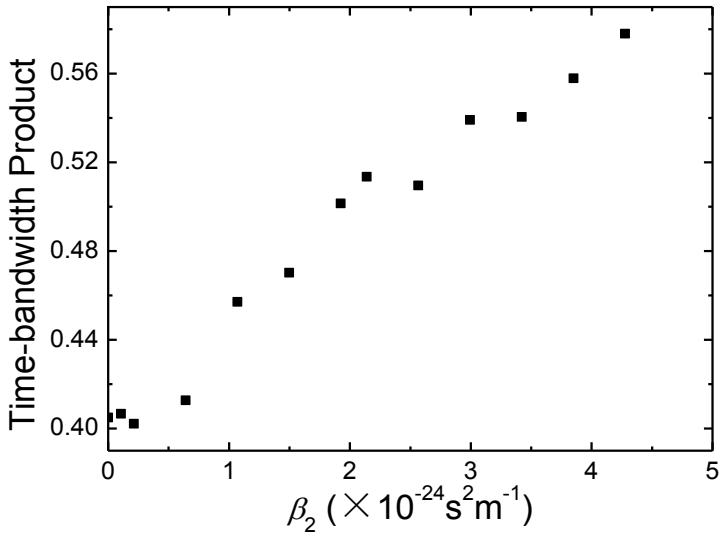

Fig. 4.8. Calculated TBP as a function GVD parameter β_2.

As shown in Fig. 4.8, the TBP increases from about 0.4 to 0.58 with the rise of β_2. The TBP value is about 0.44 for unchirped Gaussian-shaped pulses and 0.315 for unchirped sech^2-shaped pulses. It is seen in Fig. 4.8 that when β_2=0, the TBP is larger than 0.4. This means the output pulses are not completely Gaussian and also chirped. Thus the pulses are not transform-limited. According to our measurements, the measured TBP is about 0.457, which is within the range of our simulated results as shown in Fig. 4.8.

The chirp is determined by many factors, such as the GVD, SPM, the behaviour of the SA, and the interplay between the gain and absorber sections [116], etc. Considering the SA for example in [116], the TBP decreases with the increased reverse bias on the absorber. The explanation given in [116] is that the gain window is reduced as the increase of the reverse bias, while the spectral width is relatively independent of the reverse bias. Another important factor in QD lasers should be mentioned is the SPM induced by the dynamics of ES population [103]. The dynamics of ES population

significantly influences the refractive index at the lasing wavelength, leading to a non-zero chirp [61].

For the single-section QD (QD and QDash) MLLs, the pulse duration and the chirp are relatively low [52, 69, 70, 150]. This is possibly due to the specific locking mechanism of single-section QD MLLs. In our QD MLL, there is only the GS, and therefore no chirp induced by the dynamics of ES population. This could be one of the reasons that our QD MLL shows low chirp.

Even for the original TW-QD model without GVD and SPM, the pulses also exhibit chirps (Fig. 7 in [61]). The simulated pulse duration is 11.6 ps at 6V and 8 ps at 10 V. This is because the effects of the carrier dynamics in the gain and absorber are included in the rate equations.

As stated above, the pulse chirp is a combined effect of the above mentioned factors. Actually, not only the chirp, other characteristics of mode-locked pulses, such as pulse shape, pulse width, and power are all related to these factors. Therefore, to predict the behaviour of the pulses, besides the GVD and SPM, all the related factors should be included in the TW model. Especially, when the pulse power is high, carrier heating (CH) caused by two-photon absorption (TPA) and free carrier absorption (FCA) should also be considered which will be discussed in the following.

4.4 Discussions

4.4.1 Physical mechanisms for mode-locking in single-section QD MLLs

Currently, Kerr-lens and FWM effects are reported to be the possible mechanisms leading to the mode-locking in single-section QD MLLs, both of which are related to the third-order susceptibility $\chi^{(3)}$ and nonlinear refractive index n_2. $\chi^{(3)}$ is responsible for

nonlinear phenomena as SPM, XPM, FWM, and Kerr-lens, etc. The nonlinear index n_2 is related to $\chi^{(3)}$ as [149]

$$n_2 = \frac{3}{8n}\mathrm{Re}\left(\chi^{(3)}_{xxxx}\right), \tag{4.17}$$

where $\chi^{(3)}_{xxxx}$ is one component of $\chi^{(3)}$ by assuming linearly polarized optical field.

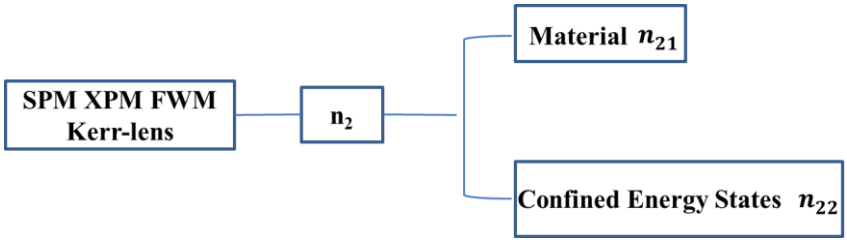

Fig. 4.9. Illustration of the cause of the nonlinear index coefficient (Kerr coefficient) n_2. The nonlinearity n_2 has two parts: n_{21} from the semiconductor material and n_{22} from the subbands.

Two factors contribute to $\chi^{(3)}$: the material itself and the confined energy states (intraband and interband) as illustrated in 错误!未找到引用源。. It is believed that the first nonlinearity is counted in the current TDTW model for calculating $-j\delta|E|^2 E$. However, the second nonlinearity could be more important in the mode-locking, although it is complicated and has not been well investigated yet.

Enhanced optical nonlinearities are found in QDs [151]. The FWM conversion efficiency and conversion symmetry is also greatly improved in QDs compared to those in bulk SOAs [92]. The wavelength conversion is compared in QD and QW optical amplifiers, where more efficient FWM is found in the QD device [152]. The increased $\chi^{(3)}$ is one of the factors leading to enhanced Kerr-lens and FWM effect in QDs [153]. With large nonlinearity in QDs, the two effects could have large influence on the laser

output. But until now, nearly no effort has been made to clarify the role of the two effects in leading to mode-locking in single-section QD lasers.

As circumstantial evidences, large nonlinearity is also reported in mode-locked quantum cascade lasers (QCLs) without SAs. The intersubband high nonlinearity has been confirmed in such lasers. Both Kerr-lens and FWM have been presented to be the possible mechanism leading to mode-locking. The Kerr-induced mode-locking was discussed in a mid-infrared QCL [147]. Ps pulses with repetition frequency of about 13 GHz were generated based on intersubband transitions. The transitions have characteristics of huge optical nonlinearities and fast carrier relaxation. The locking is attributed to Kerr-lens effect, where the intensity-dependent refractive index leads to a decrease of the optical losses with increased optical intensity. The emission spectrum is very broad and up to 1.5 THz for a range of biased current. The shape of the optical spectrum, the nonlinear index, the thickness of the dielectric blocking layers, and the far-field beam profiles were analyzed in the work as evidences of self-mode-locking by Kerr-lensing. In particular, the calculated nonlinear index n_2 is about 10^{-9} cm^2/W which is significantly greater than that in bulk material. For the FWM-induced mode-locking, the mechanism was identified as FWM between longitudinal modes, where large optical nonlinearities and low flat GVD are the key properties in the device [154]. The frequency comb covers 308 nm range in the spectrum with centre at 7 μm. The strong third-order susceptibility $\chi^{(3)}$ between the ES and the empty lower states allows the occurrence of FWM process. In addition, high FWM conversion efficiency of above -40 dB for over 3 THz detuning range was observed [155] in a QCL. The observations in these experiments

indicate that Kerr-lens and FWM could be responsible for the locking, although there is still lack of rigorous proofs.

To include the above possible locking mechanisms induced by the large nonlinearity (n_{22}) from the confined energy levels, an equivalent SA is applied in our simulation, and the parameters of which are fitted based on experimental results.

In the following sections, the effect of the equivalent SA and nonlinear effects based on the material n_{21} will be discussed. It is found that the contribution of the equivalent SA to the mode-locking is probably more than 90%. More efforts are required in the future for full consideration of the nonlinearity in the model.

4.4.2 SPM, XPM and FWM caused by the Kerr coefficient n_{21}

In this part, laser outputs only with the effect of n_{21}, i.e. without the SA, are simulated and presented. Before reaching the locking state, the nonlinear coefficient δ ($\delta = n_2\omega_0/cA_{eff}$) induced nonlinearity $-j\delta|E|^2 E$ in Eq. (4.5) actually has three parts: SPM, XPM and FWM. Taking two electric fields as an example, the nonlinear coupling is:

$$\begin{aligned} -j\delta|E|^2 E &= -j\delta(E_1+E_2)(E_1+E_2)^*(E_1+E_2) \\ &= -j\delta(E_1+E_2)(E_1^*+E_2^*)(E_1+E_2) \\ &= -j\delta\left(|E_1|^2 E_1 + |E_2|^2 E_2 + 2|E_1|^2 E_2 + 2|E_2|^2 E_1 + E_1^2 E_2^* + E_2^2 E_1^*\right) \end{aligned} \tag{4.18}$$

where the 1st two terms are SPM, the next two are XPM and the last two are FWM induced coupling, respectively. The FWM terms have generated new frequencies at $2\omega_1-\omega_2$ and $2\omega_2-\omega_1$. The effect of the nonlinear wave mixing on the output field is also included by the coefficient. The time-domain waveform shows no locking pulse train

in Fig. 4.10. With increased current in Fig. 4.11, the output intensity is higher; the extinction ratio of the self-pulsed waveform increases slightly; the spectrum is marginally expanded; but no mode-locked pulse train is formed. The nonlinear effects caused by n_{21} can hardly lead to mode-locking in single section QD MLLs.

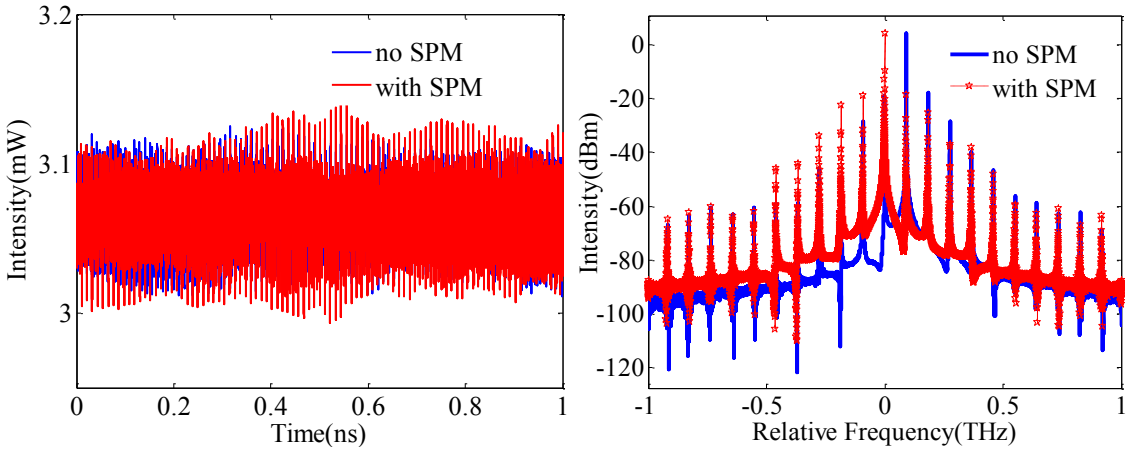

Fig. 4.10. The nonlinear coupling on the change of optical output in the time and frequency domains at the current density of 850 A/cm^2.

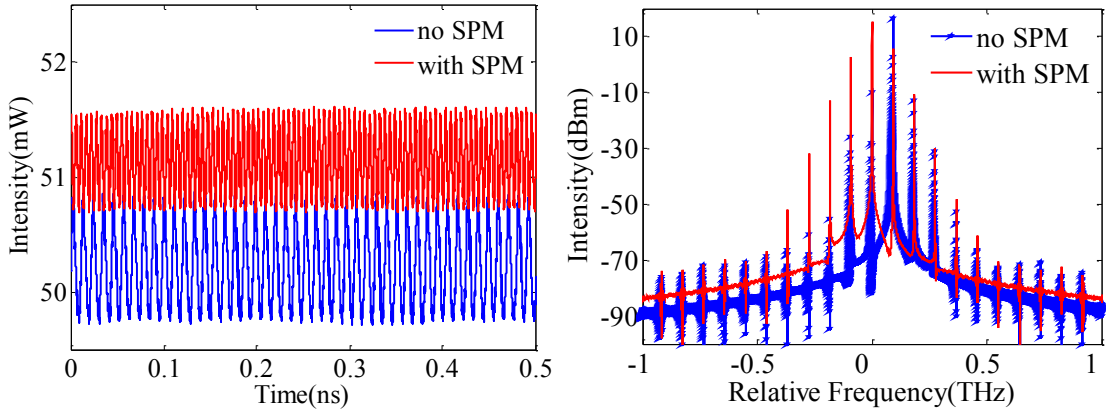

Fig. 4.11. The nonlinear coupling on the change of optical output in the time and frequency domains at the current density of 17000 A/cm^2.

4.4.3 Effect of the equivalent saturable absorber

In the simulation, the equivalent SA is responsible for the n_{22}. To study the importance of the equivalent SA, the laser outputs with and without the equivalent SA are compared.

The parameters used are the same as in section 4.2 except $s_0 = 0$. The time-domain waveform as a function of simulation time and the corresponding optical spectrum is plotted in Fig. 4.12. The whole time-domain output is also shown in the inset. It is seen that without the equivalent SA, the output time-domain waveform is almost cw and the corresponding optical spectrum is also very narrow where the centre mode is about 20 dB higher than the neighbour side modes. The cw output is mainly due to the central longitudinal modes. With the equivalent SA, the laser emits a train of mode-locked pulses at steady state and the corresponding occupation probability as a function of time is shown in Fig. 4.13. When the leading edge of the pulse enters the QD cavity, the QD occupation of the GS decreases and then it recovers with the trailing edge of the pulse leaving the cavity. In the figure, the change of the occupation probabilities for all QD groups are synchronized and repeated at the period of pulse circulation time in the cavity. There are totally 15 groups in the simulation, where group 8 corresponds to the emission centre. The QD groups closer to the emission centre have more intense stimulated emission. For a clear view, the occupation probability of QDs in eight groups is plotted in Fig. 4.13. For group 7, the probability is decreased from almost 100% to about 80% while the change is only 2% for group 1. The tendency of occupation probability as a function of time is the same as in two-section QD MLLs [156].

Without the equivalent SA, the probability is totally different where almost constant value versus time is observed in Fig. 4.14. As seen from the spectrum in Fig. 4.12, stimulated emission occurs mainly in the centre modes, corresponding to occupation variation of the group 8 in the inset of Fig. 4.14. There are also slight variations for the occupation in groups 7 and 9 but they change in an opposite way. By taking group 8 as

the symmetrical centre, the probability at its two sides show opposite tendency versus time whereas all groups exhibit the same tendency in a MLL as simulated with the equivalent SA.

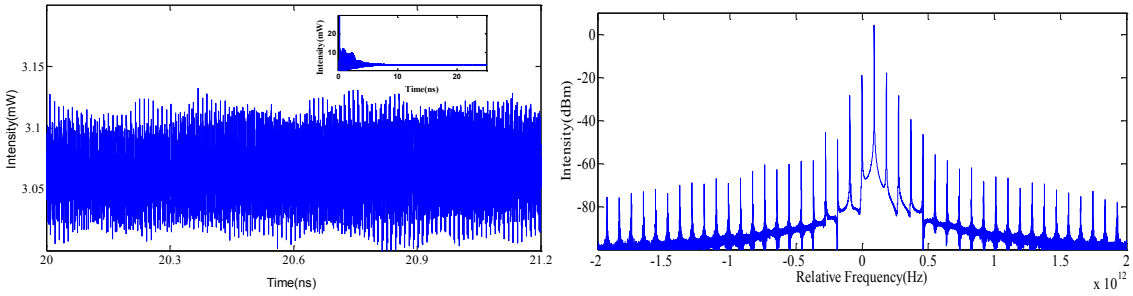

Fig. 4.12. (a). Time-domain waveform without the equivalent SA in the simulation at the current density of 850 A/cm^2. It is the zoom-in of the inset. The inset shows the waveform from 0 to 25 ns, where the output is not stable until about 8 ns. (b). Optical spectrum without the equivalent SA in the simulation. The frequency centre is at 1540 nm.

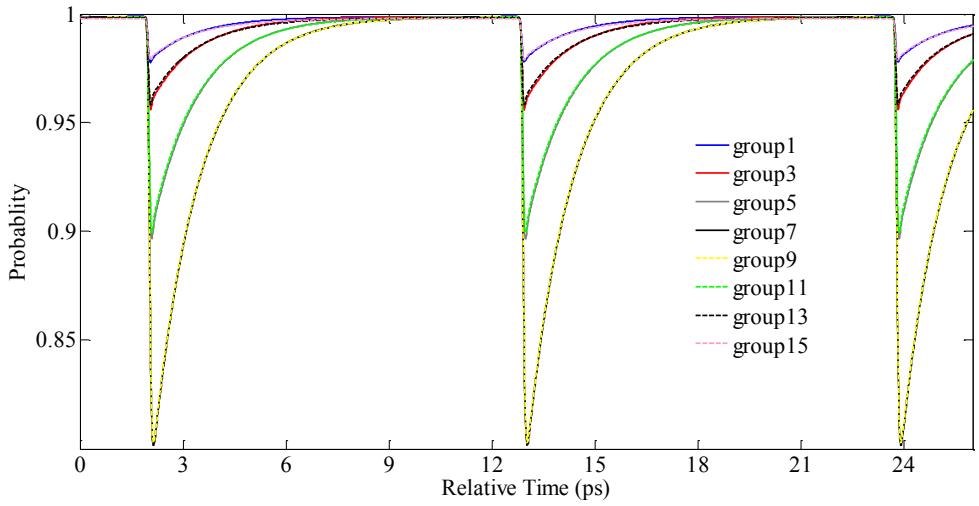

Fig. 4.13. Occupation probability versus time for 8 groups of QDs with the equivalent SA at the current density of 850 A/cm^2.

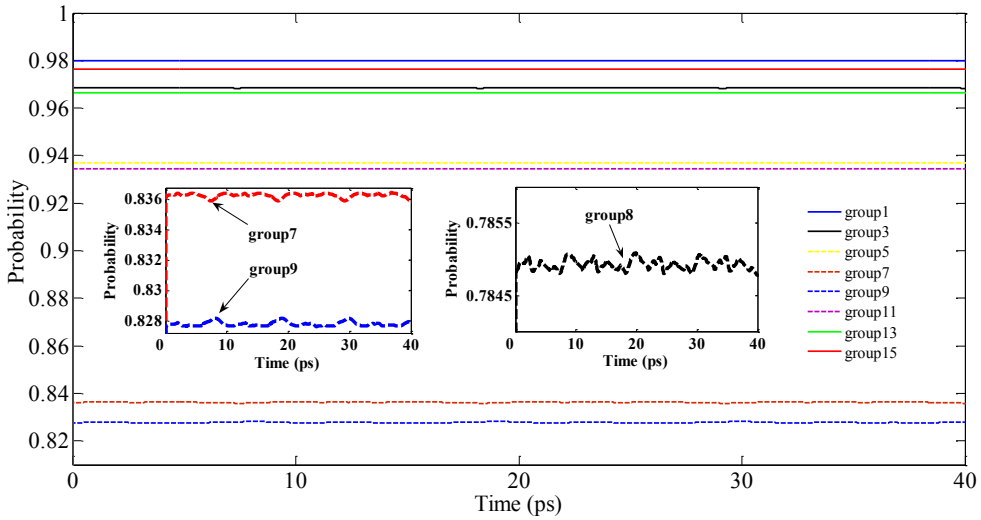

Fig. 4.14. Occupation probability versus time for 8 different groups of QDs without the equivalent SA at the current density of 850 A/cm^2. The insets show the enlarged plots for groups 7, 8, and 9.

Many parameters are also varied to check the outputs without the SA, which include the injection current, homogeneous gain bandwidth, number of QD groups, frequency separation of QD groups and gain parameters, etc. However, no clear mode-locked pulse train is observed in the simulation. Only self-pulsation is observed in the time domain by optimizing the parameters. For example, at the current density of 17000 A/cm^2, the time-domain self-pulsation is shown in Fig. 4.15. The contrast ratio given by the peak to bottom intensity of the pulse is about 6.89%. The self-pulsation is the result of beating between longitudinal modes in the frequency domain, indicating some phase correlation between the modes. The beating rate is the same as the ML frequency of 92 GHz. The beating might be caused by the CDP between longitudinal modes and the phase is partially correlated by the FWM.

The occupation probability of the eight QD groups is shown in Fig. 4.16. The stimulated emission occurs mainly in the centre QD groups, where periodic variation

over simulation time is observed and enlarged in the inset. In the inset of Fig. 4.16, the occupation probability for groups 7, 8 and 9 have similar variation tendency versus time. This is different from the previous case in Fig. 4.14, indicating some correlation among the groups involved in the stimulated emission probably as a result of self-pulsation.

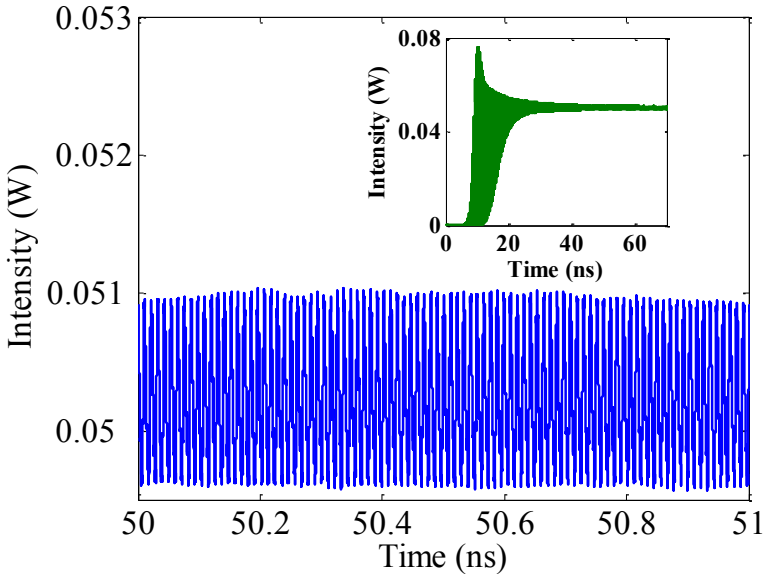

Fig. 4.15. Time-domain waveform without the equivalent SA in the simulation at the current density of 17000 A/cm^2. It is the zoom-in of the inset. The inset shows the waveform from 0 to 70 ns, where the waveform is not stable until about 30 ns.

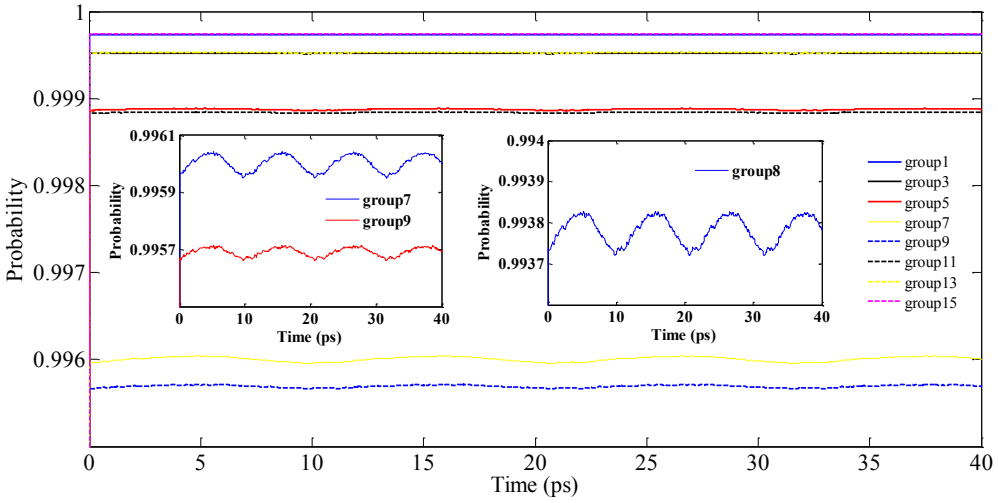

Fig. 4.16. Occupation probability versus time without the equivalent SA at the current density of 17000 A/cm^2. The inset shows the enlarged plot for groups 7, 8 and 9.

Without the equivalent SA, pulse train is not observed in the time-domain. Only self-pulsation occurs by adjusting some simulation parameters. The occupation probability also shows different tendency in all QD groups with and without the equivalent SA.

4.4.4 Other effects

Three effects might be important in our QD lasers: carrier density pulsation (CDP), spectral hole burning (SHB) and CH. The last term in Eq. (4.4b) representing the stimulated emission and the CDP is inherently included by this term [157, 158]. The SHB is also inherently included in the multi-level rate equations where more than one state is considered [159]. CH has three parts: FCA, TPA and stimulated transitions. The first two effects can create high energetic carriers in both the conduction and valence bands. And the hot carriers can heat up the distribution through carrier-carrier scattering. Stimulated emission can remove below-the-average-energy carriers (cool carriers), and thus leave above-the-average-energy carriers (hot carriers). Stimulated absorption does the same thing by creating hot carriers. The probability of stimulated transitions is higher than the FCA but the energy changed by each FCA event is orders of magnitude larger than the stimulated transitions [160]. The FCA caused heating often dominates in bulk and QWs. While in QDs, FCA is suppressed probably due to lower carrier density inversion required in the GS for lasing. In QDs, no significant CH is found and CH plays a minor role in the gain recovery of QD devices. As for TPA, it is considered important in gain compression especially at high peak powers. It is one of the major factors that cause CH no matter in bulk, QW or QD materials. The hot carriers induced by TPA affect the carrier distribution and then influence the gain, leading to the spectral distortions. For a comprehensive model suitable for broader range, the TPA should be included,

particularly when the pulse width reduces to several hundreds of fs. In the current form of our simulation, the TPA effect is not included, which is mainly due to the relative weak power in the simulated QD lasers.

To evaluate the TPA effect in our QD lasers, let's recall several quantities of the pulses in the references. (1) in Fig. 8 of [161], the TPA effect is significant for the pulse of 3.5 pJ and 450 fs (peak power of ~7.78 W); (2) in Fig. 2 of [162], the relation between TPA and pulse energy is shown. The net CH occurs at pulse of ~0.2-0.3 pJ and 170 fs (peak power of ~1.18 W); (3) in Figs. 2 and 5 of [87] (QD), the TPA affects the gain strongly when the pulse energy is greater than 0.27 pJ (pulse width of 150 fs, peak power of 1.8 W). And at 0.27 pJ, the TPA effect is still a small contribution of -0.5 dB. Therefore, the TPA effect is important for strong pulses only [87, 161, 162].

In our QD lasers, the energy of the pulse is ~0.09 pJ and the peak power is ~0.3 W [68], which are relatively lower than the above values. Even taking the facet reflection (30%) into consideration, the peak power in the laser cavity is ~0.43 W, which is still low. Thus, the TPA contribution to the pulse shape is considered small (<-0.5 dB). This could also be the reason that we didn't observe perceptible distortion in the measured spectrum [68].

4.5 Conclusion

We have successfully established an improved TDTW model that includes both GVD and SPM effects on the pulse generation and evolution in a single-section InAs/InP QD MLL. The solution of the improved model is solved by applying the 1st-order Taylor approximation on the GVD term. The 2nd-order approximation is also applied to verify the accuracy of the 1st-order approximation. The GVD and SPM effects on the pulse

evolution are investigated based on the improved TDTW model. The calculated pulse is in reasonable agreement with our previous experimental results. The contributions to the pulse broadening from GVD and SPM are discussed, and it is found that the GVD is the dominant broadening factor in our considered QD MLL.

Kerr-lens effect, FWM, and the random population are used to explain the mechanisms of mode-locking in single-section QD MLLs. According to these mechanisms, an equivalent SA is used in this paper. In the future, we will focus on these mechanisms and figure out their physical essence in mode-locking. Then their effects on the pulses can be further investigated. Moreover, the nonlinear effects such as TPA and FCA will also be included in our model at the presence of high-power pulses.

At last, it is worth noting that the proposed method of inclusion of GVD and SPM in the TDTW model is relatively independent to the other effects mentioned above. Also, this method is compatible with other effects and can be easily integrated in the general equations of the TW model. Therefore, this method should be useful in a broad range. With this method, as long as the lasers and amplifiers can be described by the TDTW model, the GVD and SPM effects on pulses can be successfully predicted.

Chapter 5 Ultra-High Repetition Rate Pulse Generation using External-Cavity Coupled InAs/InP QD MLLs

5.1 Introduction

Generation of optical pulse trains with a high repetition rate is desirable for the applications of high bit rate optical transmissions and high-speed digital information processing. High repetition-rate optical pulses can be generated in many methods [163-166] and the use of semiconductor MLLs is considered promising because of their compact size, electrical pumping, high efficiency, and easy operation. In particular, the use of QD semiconductor MLLs has attracted much more attention recently [24, 29, 58, 68], thanks to their inherent properties, such as fast carrier dynamics and broadband gain. Because the repetition rate of the pulse train is inversely proportional to QD waveguide length, the repetition rate of generated pulses is usually limited to be less than 100 GHz. Using high gain QDashes, an MLL emitting a pulse train with repetition rate of up to 346 GHz was demonstrated [70]. A pulse train with repetition rate of up to 238 GHz was also achieved using the harmonic mode-locking method [32].

In this chapter, we present experimental investigations on high repetition rate pulse generation from QD MLLs with external cavities. In section 5.2, high repetition rate and short duration pulse trains of 10 to 100 GHz from monolithic single-section QD MLLs will be reported. Then in sections 5.3-5.5, ultra-high repetition rates of 403 GHz, 437 GHz, 394 GHz and 1.01 THz will be successfully demonstrated from QD cavity combined with external cavity structure. The whole cavity consists of an InAs/InP QD cavity and external cavities of eight or three FBGs. In this MLL, the InAs/InP QDs provide gain and nonlinearities, and the FBGs are used to select and enhance desired

longitudinal modes. Different drive currents, couplers, QD lasers, and FBGs are combined in the experimental setup. FWM side bands are observed on the spectrum, indicating phase correlation between the FBG selected modes. Pulse train in the time-domain is also obtained through the autocorrelator, demonstrating fully or partially phase locking between these enhanced longitudinal modes. Finally, a summary is given in section 5.6.

5.2 High repetition rate InAs/InP monolithic QD MLLs

We have designed, grown and fabricated single-section InAs/InP QD MLLs of different cavity lengths, where the repetition rates range from 10 GHz to 100 GHz in C or L band. With the active cavity lengths of 4300 μm and 430 μm, repetition rates of 10 GHz and 100 GHz are obtained. There corresponding optical spectra are shown in Fig. 5.1 (a) and (b), respectively.

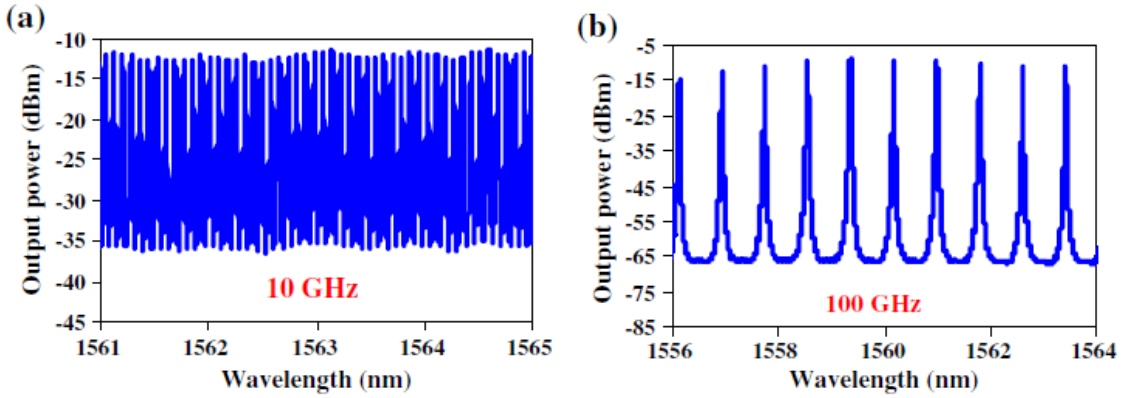

Fig. 5.1. Typical optical spectrum from the developed InAs/InP QD MLLs with the repetition rate of 10 GHz and 100 GHz, respectively.

The QD MLLs at repetition rates of 92 GHz and 46 GHz at C and L band have also been demonstrated from 456- and 930-μm-long cavities, respectively [68, 69]. The 3-dB bandwidths are 11.62 and 13 nm, respectively. Short pulse widths of 312 and 445 fs have

been achieved. Assuming Gaussian shape pulses, the TBPs are calculated to be 0.457 and 0.69, respectively, indicating some residual chirp in the pulses.

Besides, dual-wavelength self-mode-locked laser at 92.5 GHz is also successfully generated from single-section InAs/InP QD MLLs for the first time [58]. With increased bias current, the spectrum is broadened and split into a two-peak structure. Both peaks are self-locked but dependent. At the current of 60 mA, the centers of the two bands are at 1543.7 nm and 1571.7 nm and pulse widths are of 657 fs and 955 fs, respectively. It is found that the higher the biased current, the wider the splitting peaks. Thus the two-band phenomenon is different from GS/ES lasing structures as reported in other dual-peak QD lasers. Rabi splitting might have caused the two-band phenomenon.

These promising results, largely attributed to the unique properties of QD gain materials, open a breakthrough direction to design high performance fs pulse sources and low timing jitter components for ultra-high-bit-rate optical communications and signal processing.

5.3 403 GHz repetition rate pulse generation using a 856-μm-long QD laser and eight FBGs

5.3.1 Experimental setup

The experimental setup for the QD MLL, for generating the high repetition-rate pulses, is shown in Fig. 5.2. The InAs/InP QD waveguide was grown by CBE and fabricated to an Fabry-Perot laser with a ridge width of 3 μm and cavity length of 850 μm [68]. One facet has a high-reflectivity coating and the other is cleaved.

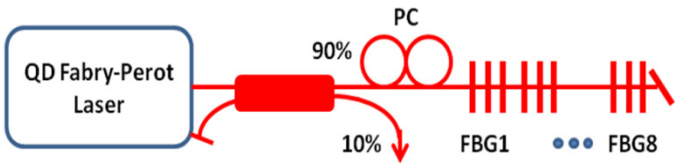

Fig. 5.2. Schematic diagram of the QD-MLL for generating the 403 GHz repetition-rate pulse train. PC: polarization controller, and FBG: fiber Bragg grating.

The threshold of the QD Fabry-Perot laser is 41 mA. In the experiment, the QD Fabry-Perot laser is biased above the threshold and the temperature is stabilized at 18ºC. Above the threshold, the QD Fabry-Perot laser emits hundreds of longitudinal modes with the free spectral range (FSR) of 50.25 GHz (i.e. mode spacing), as shown in the inset of Fig. 5.3 (a) at the biased current of 112 mA. The external cavities include eight FBGs with central wavelengths at 1531.78, 1534.86 (3.08), 1538.06 (3.20), 1541.26 (3.19), 1544.45 (3.19), 1547.45 (3.01), 1550.96 (3.5), and 1553.97 nm (3.02), where the values in the brackets indicate the frequency spacing in nm with respect to the previous FBG. The spacing in frequency and wavelength scales are both shown in Table 5.1. The eight FBGs were written in series in a single piece of fiber to form eight external fiber cavities. The reflectivity of each FBG is approximately 95% and the FWHM of the reflecting band is about 0.15 nm. The transmission optical spectrum of the eight FBGs is shown in Fig. 5.3 (a), measured by a broadband optical source.

Table 5.1 List of the grating parameters in the external cavity.

Number of grating	Grating reflection wavelength (nm)	Spacing in wavelength (nm)	Spacing in frequency (GHz)
1	1531.78	--	--
2	1534.86	3.08	393.80
3	1538.06	3.20	408.27
4	1541.26	3.19	404.79
5	1544.45	3.19	402.61
6	1547.45	3.01	378.32
7	1550.96	3.5	438.74
8	1553.97	3.02	376.39

The QD Fabry-Perot laser is connected with the eight FBGs by a 90/10% optical coupler through a lensed fiber and a polarization controller. The lensed fiber provides high coupling efficiency from 3-μm waveguide ridge to the fiber pigtail. The optical spectrum from the QD Fabry-Perot laser is illustrated in Fig. 5.3 (a) inset, showing hundreds of longitudinal modes in the C band. The 90% port of the coupler is connected to a polarization controller while the 10% port is used for measurement. Reflected lights by the FBGs are transmitted forth and back into the QD Fabry-Perot laser through the 90% port of the optical coupler. All the passive elements in the cavity have meter-long fiber pigtails and are connected through angle-polished connectors, avoiding light reflection at the connectors. The external cavity length is estimated to be 8.8 m, obtained by the fact that there are 17 modes within the frequency band of 200 MHz, observed by an electrical spectrum analyzer. The polarization controller is used to control the light polarization between the external cavities and the QD Fabry-Perot laser. Two optical terminators are connected to FC/APC connectors at the fiber ends to avoid any back reflection. The optical spectrum is observed by an OSA and the time-domain pulse is measured by an autocorrelator. Optical light entering the autocorrelator is separated into two parallel arms

where one of them has a variable delay line. Then the two beams are focused into a nonlinear crystal to generate second-order harmonic. The output signal is proportional to the product of the intensity of the two beams and a function of the delay time. The result is observed on an oscilloscope and the autocorrelation width of a pulse is proportional to the real pulse width. For a Gaussian pulse, the autocorrelation width is $\sqrt{2}$ times longer than the real pulse width and for a sech^2 shape pulse, it is 1.54 times longer. Only pulse width can be measured in this way but not the pulse phase.

5.3.2 Experimental results and discussions

As shown in the inset of Fig. 5.3 (a), there are hundreds of longitudinal modes emitting from the QD Fabry-Perot laser. However, because the eight FBGs are connected to the QD Fabry-Perot laser for the external cavities, only the longitudinal modes, whose wavelengths are within the reflecting bands of the FBGs, can be transmitted forth and back, and thus are enhanced by QD waveguide gain and the external cavities. The alignment between the FBG reflecting bands and QD Fabry-Perot laser modes can be optimized by tuning the biased current that shifts the wavelengths of the longitudinal modes. Fig. 5.3 (b) shows the measured optical spectrum from the QD Fabry-Perot laser with the external cavities when the biased current is 112 mA, and the optical spectrum is located in the C band with the central wavelength around 1540 nm. It is seen that there are several strong light peaks created, which are separated by 403 GHz in frequency, determined by the frequency separation of the FBGs, in addition to the original hundreds of weak longitudinal modes with the mode separation of 50.25 GHz in frequency. These strong light peaks are referred to the modes, supported by the external cavities. It can be further observed that there are eight light peaks or modes corresponding to the reflecting

bands of the FBGs, even though the two peaks at 1550.96 and 1553.97 nm (i.e. two longest wavelengths) are weak compared with the other six peaks. This is because the external cavity supported modes strongly depend on the alignment of the QD Fabry-Perot laser modes and the reflecting bands of the FBGs. When the frequency spacing between the FBGs does not equal to multiples of the FSR of the QD Fabry-Perot laser, the external cavities hardly enhance any modes. Nevertheless, we have obtained five strong peaks at 1531.70, 1534.85, 1538, 1541.17 and 1544.36 nm. In addition, note that there are three spurious light peaks at 1522.35, 1525.46 and 1528.57 nm as shown in Fig. 5.3 (b), where there are no reflecting bands of the FBGs (the light peak at 1522.35 nm is very small). It is clearly shown that almost equal frequency separation between all the light peaks (including the spurious light peaks) is obtained. This suggests that FWM between the five strong light peaks occurs inside the QD waveguide. In other words, the three spurious light peaks are generated by FWM between these strong light peaks. Thus, due to the FWM that is phase sensitive, all the strong light peaks are phase correlated. Consequently, the phase locking between these strong light peaks is achieved. Furthermore, the observed FWM effect is much more evident and clear than that in the previous reports [29, 58, 68, 70].

To further verify the above observations, we decrease the bias current to 110 mA and tune the polarization, seven strong light peaks corresponding to the reflecting bands of the FBGs are observed as shown in Fig. 5.3 (c), and one strong light peak is created at 1553.97 nm, which is not strong enough in Fig. 5.3 (b). It is seen that there are three spurious light peaks generated in the shorter wavelengths (1522.34, 1525.43 and 1528.55 nm) and two spurious light peaks generated in the longer wavelengths (1557.26 and

1560.53 nm). This further verifies the FWM occurrence inside the QD waveguide. It is also further suggested that the FWM process in InAs/InP QD waveguide is broadband, i.e. covering the C-band for our case.

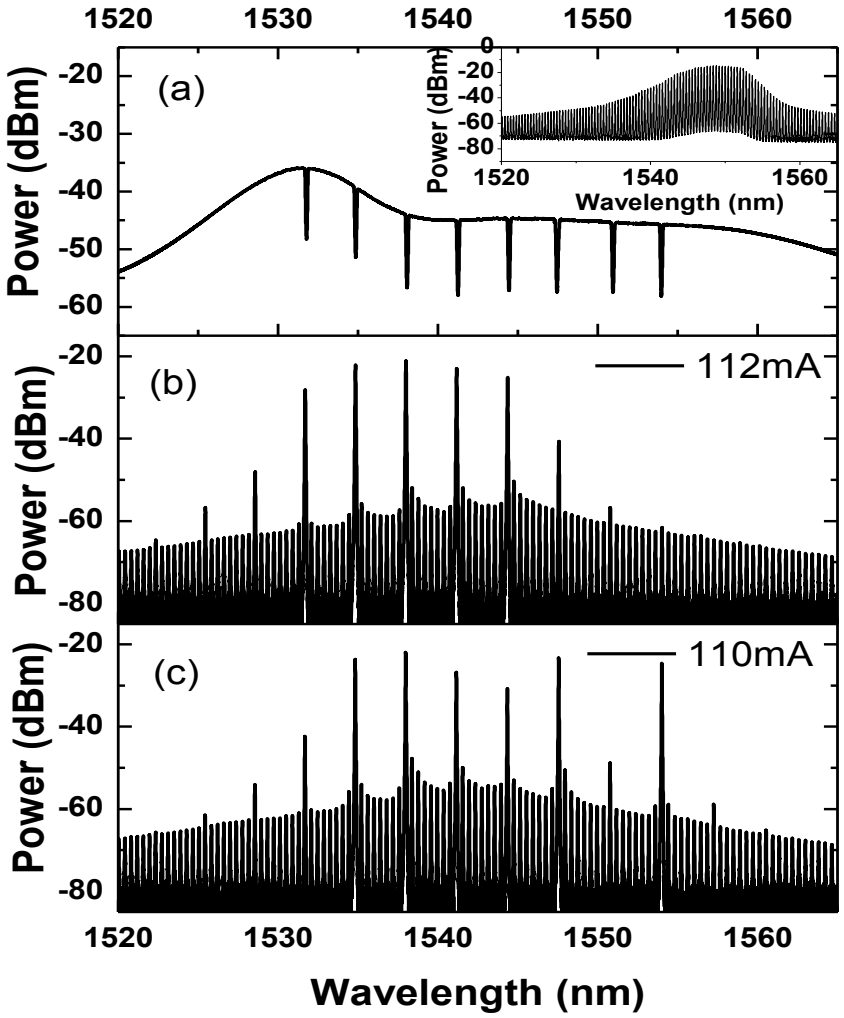

Fig. 5.3. (a) Transmission optical spectrum of the FBGs. Inset: optical spectrum of the QD Fabry-Perot laser at the biased current of 112 mA. (b) Measured optical spectrum of the QD-MLL with the external cavities of eight FBGs, at the biased current of 112 mA. (c) The same as in (b) but at the biased current of 110 mA. Optical resolution used is 10 pm.

To show the mode locking, the pulse train is measured using the intensity autocorrelator. For the case at the biased current of 112 mA as shown in Fig. 5.3 (b), a pulse train with a period of 2.48 ps is exhibited as shown in Fig. 5.4 (a), corresponding to

a 403 GHz repetition rate. The period is determined by the frequency spacing of the strong light peaks as shown in Fig. 5.3 (b). The formation of the pulse train demonstrates the successful mode-locking in the C-band QD Fabry-Perot laser with the external cavities. By assuming a Gaussian pulse shape, the FWHM of the pulse is approximately 563 fs.

For the case at the biased current of 110 mA in Fig. 5.3 (c), a 403 GHz repetition-rate pulse train is also generated successfully although there are side lobes between the pulses as shown in Fig. 5.4 (b). Excluding the side lobes, the FWHM of the pulse is about 268 fs by Gaussian fitting. The narrower FWHM in Fig. 5.4 (b) can be explained as follows: seven strong light peaks, which occupy more optical bandwidth as shown in Fig. 5.3 (c), involve in the FWM process that leads to mode-locking, rather than the five strong light peaks that occupy less optical bandwidth as shown in Fig. 5.3 (b). In addition, because the light peak at 1550.96 nm is weak, the optical spectrum in Fig. 5.3 (c) is equivalent to dual emission bands. The light peaks above 1550.96 nm are considered one band and the rest is considered the other band. It was found that dual emission bands lead to narrower pulse width [42]. Therefore, the narrower pulse width in Fig. 5.4 (b) is attributed to two reasons: broader optical spectrum and dual emission bands.

It is assumed that all the light peaks contributing to the 403 GHz pulse generation in the spectrum have equal phase and negligible amplitude noise and phase noise. The calculated pulse train by Fourier synthesis is shown in Fig. 5.5 (a) and (b) corresponding to Fig. 5.4 (a) and (b). The narrowing effect and side lobes between pulses are clearly shown in Fig. 5.5 (b).

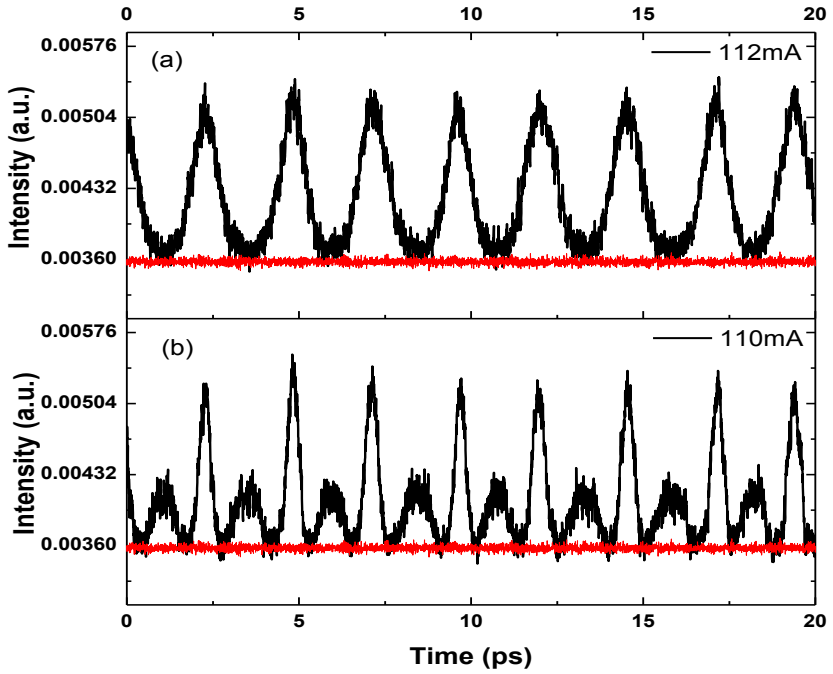

Fig. 5.4. Measured autocorrelations of the pulse train indicating the period of 2.48 ps, which corresponds to a repetition rate of 403 GHz at the biased current of (a) 112 mA and (b) 110 mA. The red line indicates noise level of the autocorrelator. The intensity autocorrelation is measured based on second harmonic generation with a time resolution of 10 fs.

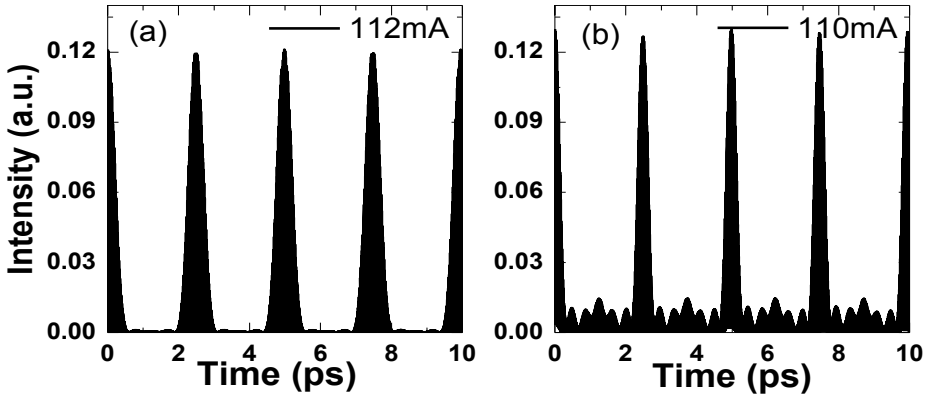

Fig. 5.5. Calculated pulse trains using Fourier synthesis for the spectra in Fig. 2 (b) and (c) by only taking all the light peaks reflected by the FBGs and generated by FWM.

High conversion efficiency of FWM effect in QDs has been found [92, 167]. The FWM effect is dependent on phase-matching that is related to linear chromatic dispersion of the QD waveguide and materials and nonlinear effect of the QD materials. As shown

in Fig. 5.3 (b) and (c), the FWM occurs over the C-band in InAs/InP QDs. This suggests that a small and flat linear chromatic dispersion over the C-band is compensated by the nonlinear effect of InAs/InP QDs. As a result, FWM between the strong light peaks indicates phase locking and mode locking, as explained in [29, 58, 68, 70, 165].

We have successfully generated 268 and 563 fs pulse trains with a repetition rate of 403 GHz using a C-band InAs/InP QD Fabry-Perot laser and FBG external cavities, i.e. a C-band InAs/InP QD MLL. It is much more evident that FWM process inside QD waveguide is the key in achieving mode-locking.

5.4. 437 and 394 GHz repetition rate pulse generation using a 1-mm-long QD laser and eight FBGs

The same FBGs are then applied to another InAs/InP QD laser as the external cavity. The QD laser is similar to the previous one except for the cavity length, which is 1 mm in this case. The threshold current of the 1 mm QD laser is about 36 mA. And in the experiment, the temperature is also stabilized at 18ºC. The experimental setup is the same as the one in Fig. 5.2 except for the coupler ratio. The coupler used here is a 50/50% one, where half of the light is transmitted to the external cavity and the other half is sent to OSA and autocorrelator for observation. The optical spectrum at the DC current of 100 mA is shown in Fig. 5.6. The centre of the spectrum is at about 1542 nm and the FSR between the longitudinal modes is about 43.11 GHz.

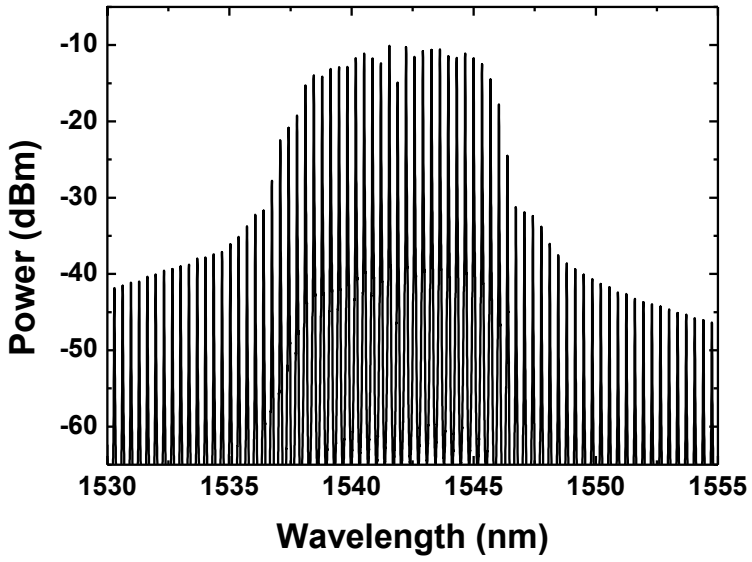

Fig. 5.6. Optical spectrum of a 1 mm InAs/InP QD laser at the current of 100 mA.

Fig. 5.7 (a) shows the measured optical spectrum with the external cavity. Longitudinal modes marked by B are generated by the stimulated emission in the Fabry-Perot cavity with QDs due to the uncoated facets with reflectivity of approximately 33%. Eight high peaks with optical power from -40 dBm to -10 dBm and almost equal spacing in the C band are clearly observed in the spectrum, marked as A in Fig. 5.7 (a). They were selected by the gratings in the external cavities, and then amplified and phase correlated in the QD Fabry-Perot cavity. The spacing of the gratings does not exactly equal to multiples of the FSR of the QD cavity, and eight longitudinal modes cannot be all selected at the same time by the eight gratings. Therefore, only four longitudinal modes within the reflection bands of the gratings at the current of 100 mA were highly reflected. Two FWM sidebands at about 1529 nm and 1557 nm marked as C are also observed in Fig. 5.7 (a). The optical light from one port of the 50/50% coupler was amplified to 10 mW and then measured with the intensity autocorrelator. A pulse train with a period of 2.29 ps was exhibited on the oscilloscope, corresponding to a 437 GHz

repetition rate as shown in Fig. 5.7 (b). The extinction ratio of the measured autocorrelation pulse train is 50% and the bottom of the pulses does not reach zero.

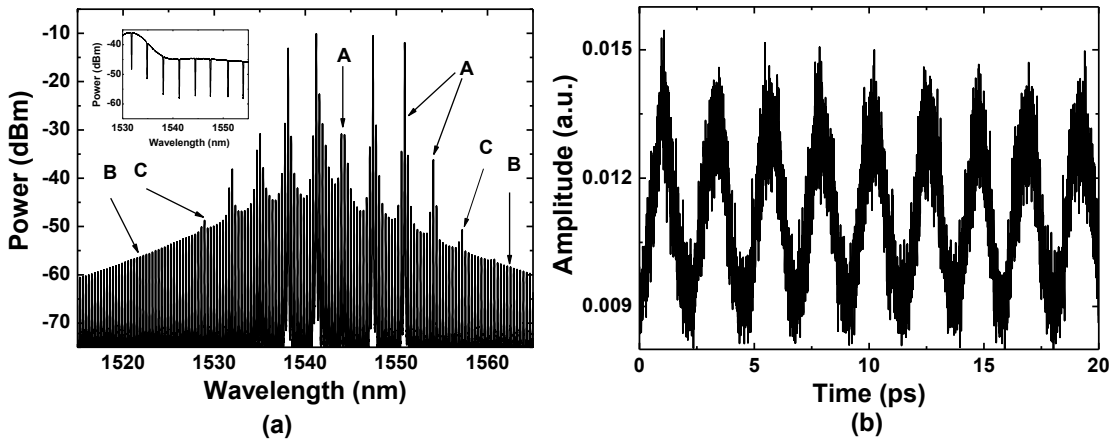

Fig. 5.7. (a) Measured optical spectrum of the MLL with eight gratings as external cavities and QDs as the gain medium. Longitudinal modes marked by A, B and C are generated by external cavities, the QD cavity, and FWM, respectively. Inset: eight transmission bands of the FBGs in the external cavity. (b) Autocorrelation of the pulse train with the periodic time of 2.29 ps, which corresponds to the repetition rate of 437 GHz.

The performance of the external cavity laser is also measured at the current of 42 mA, just above the threshold, as shown in Fig. 5.8. Besides hundreds of longitudinal modes with frequency spacing of 43.11 GHz, six high light peaks are observed in the spectrum corresponding to six external FBGs. Two FBGs with reflection bands of 1538.06 and 1553.97 nm does not reflect any longitudinal modes at this current due to the misalignment. No FWM side bands are observed perhaps due to the low power at the current of just above threshold. But the pulses are also obtained on the autocorrelator, indicating phase correlation between the high light peaks. The repetition rate is 2.54 ps, corresponding to the repetition frequency of 394 GHz.

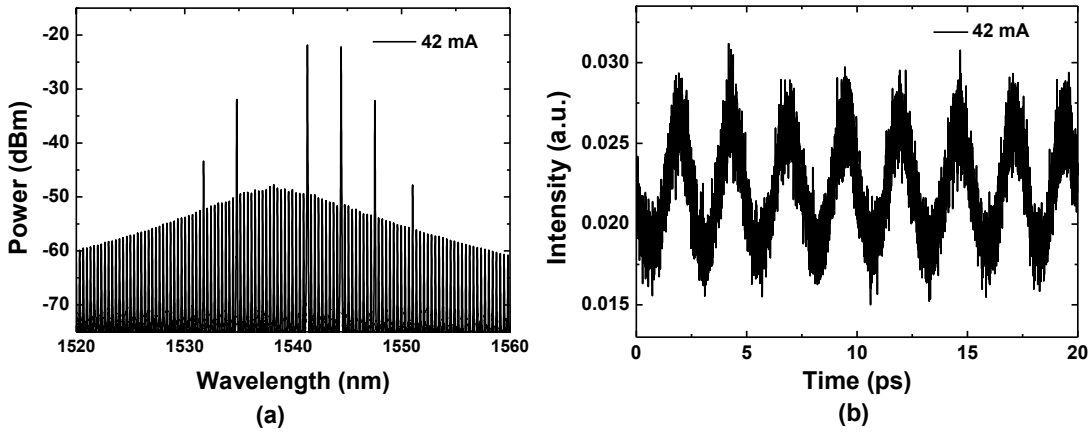

Fig. 5.8. (a) Optical spectrum and (b) time-domain pulses at the biased current of 42 mA with the external cavity structure.

The performance of the external cavity structure is also measured at a higher current of 154 mA as shown in Fig. 5.9. It is seen from the optical spectrum in Fig. 5.9 (a) that relatively high intensity longitudinal modes appear around each FBG reflected mode. This is because that the light intensity in the QD cavity itself is already very high at 154 mA and cannot be well suppressed by the external cavity. The beating of the FBG selected modes results in the generation of pulse train at 431 GHz as shown in Fig. 5.9 (b). And the envelope of the pulse train is modulated at 43.11 GHz due to beating of the unsuppressed longitudinal modes.

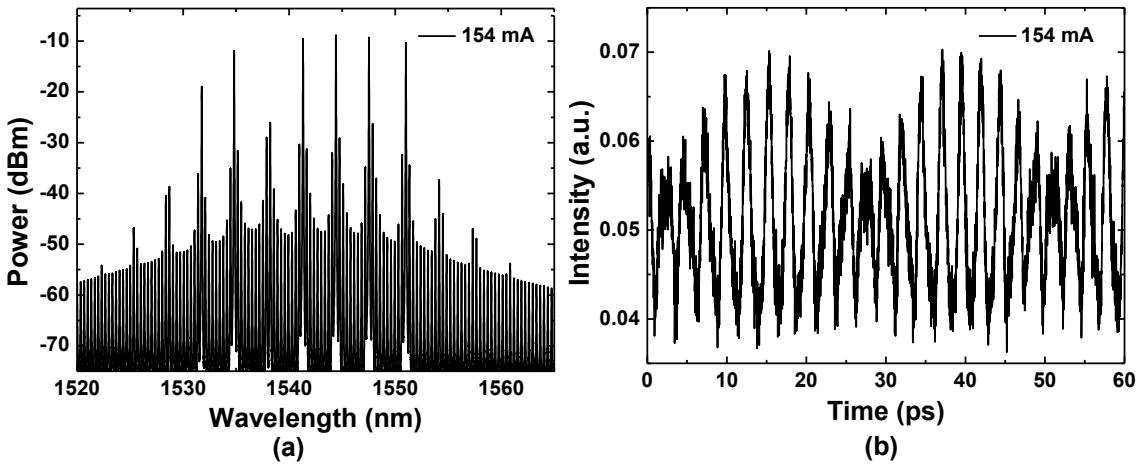

Fig. 5.9. (a) Optical spectrum and (b) time-domain pulses at the biased current of 154 mA with the external cavity structure.

Note that the slight difference in the repetition rate in the external cavity structure could be due to the reason that the frequency spacings between the FBGs are not exactly the same as given in Table 5.1, and the reflection bandwidth of the FBGs in the external cavity is about 0.15 nm, broader than the FWHM of the QD longitudinal modes.

It is seen that the performance is better using the 850-μm QD cavity as the gain material than that using the 1-mm QD cavity. The alignment between the two cavities is very crucial in generating high quality and high repetition rate pulses. It is expected that eight higher peaks in the spectrum and shorter pulse width can be obtained if the wavelength spacing of the gratings exactly equals to multiples of the FSR of the QD cavity.

5.5 THz repetition rate pulse generation using a 1-mm-long QD laser and three FBGs

Higher repetition rate could be reached with wider frequency separation between gratings. The frequency spacing between gratings needs to be multiples of FSR of the QD cavity.

By using this scheme, even higher repetition rate of up to the THz range has been demonstrated. The experimental setup is the same as before except the number of FBGs and spacing between the FBGs in the external cavity. The optical transmission spectrum of the three FBGs in series is shown in Fig. 5.12 (a). Their central Bragg wavelengths are 1531.868 nm, 1539.656 nm, and 1547.506 nm, with peak reflectivity of 96% and FWHM of 0.080 nm. The inter-FBG frequency spacing is approximately 1.01 THz.

The QD cavity in use is 1 mm long with ridge width of 3 μm. One facet of the QD laser is highly coated with 95% reflectivity and the other facet is as cleaved giving a 31% reflectivity. The coupler ratio is 90/10%, where the 90% port is connected with the external cavity and the 10% port is used for observation. And the temperature is controlled at 18^{o} C for the QD laser.

The working principle is the same as the previous QD coupled external cavity with eight FBGs. These external fiber cavities only reflect longitudinal modes (of the QD Fabry-Perot cavity) within the reflecting bands of the FBGs to the QD gain medium, and the rest are transmitted. The selected modes could be optimized in terms of amplitude and wavelength by adjusting the QD laser bias current or temperature to shift the frequency comb of the QD Fabry-Perot laser. Due to the reduction in optical loss of the whole system at the FBG back-reflection wavelengths, the coupled-cavity laser can lase at a bias current below that of the bare QD Fabry-Perot device, 48 mA.

The optical spectra of the external cavity structure from 32 to 40 mA, below the threshold of the QD Fabry-Perot laser, are shown in Fig. 5.10. At the current of 32 mA, two small modes at the wavelengths of 1539.57 and 1547.524 nm, corresponding to the second and third FBGs, start to appear in the spectrum. Then the mode at 1547.524 nm

gets enhanced to about -28 dBm at the current of 34 mA while the intensity of the other one is still very low, about -50 dBm. With further increasing the current, the mode at 1539.566 nm gets amplified to -23 dBm at 37 mA and the third mode at 1531.768 nm is observed at the current of 40 mA. With the external cavity, not only lasing occurs below the original threshold of the QD Fabry-Perot laser, but also the pulse train is observed in the time-domain. The measured pulse trains at the currents of 37 mA and 40 mA by the autocorrelator are show in Fig. 5.11, corresponding to the optical spectra in Fig. 5.10 (c) and (d), respectively. At 37 mA, two sets of pulse trains are observed, the lower repetition rate is about 43.57 GHz and the higher one is about 989.02 GHz, generated by the original QD cavity modes and the FBG selected modes, respectively. At 40 mA, the original cavity modes are further suppressed and the FBG selected modes are further amplified, where only one set of pulse train with repetition rate of 999.3 GHz is observed in Fig. 5.11 (b).

The beating indicates the two FBG selected modes start to establish phase correlation even at very low current. The pulse quality is improved with increased bias current by comparing Fig. 5.11 (a) and (b).

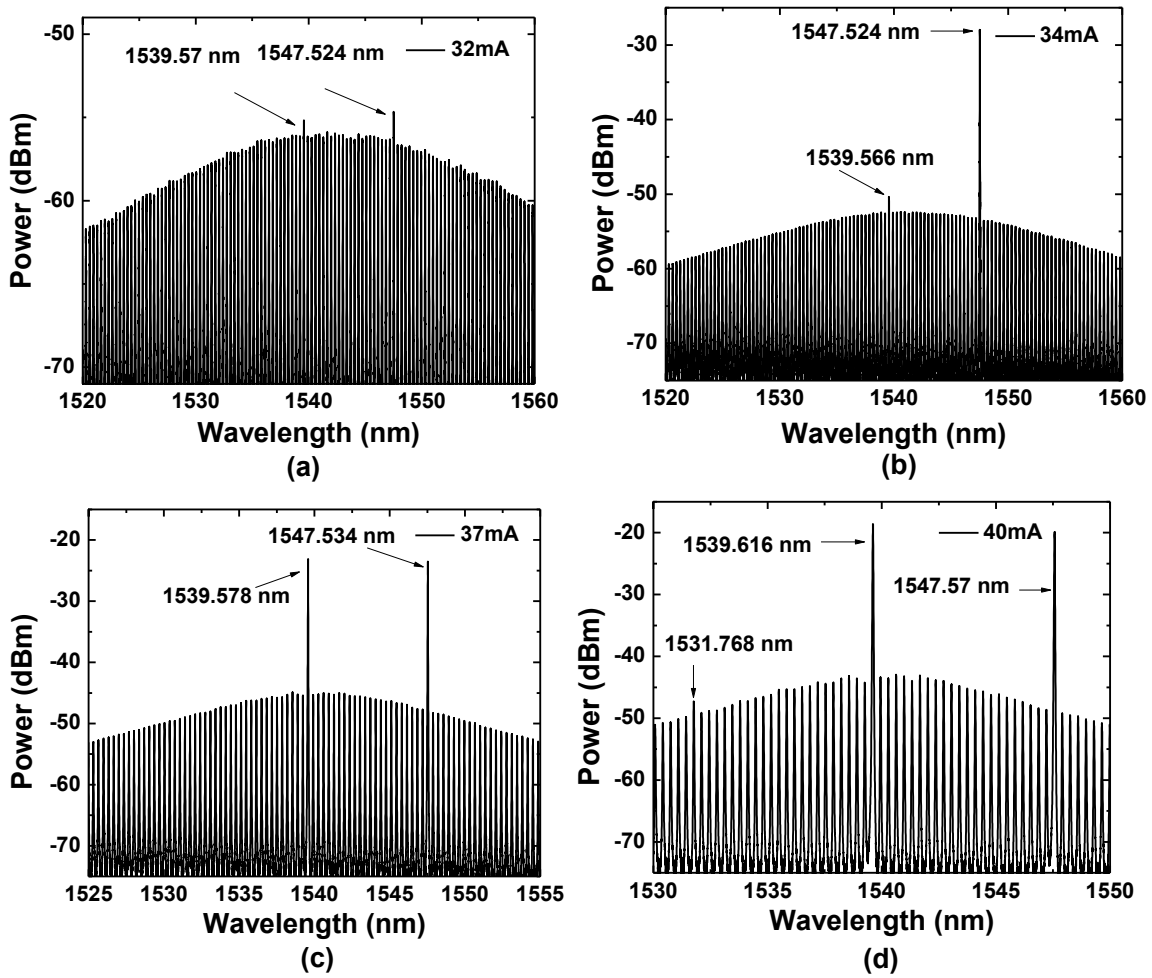

Fig. 5.10. Optical spectra change with the increase of the biased current in the QD coupled external cavity structure. From (a) to (d), the FBG selected modes appear and get enhanced with the current. The wavelengths of the selected modes are indicted in the figure.

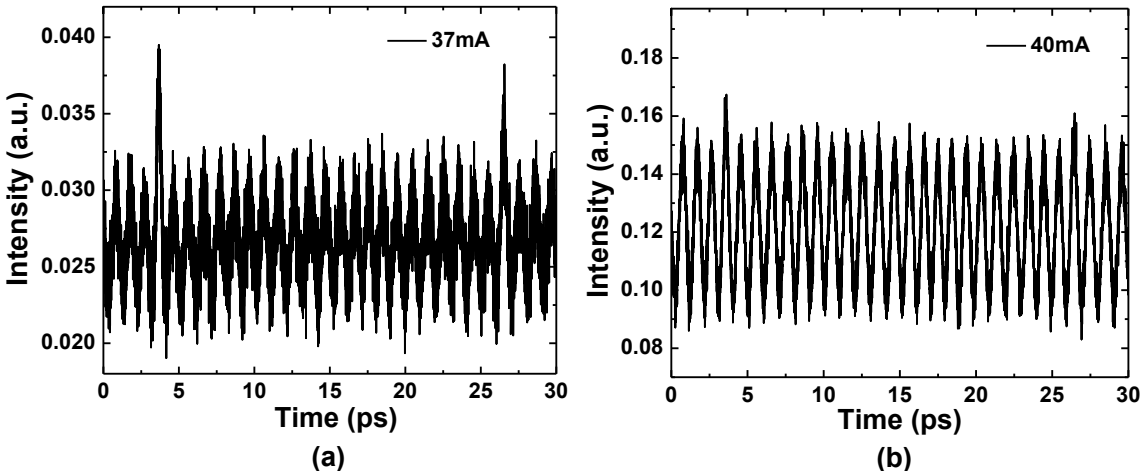

Fig. 5.11. Time-domain pulse train in the external cavity structure at the current of (a) 37 mA and (b) 40 mA.

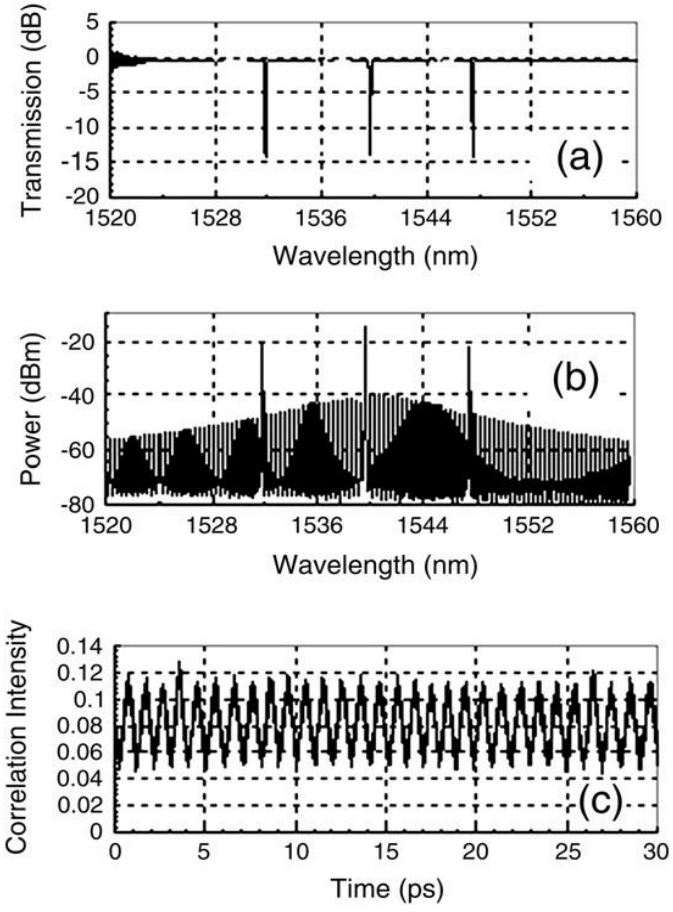

Fig. 5.12. (a) Transmission spectrum of the three FBGs. (b) Lasing spectrum of the coupled-cavity QD laser at a bias current of 45 mA. (c) Pulse train indicating the repetition rate of 1.01 THz.

Then at the current of 45 mA, all the three FBG selected modes are amplified and can be clearly observed from the spectrum in Fig. 5.12 (b). The spectrum is dominated by three lasing modes at 1531.827 nm, 1539.655 nm and 1547.548 nm. These correspond to the reflection bands of the FBGs. The resulting pulse train, with a pulse period of about 1.0 ps as shown in Fig. 5.12 (c), was measured and averaged over 64 times with an intensity autocorrelator. Its repetition rate and pulse duration are 1.01 THz and 0.5 ps, respectively. Due to the intensity or amplitude difference of the three lasing modes, the cw background of the laser pulses is high so that the pulse contrast is poor. The above results indicate that the external fiber cavities are controlling the lasing spectrum at low bias current, and that the three lasing modes are phase-correlated. This correlation is likely mediated through the strong FWM observed in QD gain media [91, 168].

The FWM is examined more carefully at the current of 47 mA. By tuning the temperature, the coupled-cavity laser could be made to operate on only two of the FBG-selected modes (the other FBG peak was mismatched from any longitudinal mode of the QD Fabry-Perot laser). FWM Stokes and anti-Stokes signals, labeled by the arrows in Fig. 5.13, were clearly observed at the wavelengths of 1547.5 nm and 1524.1 nm. By changing the frequency spacing and the number of FBG sets, laser pulses with different repetition-rates, bandwidth, and pulse duration could be produced, independent of the original QD Fabry-Perot cavity length [168]. The physical limitations on the high pulse repetition rate are whether the QD gain medium exhibits carrier dynamics fast enough to sustain successive pulse emission, and the efficiency of the FWM process.

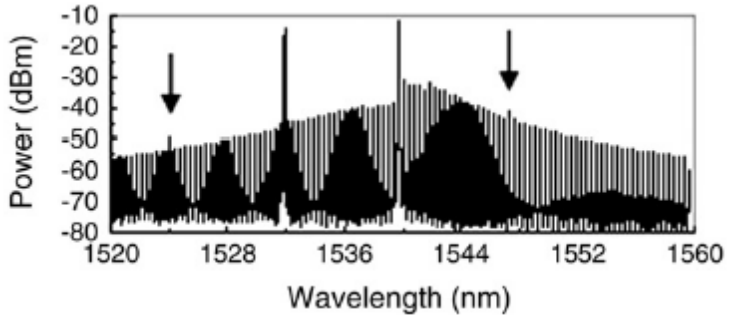

Fig. 5.13. Four wave mixing signals observed at a bias current of 47 mA.

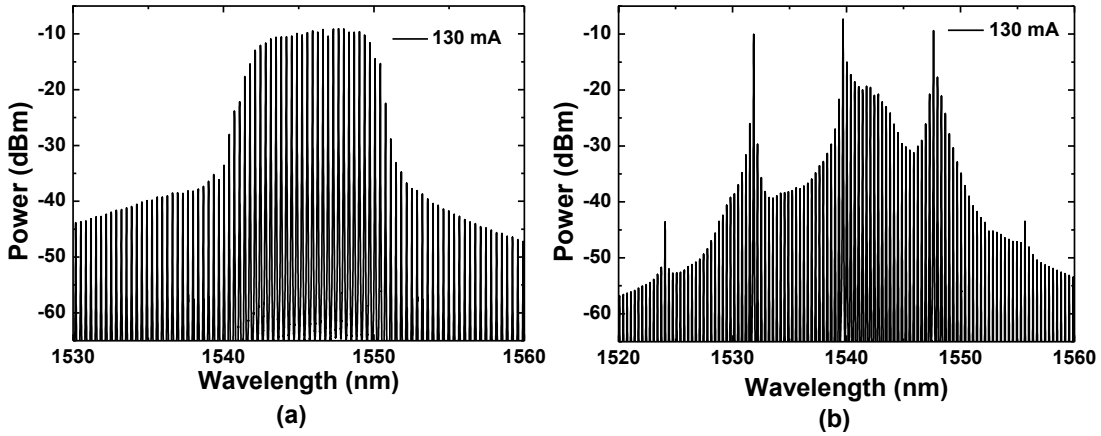

Fig. 5.14. Optical spectra of (a) the QD Fabry-Perot laser and (b) the external cavity coupled QD Fabry-Perot laser at the current of 130 mA.

Next we consider the lasing behavior of the coupled-cavity QD laser at high bias current. At this current regime the laser itself is lasing with tens of longitudinal modes simultaneously, three of which are enhanced by the feedback from the FBGs. Take the optical spectrum at the current of 130 mA for example. The original optical spectrum without the external cavity has hundreds of longitudinal modes centred at about 1545 nm as shown in Fig. 5.14 (a). With the external cavity, the longitudinal modes are suppressed and the FBG-selected modes are highly amplified in Fig. 5.14 (b). Two FWM side bands of about -43 dBm at 1524.082 nm and 1555.656 nm are also observed at this current. This results in a comb of modes with 43.8 GHz mode spacing and three dominant modes

with a 1.01 THz spacing. This is shown in Fig. 5.15 (b). Consequently, the envelope of 1.01 THz pulse train is modulated at a frequency of 43.8 GHz, with the modulation depths dependent on the weighting of the lasing modes. As the bias current is increased the modulation depth is also increased, as shown in Fig. 5.15. When the coupled-cavity laser is biased at a current of 175 mA the pulse train is dominated by pulses with a duration of less than 0.5 ps at a repetition rate of 43.8 GHz. A residual modulation at 1.01 THz could still be observed. Since at higher drive currents more lasing modes participate in the Fourier synthesis of the pulse trains [3], the cw background is significantly decreased and the pulse contrast is higher. Notice that the pulse duration for the 43.8 GHz pulse train shown in Fig. 5.15 (c) could be narrowed due to the modulation at a THz frequency [42].

Coupling a QD Fabry-Perot laser to external FBGs separated by 1.01 THz has allowed us to generate a 1.01 THz repetition-rate pulse train. The external cavity coupled laser starts to lase at the drive current of as low as 34 mA. At high drive current the repetition-rate becomes dominated by the cavity length of the QD Fabry-Perot laser, switching to a train of 0.5 ps pulses at 43.8 GHz.

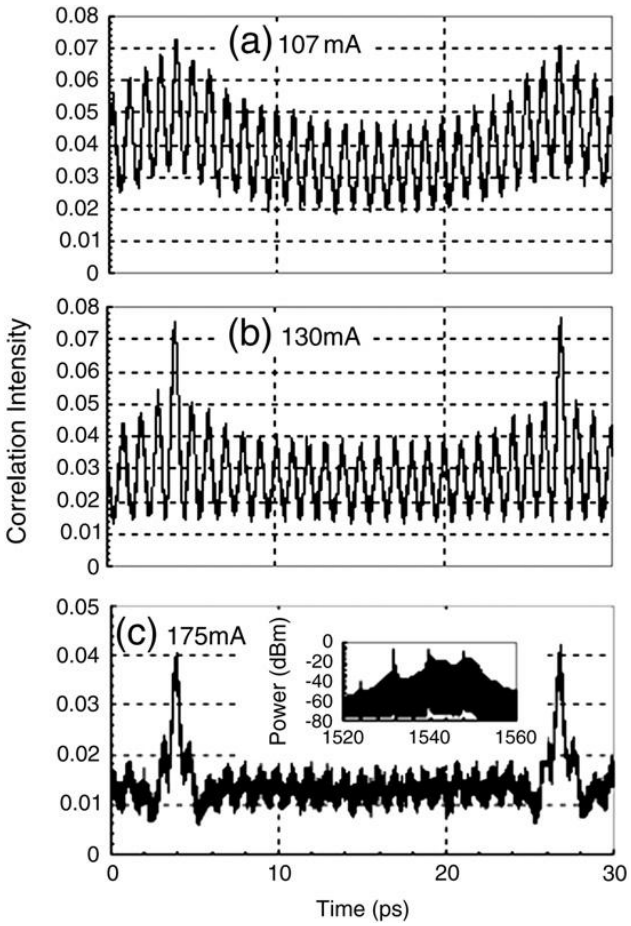

Fig. 5.15. Autocorrelation traces of the QD coupled-cavity laser biased at (a) 107 mA, (b) 130 mA, and (c) 175 mA, respectively. Inset in (c): the corresponding optical spectrum at 175 mA.

5.6 Conclusion

High repetition rate pulses of 403 GHz, 437 GHz, 394 GHz and 1.01 THz have been generated successfully from external cavity coupled QD lasers. To the best of our knowledge, the 1.01 THz is the highest repetition rate ever achieved using a QD semiconductor Fabry-Perot laser. The external cavity structure provides a new approach in generating ultra-high repetition rate pulses using QD lasers. It utilizes a QD gain medium as the potential source to provide extremely high repetition rate lasers, whose pulse rate, bandwidth, and even pulse duration can be readily tuned through spectrally

tailored optical feedback. The repetition rate is not limited by the QD cavity length, being controlled through the properties of the FBGs. FWM side bands are observed in the spectra, demonstrating phase correlation between the enhanced longitudinal modes.

Chapter 6 Tunable Terahertz Beat Signal Generation using an External-Cavity Coupled InAs/InP QD MLL

6.1 Introduction

Terahertz generation has attracted lots of interests in the applications of biomedical imaging and optical sensors. Terahertz beating can be generated by using two individual single-mode lasers [169, 170] with a wavelength difference tuned to a desired beat frequency, which can be then converted to THz radiation via a photomixer. The drawback of the method is the phase of the generated THz beating signal is uncorrelated. The use of a dual-mode laser diode offers a solution to the problem, where distributed Bragg reflectors [171, 172], Fabry-Perot filters [173], variable-bandwidth spectrum shapers [174], and V-structured end mirrors [175-177] have been used as external cavities for two wavelengths emission.

Previously reported dual-mode THz beating was based on bulk and QW materials, while no THz beating based on QD gain material has been reported and investigated yet. Two-color emission with a frequency difference of 8 THz has been reported by using a QD DFB laser with external optical feedback [178]. However, the frequency difference is fixed by the energy separation between the GS and ES.

In this chapter, we propose and demonstrate a C-band InAs/InP QD MLL combined with an external cavity, emitting a tunable THz beat signal. The external cavity includes two FBGs, where one has a fixed reflecting wavelength and the other is tunable. With the tunable FBG, beating frequencies from 1 to 2.21 THz in multiples of FSR of the QD MLL are demonstrated.

6.2 Experimental setup

The experimental setup for the tunable THz beat signal generation using a single-section QD MLL laser [58, 68] is shown in Fig. 6.1. The InAs/InP QD waveguide is grown by CBE and fabricated to an Fabry-Perot laser with a ridge width of 3 μm and cavity length of 850 μm [122]. One facet has a high-reflectivity coating and the other is cleaved. The threshold of the QD MLL is 41 mA. In the experiment, the QD MLL laser is biased above the threshold and the temperature is stabilized at 18ºC. Above the threshold, the QD laser is mode-locked at 50.25 GHz, which is determined by the cavity length. The optical spectrum of the QD MLL at the current of 100 mA is shown in Fig. 6.2, which emits hundreds of longitudinal modes centered at C-band with the mode separation of 50.25 GHz.

The external cavity includes an FBG with a reflecting wavelength at 1552.54 nm and a tunable FBG with reflecting wavelengths from 1525 to 1545 nm. The reflectivity of the two FBGs is about 95%. The FWHM of the reflecting band of the fixed FBG and the tunable FBG are about 0.5 nm.

The QD MLL is connected with the two FBGs by the two ports of a 50/50% optical coupler through a lensed fiber. Polarization controllers are used to optimize the reflected light between the FBGs and the QD MLL. An OSA is used to observe the spectra in the frequency domain. An autocorrelator with an EDFA at its input is used to obtain the pulse trains in the time domain.

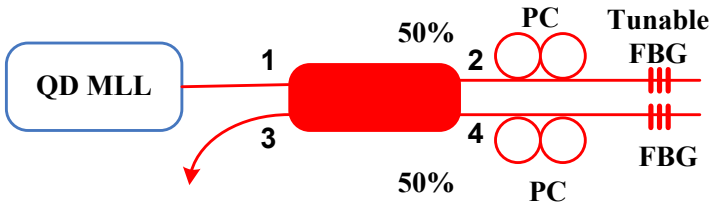

Fig. 6.1. Experimental setup for THz beat signal generation from an InAs/InP QD MLL. FBG: fiber Bragg grating, PC: polarization controller. Numbers 1-4 specify the four ports of the coupler.

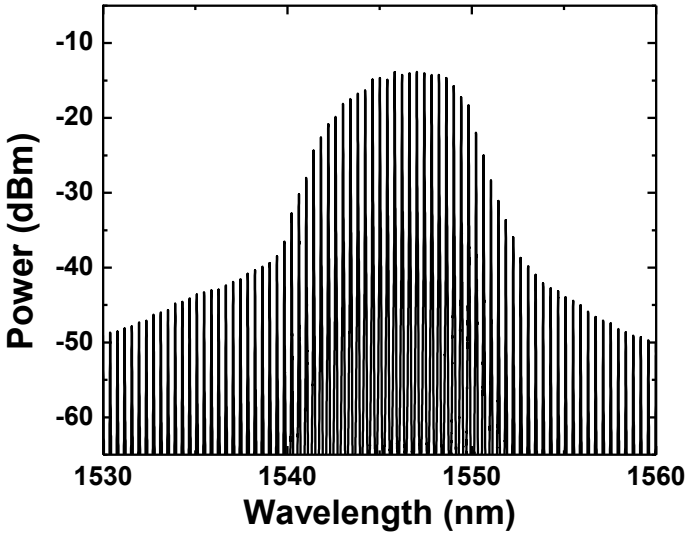

Fig. 6.2. Optical spectrum of the InAs/InP QD MLL used in the experiment at the current of 100 mA.

6.3 Experimental results and discussions

The optical spectrum after the EDFA and measured pulse train at the repetition rate of 50.25 GHz are shown in Fig. 6.3 (a), and (b), respectively. The output power is 11.5 mW before the lensed fiber.

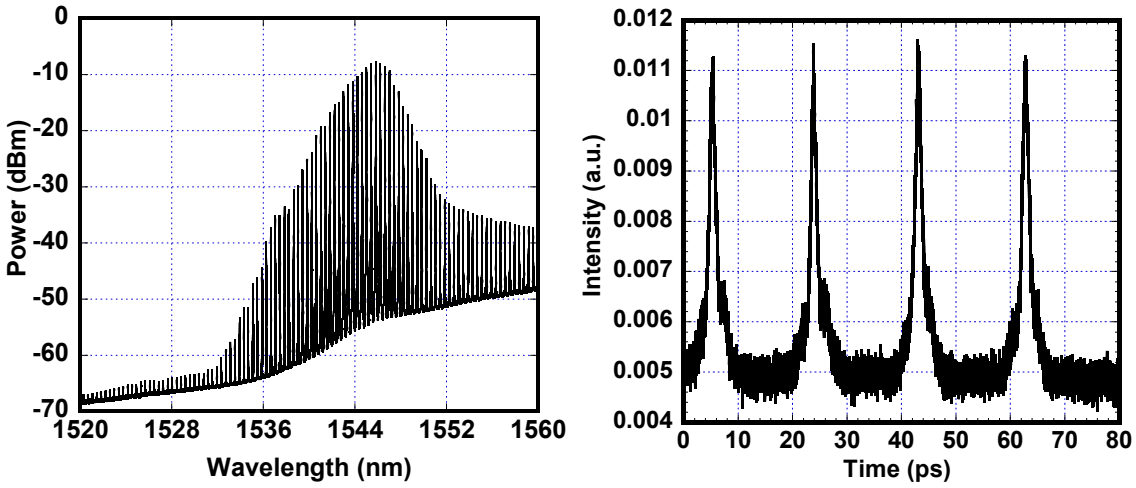

(a) (b)

Fig. 6.3. (a) Amplified optical spectrum and (b) measured pulse train of the QD Fabry-Perot laser at a biased current of 100 mA and temperature controlled at 18°C.

Fig. 6.3 (b) suggests that most longitudinal modes with high power are mode-locked, which means that they must be phase-correlated. By tuning the biased current, the wavelengths of the QD MLL modes can be shifted. The longitudinal modes within the reflecting bands of the two FBGs are transmitted forth and back, and thus are enhanced by QD waveguide gain and the FBG cavities. Each FBG can reflect one longitudinal mode, and two modes can be selected in the optical spectrum by the two FBGs. By adjusting the reflecting wavelength of the tunable FBG, different longitudinal modes of the QD MLL within the tuning range can be reflected and amplified, thus the tunability of mode separation and the beating frequency can be realized. The mode separation must be multiples of 50.25 GHz.

Now we consider the QD MLL with external cavity as shown in Fig. 6.1. The biased current is adjusted to 120 mA and the temperature is maintained at 18°C. As some examples, the reflecting wavelength of the tunable FBG is set to 1544.5, 1540.51, 1535.77 and 1534.96 nm. The reflecting wavelength of the fixed FBG is at 1552.53 nm

and thus the corresponding dual-mode separations between the two FBG reflected modes are 8.03, 12.02, 16.77 and 17.56 nm, respectively. The output power at port 3 is about 200 μW before the EDFA. Fig. 6.4 shows the optical spectrum for the above four cases, where one mode is fixed and the other is changed by the tunable FBG. Two high light peaks with the above mode separation, i.e. enhanced longitudinal modes reflected by the two FBGs, are observed in the optical spectrum. Other longitudinal modes of the QD MLL in the optical spectrum are highly suppressed.

Sinusoidal modulation due to mode beating between the two light peaks is necessary for photomixing. Measured optical sinusoidal signal using an autocorrelator is shown in Fig. 6.5. Corresponding to Fig. 6.4, the repetition frequency of the sinusoidal signal is the mode beat frequency of 1, 1.51, 2.11 and 2.21 THz. The corresponding pulse widths without considering the DC background are 315, 192, 158 and 169 fs.

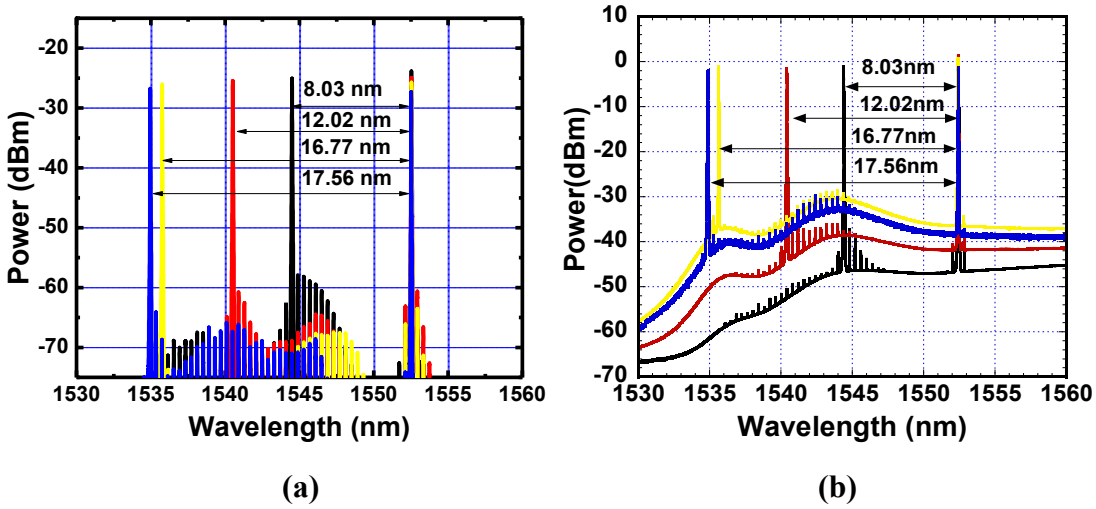

Fig. 6.4. Tunable dual-mode spectra (a) before and (b) after EDFA from 1 to 2.21 THz at the biased current of 120 mA. The temperature is controlled at 18°C. The mode separations are indicated in the spectrum.

Because the two modes share a common QD cavity and they are partially phase-locked by intracavity FWM processes [179] in the QD waveguide, it is believed that the

two modes are phase-correlated and thus the generated THz wave has much less phase noise. But it is difficult to measure the linewidth of THz beating signal based on the current availability of optoelectronic devices. However, to show the modes that are phase correlated even after adding the external cavities, we conduct the following verification. We connect two FBGs in series to the port 2 of the coupler, where one is the tunable FBG and the reflecting wavelength of the other one is at 1548.58 nm with FWHM of 0.33 nm and reflectivity of ~95%. Port 4 of the coupler is left unconnected to observe the optical spectrum. The reflecting wavelength of the tunable FBG is firstly set to 1540.5 nm. In Fig. 6.6 (a), two high peaks at 1540.5 nm and 1548.49 nm are the two modes reflected by the two FBGs. The frequency difference between them is 1 THz (8 nm). Besides the two high peaks, two small peaks at the wavelengths of 1532.61 and 1556.58 nm on the two sides of the high peaks have been also observed. It is clearly seen that the four peaks are equally spaced (~1 THz), which means that the two small peaks are generated by the FWM effect. This suggests that the FWM still occurs even after adding the external cavities. In other words, phase-locking is still partially retained after adding the external cavities. Therefore, the two high peaks are phase-correlated. To further verify the phase correlation, we increase the frequency separation of the two modes to 1.76 THz (13.92 nm) by tuning the reflecting wavelength of the tunable FBG to 1534.57 nm. Newly generated wave by FWM appears at 1521.14 nm as shown in Fig. 6.6 (b). And the spacing between the newly generated peak and the peak at 1534.57 nm is 1.73 THz, almost equaling to the frequency separation between the two high peaks. This shows that the FWM effect exists even with the frequency separation of 1.76 THz at C-band. This further verifies FWM occurrence in the QD waveguide plus external cavities.

Furthermore, it is indicated that the successful beat signal generation of up to 2.21 THz between the dual modes is attributed to strong intracavity FWM and fast dynamics in QD waveguides.

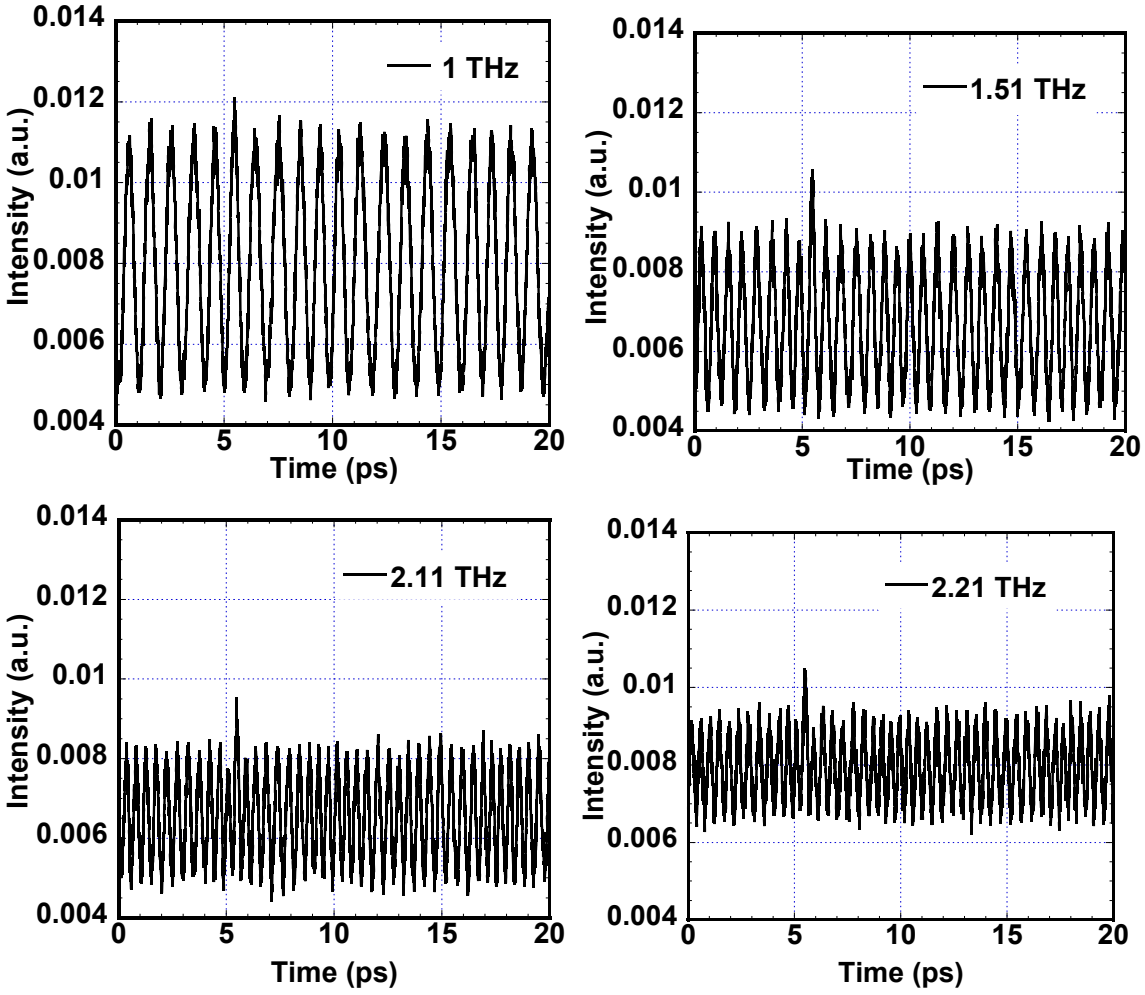

Fig. 6.5. Tunable beating frequencies from 1 to 2.21 THz in the time domain corresponding to the four mode-separations in Fig. 6.4.

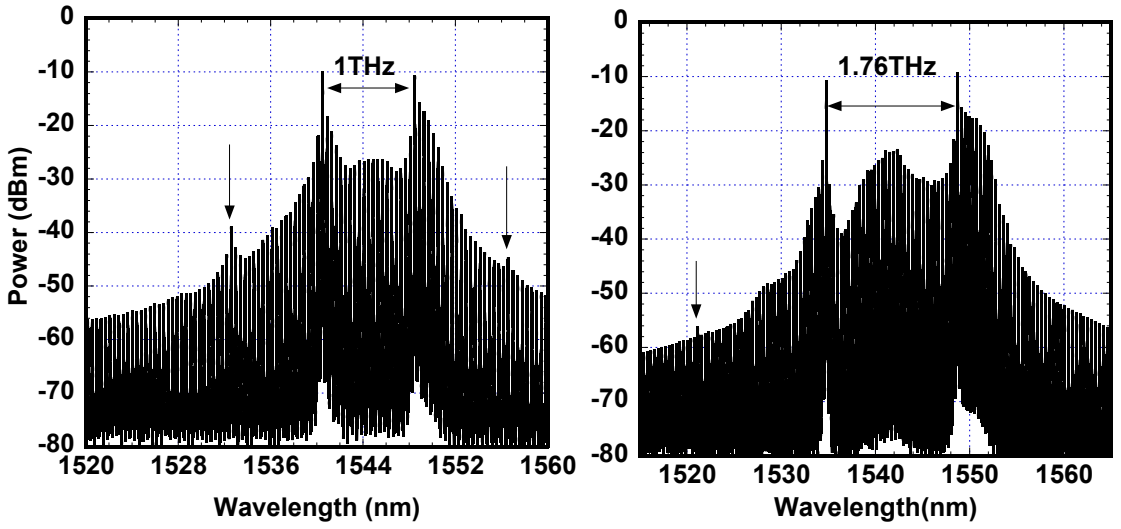

Fig. 6.6. Optical spectra of QD MLL with two FBGs of separations of (a) 1 THz at the biased current of 120 mA and (b) 1.76 THz at the biased current of 134 mA. The two FBGs are connected to port 2 of the coupler in series. The output power at port 4 is about 1.4 mW.

As shown in Fig. 6.5, the contrast ratio of the pulse trains is decreased with the increase of the dual-mode separation. Obviously, linear phase mismatch due to chromatic dispersion of the external cavities and QD waveguide is increased with the increase of beating frequency, thus intra-cavity FWM effect is reduced [149]. Consequently, the phase correlation may be reduced with the increase of THz signal. On the other hand, the beating signal is proportional to $\cos^2(\Delta\beta)$ in power, $\Delta\beta$ -total phase mismatch. Therefore, the contrast ratio is decreased with the increase of the dual-mode separation. This also indicates that the tuning range might be limited by the phase mismatch.

By tuning the current, two other different cases are observed as shown in Fig. 6.7. At 134 mA, two neighbor longitudinal modes are enhanced at the same time by the fixed FBG at 1552.54 nm and at 130 mA, two neighbor longitudinal modes are selected and amplified by each of the two FBGs. Due to the FWHM of the FBG reflecting band, when

it is positioned between two neighbor modes, both of them get amplified at the same time. Then correspondingly, the time-domain pulse is modulated by the beating of the two neighbor modes at 50.25 GHz.

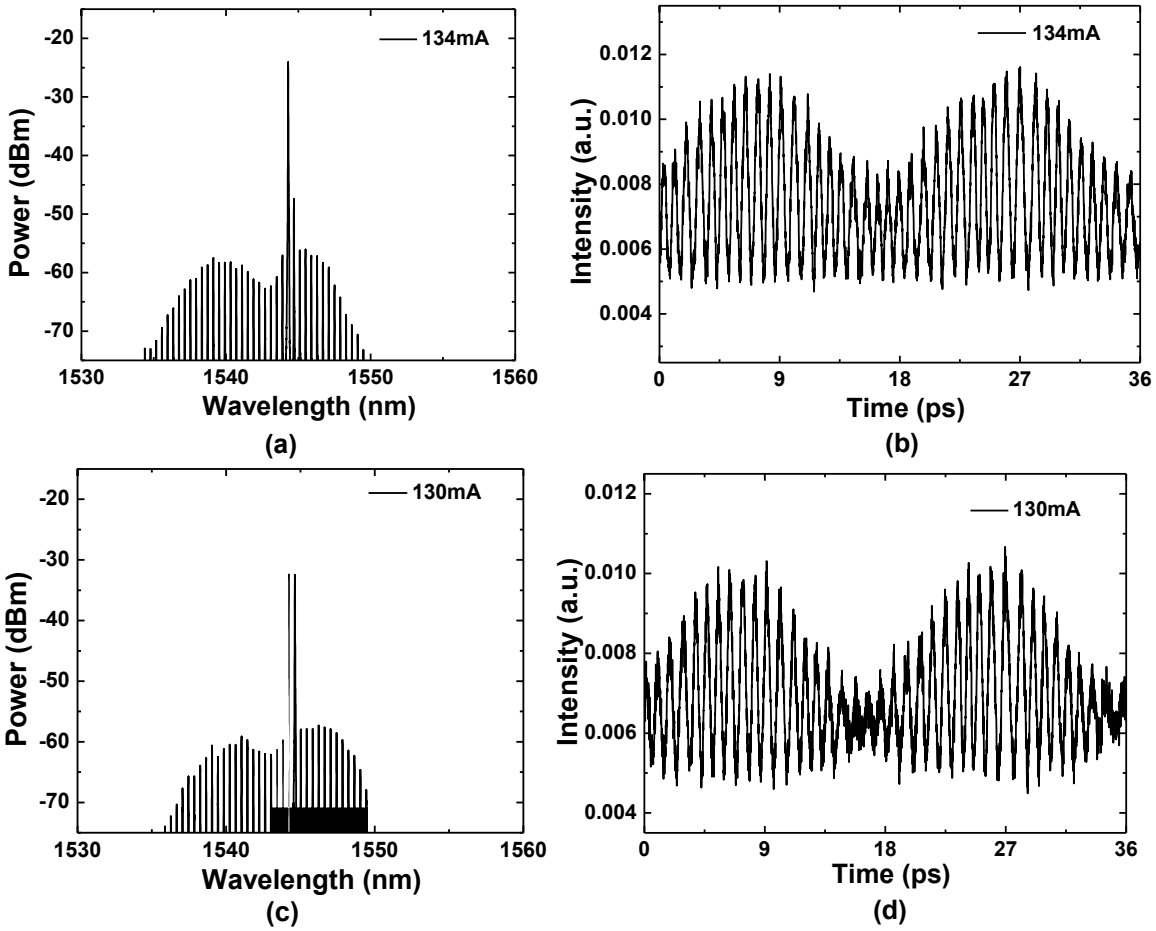

Fig. 6.7. Optical spectra and time-domain beating for two other different cases in the external cavity coupled QD laser.

6.4 Conclusion

The first generation of tunable dual-mode beat signal from 1 to 2.21 THz have been successfully demonstrated by using a C-band InAs/InP QD MLL and an external cavity of two FBGs. The beat frequencies can be tuned quasi-continuously in multiples of the fundamental repetition rate of QD MLL. Thanks to the use of one QD MLL, and

intracavity FWM effect, the dual modes are phase-correlated and therefore the generated THz will have much less phase noise.

The highest repetition rates reported in semiconductor MLLs by using QD and QW materials are 1.01 THz [122] and 1.5 THz [180], respectively. It is found that QD materials are promising for high-repetition-rate operation of up to 1 THz due to their ultrafast carrier dynamics [83]. This work shows that up to 2.21 THz beat signal can be generated using QD MLL and external cavities.

Chapter 7 Conclusions

The single-section InAs/InP QD MLLs are investigated comprehensively in this thesis. The following conclusions are drawn:

1. The LEF of our QD materials is found to be smaller than QW materials. We have measured the LEF parameter using two experimental methods. The measured LEF is around 1, and thus this material is considered suitable for making QD lasers and QD MLLs for the optical communication systems.
2. The improved TDTW model is established to simulate the single-section QD MLLs. Compared to the original TDTW model, an equivalent SA is proposed and the GVD and SPM terms are included. The importance of the proposed SA in mode-locking is verified by comparing the simulation results with and without the SA. The GVD and SPM effects on the pulse evolution are successfully predicted. With the two effects included, 1^{st}-order and 2^{nd}-order Taylor expansions are used to deduce an analytical expression for the electric field. The pulse duration and chirp as a function of the GVD parameter are obtained. The GVD effect is found to be the dominant one compared to SPM. The simulated results are in reasonable agreement with the experimental data. The role of the equivalent SA, FWM and SPM in the pulse evolution are also analyzed and discussed.
3. Ultra-high repetition rate pulses are successfully generated from a QD laser coupled with external cavity structure. The structure can overcome the limitation of repetition rates by the QD cavity, which is usually less than 100 GHz. The QD cavity provides gain and the external cavity selects amplified modes. High repetition rates from ~400 GHz to 1.01 THz have been obtained depends on the QD cavity and external-cavity

FBGs. The phase correlation between the FBG selected modes is demonstrated by the observations of the FWM sidebands on the optical spectra.

4. Furthermore, tunable THz beating of up to 2.01 THz is obtained using a similar configuration. Two longitudinal modes generated by the QD cavity are selected and amplified by the external FBGs. The phase correlation is also proved by FWM sidebands in the spectra. The two modes are from the same cavity, and thus less phase noise is expected. The beating signal may find potential applications in microwave photonics systems.

Future work can be focused on further improving locking performance of the QD MLLs, including pulse duration, peak power, phase noise, repetition rate, etc. For the generation of high repetition rate pulses using the external cavity structure, the external cavity can be controlled to improve the pulse quality. It can be temperature stabilized to reduce the wavelength shift of the longitudinal modes. The external cavity is fiber based FBGs in the experiment, the pigtails of which are of several meters long. The long external cavity can increase the total dispersion and lead to pulse broadening. It can be shortened to reduce phase noise and pulse duration. In using two FBG based external cavity to generate THz beating signal, the external cavity can also be temperature controlled and length shortened to improve the phase correlation of the two selected modes. For reducing the phase noise, injection locking and external feedback techniques can be applied. The injected light or feedback intensity/phase need to be optimized.

The mode-locking mechanisms in the single-section QD MLLs can be further explored. Both theoretical and experimental investigation are further required. To check the Kerr-lens effect, the far-field beam profile could be compared under cw and pulsed

state. Under pulsed condition, the profile should be broader than that of cw, undergoing self-focusing in the waveguide. The thickness of the dielectric blocking layer can be altered for different saturable loss [147]. For the FWM effect, we can design QD cavities with different FWM efficiencies in the cavity and observe the mode-locking strength at the same time. Besides, the GVD is proved to affect pulse durations in our QD MLLs. It can be decreased or compensated by waveguide design and facet coatings to get short and chirp-free pulses.

References

[1] K. Gürs, and R. Müller, “Breitband-modulation durch Steuerung der emission eines optischen masers (Auskopple-modulation),” *Phys. Lett.,* vol. 5, pp. 171-181, 1963.

[2] H. Statz, and C. L. Tang, "Zeeman effect and nonlinear interactions between oscillating laser modes," *Quantum Electronics III*, P. Grivet and N. Blombergen, eds., pp. 469-498, New York: Columbia Univ. Press, 1964.

[3] H. A. Haus, “Mode-locking of lasers,” *IEEE J. Sel. Topics Quantum Electron.,* vol. 6, pp. 1173-1185, 2000.

[4] S. Kasap, and P. Capper, *Springer handbook of electronic and photonic materials*: Springer, 2006.

[5] M. Asada, Y. Miyamoto, and Y. Suematsu, “Gain and the threshold of three dimensional quantum-box lasers,” *IEEE J. Quantum Electron.,* vol. QE-22, no. 9, pp. 1915-1921, 1986.

[6] D. Huffaker, G. Park, Z. Zou, O. Shchekin, and D. Deppe, “Continuous-wave low-threshold performance of 1.3 μm InGaAs-GaAs quantum-dot lasers,” *IEEE J. Sel. Topics Quantum Electron.,* vol. 6, no. 3, pp. 452-261, 2000.

[7] N. Kirstaedter, N. N. Ledentsov, M. Grundmann, D. Bimberg, V. M. Ustinov, S. S. Ruvimov, M. V. Maximov, P. S. Kop'ev, Z. I. Alferov, U. Richter, P. Werner, U. Gosele, and J. Heydenreich, “Low threshold, large T injection laser emission from InGaAs quantum dots,” *Electron. Lett.,* vol. 30, pp. 1416-1417, 1994.

[8] Y. Arakawa, "Progress in GaN based quantum dots for opto-electronics applications," *IEEE J. Sel. Topics Quantum Electron.,* vol. 8, no. 4, pp. 823-832, 2002.

[9] R. Dingle, and C. henry, *Quantum effects in heterostructure lasers*, US 3982207 A, 1976.

[10] N. N. Ledentsov, V. M. Ustinov, A. Y. Egorov, A. E. Zhukov, M. V. Maksimov, I. G. Tabatadze, and P. S. Kop'ev, "Optical properties of heterostructures with InGaAs-GaAs quantum clusters," *Semiconductors,* vol. 28, pp. 832-834, 1994.

[11] D. L. Huffaker, G. Park, Z. Zou, O. B. Shchekin, and D. G. Deppe, "1.3 μm room-temperature GaAs-based quantum-dot laser," *Appl. Phys. Lett.,* vol. 73, pp. 2564, 1998.

[12] O. B. Shchekin, and D. G. Deppe, "1.3 μm InAs quantum dot laser with T_0=161 K from 0 to 80°C," *Appl. Phys. Lett.,* vol. 80, pp. 3277, 2002.

[13] G. Park, O. B. Shchekin, S. Csutak, D. L. Huffaker, and D. G. Deppe, "Room-temperature continuous-wave operation of a single-layered 1.3 μm quantum dot laser," *Appl. Phys. Lett.,* vol. 75, pp. 3267, 1999.

[14] S. Freisem, G. Ozgur, K. Shavritranuruk, H. Chen, and D. G. Deppe, "Very-low-threshold current density continuous-wave quantum-dot laser diode," *Electron. Lett.,* vol. 44, no. 11, pp. 679-681, 2008.

[15] D. G. Deppe, K. Shavritranuruk, G. Ozgur, H. Chen, and S. Freisem, "Quantum dot laser diode with low threshold and low internal loss," *Electron. Lett.,* vol. 45, no. 1, pp. 54-56, 2009.

[16] M. S. Skolnick, and D. J. Mowbray, “SELF-ASSEMBLED SEMICONDUCTOR QUANTUM DOTS: Fundamental Physics and Device Applications,” *Annu. Rev. Mater. Res.,* vol. 34, pp. 181-218, 2004.

[17] Y. Arakawa, and H. Sakaki, “Multidimensional quantum well laser and temperature dependence of its threshold current,” *Appl. Phys. Lett.,* vol. 40, pp. 939-941, 1982.

[18] G. T. Liu, A. Stintz, H. Li, T. C. Newell, A. L. Gray, P. M. Varangis, K. J. Malloy, and L. F. Lester, “The influence of quantum-well composition on the performance of quantum dot lasers using InAs-InGaAs dots-in-a-well (DWELL) structures,” *IEEE J. Quantum Electron.,* vol. 36, no. 11, pp. 1272-1279, 2000.

[19] A. R. Kovsh, N. A. Maleev, A. E. Zhukov, S. S. Mikhrin, A. P. Vasil'ev, Y. M. Shernyakov, M. V. Maximov, D. A. Livhsits, V. M. Ustinov, Z. I. Alferov, N. N. Ledentsov, and D. Bimberg, “InAs/InGaAs/GaAs quantum dot lasers of 1.3 μm range with high (88%) differential efficiency,” *Electron. Lett.,* vol. 38, no. 19, pp. 1104-1106, 2002.

[20] T. Kageyama, K. Nishi, M. Yamaguchi, R. Mochida, Y. Maeda, K. Takemasa, Y. Tanaka, T. Yamamoto, M. Sugawara, and Y. Arakawa, “Extremely high temperature (220°C) continuous-wave operation of 1300-nm-range quantum-dot lasers,” in Lasers and Electro-Optics Europe (CLEO EUROPE/EQEC), 2011 Conference on and 12th European Quantum Electronics Conference, Munich, 2011, pp. 1.

[21] K. Kamath, J. Philips, H. Jiang, J. Singh, and P. Bhattacharya, "Small-signal modulation and differential gain of single-mode self-organized $In_{0.4}Ga_{0.6}As$/GaAs quantum dot lasers," *Appl. Phys. Lett.,* vol. 70, pp. 2952, 1997.

[22] S. Fathpour, Z. Mi, and P. Bhattacharya, "High-speed quantum dot lasers," *J. Phys. D: Appl. Phys.,* vol. 38, pp. 2103-2111, 2005.

[23] D. Bimberg, N. Kirstaedter, N. N. Ledentsov, Z. I. Alferov, P. S. Kop'ev, and V. M. Ustinov, "InGaAs-GaAs Quantum-dot Lasers," *IEEE J. Sel. Topics Quantum Electron.,* vol. 3, pp. 196-205, 1997.

[24] X. Huang, A. Stintz, H. Li, F. Lester, J. Cheng, and K. Malloy, "Passive mode-locking in 1.3 um two-section InAs quantum dot lasers," *Appl. Phys. Lett.,* vol. 78, pp. 2825-2827, 2001.

[25] M. G. Thompson, K. T. Tan, C. Marinelli, K. A. Williams, R. V. Penty, I. H. White, M. Kuntz, D. Ouyang, D. Bimberg, V. M. Ustinov, A. E. Zhukov, A. R. Kovsh, N. N. Ledentsov, D.-J. Kang, and M. G. Blamire, "Transform-limited optical pulses from 18 GHz monolithic modelocked quantum dot lasers operating at 1.3 μm," *Electron. Lett.,* vol. 40, pp. 346-347, 2004.

[26] E. U. Rafailov, M. A. Cataluna, W. Sibbett, N. D. Il'inskaya, Y. M. Zadiranov, A. E. Zhukov, V. M. Ustinov, D. A. Livshits, A. R. Kovsh, and N. N. Ledentsov, "High-power ultrashort pulses output from a mode-locked two-section quantum-dot laser," in Tech. Dig. of CLEO'04, San Francisco, USA, 2004.

[27] E. U. Rafailov, M. A. Cataluna, W. Sibbett, D. A. Livshits, A. R. Kovsh, and N. N. Ledentsov, "Stable modelocked operation from a quantum-dot laser in a broad

temperature range," in Lasers and Electro-Optics (CLEO). Conference on, Baltimore, MD, USA, 2005, pp. 1017-1018.

[28] M. G. Thompson, C. Marinelli, X. Zhao, R. L. Sellin, R. V. Penty, I. H. White, I. N. Kaiander, D. Bimberg, D. J. Kang, and M. Blamire, "20 GHz colliding pulse mode-locking of InGaAs quantum dot lasers," in Lasers and Electro-Optics, 2005. (CLEO). Conference on, Batimore, MD, USA, 2005, pp. 1014-1016.

[29] J. Renaudier, R. Brenot, B. Dagens, F. Lelarge, B. Rousseau, F. Poingt, O. Legouezigou, F. Pommereau, A. Accard, P. Gallion, and G. Duan, "45 GHz self-pulsation with narrow linewidth in quantum dot Fabry-Perot semiconductor lasers at 1.5 μm," *Electron. Lett.,* vol. 41, pp. 1007-1008, 2005.

[30] M. A. Cataluna, E. U. Rafailov, A. D. McRobbie, W. Sibbett, D. A. Livshits, and A. R. Kovsh, "Ground and excited-state modelocking in a two-section quantum-dot laser," in Lasers and Electro-Optics Society, 2005. LEOS 2005. The 18th Annual Meeting of the IEEE, Sydney, Australia, 2005, pp. 870-871.

[31] M. Choi, W. Lee, J. Kim, and P. Delfyett, "Ultrashort, high-power pulse generation from a master oscillator power amplifier based on external cavity mode locking of a quantum-dot two-section diode laser," *Appl. Phys. Lett.,* vol. 87, pp. 221107, 2005.

[32] A. Rae, M. Thompson, R. Penty, I. White, A. Kovsh, S. Mikhrin, D. Livsits, and I. Krestnikov, "Harmonic mode-locking of a quantum-dot laser diode," in Lasers and Electro-Optics Society, 2006. LEOS 2006. 19th Annual Meeting of the IEEE, Montreal, Que., Canada, 2006, pp. 874-875.

[33] M. Choi, J. Kim, W. Lee, and P. J. Delfyett, "Ultralow noise optical pulse generation in an actively mode-locked quantum-dot semiconductor laser," *Appl. Phys. Lett.,* vol. 88, no. 13, pp. 131106, 2006.

[34] A. D. McRobbie, M. A. Cataluna, D. A. Livshits, W. Sibbett, and E. U. Rafailov, "High power all-quantum-dot based external cavity mode-locked laser," in Lasers and Electro-Optics Society, 2006. 19th Annual Meeting of the IEEE, Montreal, Que., Canada, 2006.

[35] A. Martinez, C. Gosset, K. Merghem, F. Lelarge, J. Landreau, G. Aubin, and A. Ramdane, "Sub-picosecond pulse generation at 1.56 μm using a mode-locked quantum dot laser," in Optical Communication, 2005. ECOC 2005. 31st European Conference on, 2005, pp. 169-170.

[36] C. Gosset, K. Merghem, A. Martinez, G. Moreau, G. Patriarche, G. Aubin, J. Landreau, F. Lelarge, and A. Ramdane, "Sub-picosecond pulse generation at 134 GHz using a quantum dash-based Fabry-Perot laser emitting at 1.56 μm," in Optical Fiber Communication Conference, 2006 and the 2006 National Fiber Optic Engineers Conference. OFC 2006, Anaheim, CA, USA, 2006.

[37] L. Drzewietzki, S. Breuer, M. Rossetti, T. Xu, P. Bardella, H. Simos, C. Mesaritakis, M. Ruiz, I. Krestnikov, D. Livshits, M. Krakowski, D. Syvridis, I. Montrosset, E. U. Rafailov, and W. Elsaser, "Picosecond pulse generation with 34W peak power using a monolithic quantum-dot tapered mode-locked laser and tapered optical amplifier," in Lasers and Electro-Optics Europe (CLEO Europe/IQEC), 2013 Conference on and International Quantum Electronics Conference, Munich, 2013, pp. 1.

[38] M. Ruiz, N. Michel, M. Calligaro, Y. Robert, M. Krakowski, D. I. Nikitichev, M. A. Cataluna, D. Livshits, and E. U. Rafailov, "New tapered quantum-dot mode-locked laser diode with high peak power, low divergence and good beam quality," in Semiconductor Laser Conference (ISLC), 2010 22nd IEEE International Kyoto, 2010, pp. 170-171.

[39] Y. Ding, D. I. Nikitichev, I. Krestnikov, D. Livshits, M. A. Cataluna, and E. U. Rafailov, "Quantum-dot external-cavity passively modelocked laser with high peak power and pulse energy," *Electron. Lett.,* vol. 46, pp. 1516-1518, 2010.

[40] A. R. Albrecht, T. J. Rotter, C. P. Hains, A. Stintz, J. V. Moloney, K. J. Malloy, and G. Balakrishnan, "Multi-watt 1.25 μm quantum dot VECSEL," *Electron. Lett.,* vol. 46, no. 12, pp. 856-857, 2010.

[41] D. I. Nikitichev, M. Ruiz, Y. Ding, M. Tran, Y. Robert, M. Krakowski, M. Rossetti, P. Bardella, I. Montrosset, I. Krestnikov, D. Livshits, M. A. Cataluna, and E. U. Rafailov, "Passively mode-locked monolithic two-section gain-guided tapered quantum-dot lasers: II. Record 15 Watt peak power generation," in Lasers and Electro-Optics Europe (CLEO EUROPE/EQEC), 2011 Conference on and 12th European Quantum Electronics Conference Munich, 2011, pp. 1.

[42] C. Mesaritakis, C. Simos, H. Simos, S. Mikroulis, L. Krestnikov, and D. Syvridis, "Pulse width narrowing due to dual ground state emission in quantum dot passively mode locked lasers," *Appl. Phys. Lett.,* vol. 96, pp. 211110, 2010.

[43] R. Rosales, K. Merghem, C. Calo, G. Bouwmans, I. Krestnikov, A. Martinez, and A. Ramdane, "Optical pulse generation in single section InAs/GaAs quantum dot

edge emitting lasers under continuous wave operation ” *Appl. Phys. Lett.,* vol. 101, pp. 221113, 2012.

[44] T. H. Xu, P. Bardella, and I. Montrosset, “Quantum Dot Passively Mode-Locked Laser Optimization for High-Power and Short Pulses,” *IEEE Photon. Technol. Lett.,* vol. 25, no. 1, pp. 63-65, 2013.

[45] P. Finch, P. Blood, P. M. Smowton, A. Sobiesierski, R. M. Gwilliam, and I. O'Driscoll, “Femtosecond pulse generation in passively mode locked InAs quantum dot lasers,” *Appl. Phys. Lett.,* vol. 103, no. 13, pp. 131109, 2013.

[46] R. Raghunathan, M. T. Crowley, F. Grillot, Y. Li, J. K. Mee, V. Kovanis, and L. F. Lester, “Pulse Characterization of Passively Mode-Locked Quantum-Dot Lasers Using a Delay Differential Equation Model Seeded With Measured Parameters,” *IEEE J. Sel. Topics Quantum Electron.,* vol. 19, no. 4, pp. 1100311, 2013.

[47] F. Van Dijk, A. Enard, X. Buet, F. Lelarge, and G. Duan, “Phase Noise Reduction of a Quantum Dash Mode-Locked Laser in a Millimeter-Wave Coupled Opto-Electronic Oscillator,” *J. Lightw. Technol. ,* vol. 26, no. 15, pp. 2789-2794, 2008.

[48] M. G. Thompson, D. Larson, A. R. Rae, and K. Yvind, “Monolithic Hybrid and Passive Mode-Locked 40GHz Quantum Dot Laser Diodes,” in Optical Communications, 2006. ECOC 2006. European Conference, Cannes, France, 2006, pp. 1-2.

[49] G. Carpintero, M. G. Thompson, R. V. Penty, and I. H. White, “Sub-kHz RF electrical linewidth from a 10GHz passively mode-locked quantum-dot laser diode,” in Lasers and Electro-Optics, 2009 and 2009 Conference on Quantum

electronics and Laser Science Conference. CLEO/QELS 2009. Conference on, Baltimore, MD, 2009, pp. 1-2.

[50] T. Habruseva, S. O'Donoghue, N. Rebrova, D. Reid, L. Barry, D. Rachinskii, G. Huyet, and S. Hegarty, "Quantum-dot mode-locked lasers with dual-mode optical injection," *IEEE Photon. Technol. Lett.,* vol. 22, pp. 359-361, 2010.

[51] M. Xia, M. Thompson, R. Penty, and I. White, "External-cavity mode-locked quantum-dot laser diodes for low repetition rate, sub-picosecond pulse generation," *IEEE J. Sel. Topics Quantum Electron.,* vol. 17, pp. 1264-1271, 2011.

[52] K. Merghem, A. Akrout, A. Martinez, F. Lelarge, B. Rousseau, F. Poingt, L. Legouezigou, O. Legouezigou, A. Accard, F. Pommereau, G. H. Duan, G. Aubin, and A. Ramdane, "Subpicosecond pulse generation at 245 GHz using a quantum-dash-based passive mode-locked laser emitting at 1.53 μm," in Lasers and Electro-Optics, 2008 and 2008 Conference on Quantum Electronics and Laser Science. CLEO/QELS 2008. Conference on San Jose, CA, 2008.

[53] Y. Li, M. Breivik, C. Feng, B. Fimland, and L. Lester, "A low repetition rate all-active monolithic passively mode-locked quantum-dot laser," *IEEE Photon. Technol. Lett.,* vol. 23, pp. 1019-1021, 2011.

[54] A. Lagrost, M. CostaeSilva, M. Gay, L. Bramerie, S. LaRochelle, P. Besnard, A. Shen, and G. H. Duan, "Tunable and variable clock generation up to 1.2 THz by filtering an actively mode-locked 42.5 GHz quantum dash fabry-perot laser with a reconfigurable filter," in Optical Fiber Communication (OFC), collocated National Fiber Optic Engineers Conference, 2010 Conference on (OFC/NFOEC) San Diego, CA, 2010, pp. 1-3.

[55] Z. Jiao, J. Liu, Z. Lu, X. Zhang, P. Poole, P. Barrios, and D. Poitras, "A C-Band InAs/InP quantum dot semiconductor mode-locked laser emitting 403-GHz repetition rate pulses," *IEEE Photon. Technol. Lett.,* vol. 23, pp. 543-545, 2011.

[56] M. A. Cataluna, D. I. Nikitchev, I. Krestnikov, D. A. Livshits, A. R. Kovsh, and E. U. Rafailov, "Dual-wavelength mode-locked GaAs-based quantum-dot laser," in Lasers and Electro-Optics 2009 and the European Quantum Electronics Conference. CLEO Europe - EQEC 2009. European Conference on Munich, 2009, pp. 1.

[57] C. Mesaritakis, C. Simos, H. Simos, I. Krestnikov, and D. Syvridis, "Dual ground-state pulse generation from a passively mode-locked InAs/InGaAs quantum dot laser," *Appl. Phys. Lett.,* vol. 99, no. 14, pp. 141109, 2011.

[58] J. Liu, Z. Lu, S. Raymond, P. Poole, P. Barrios, and D. Poitras, "Dual-wavelength 92.5 GHz self mode- locked InP-based quantum dot laser," *Opt. Lett.,* vol. 33, pp. 1702-1704, 2008.

[59] K. Klaime, R. Piron, C. Paranthoen, T. Batte, F. Grillot, O. Dehaese, S. Loualiche, A. Le Corre, R. Rosales, K. Merghem, A. Martinez, and A. Ramdane, "20 GHz to 83 GHz single section InAs/InP quantum dot mode-locked lasers grown on (001) misoriented substrate," in Indium Phosphide and Related Materials (IPRM), 2012 International Conference on Santa Barbara, CA, 2012, pp. 181-184.

[60] M. Radziunas, A. G. Vladimirov, E. A. Viktorov, G. Fiol, H. Schmeckebier, and D. Bimberg, "Strong pulse asymmetry in quantum-dot mode-locked semiconductor lasers," *Appl. Phys. Lett.,* vol. 98, no. 3, pp. 031104, 2011.

[61] M. Rossetti, P. Bardella, and I. Montrosset, "Time-domain travellingwave model for quantum dot passively mode-locked lasers," *IEEE J. Quantum Electron.,* vol. 47, pp. 139-150, 2011.

[62] H. Simos, C. Simos, C. Mesaritakis, and D. Syvridis, "Two-section quantum-dot mode-locked lasers under optical feedback: Pulse broadening and harmonic operation," *IEEE J. Quantum Electron.,* vol. 47, no. 10, pp. 1320-1329, 2012.

[63] C. Mesaritakis, C. Simos, H. Simos, A. Kapsalis, E. Roditi, I. Krestnikov, and D. Syvridis, "Effect of the number of quantum dot layers and dual state emission on the performance of InAs/InGaAs passively mode-locked lasers," *Appl. Phys. Lett.,* vol. 101, no. 25, pp. 251115, 2012.

[64] J. K. Mee, M. Crowley, D. Murrell, R. Raghunathan, and L. F. Lester, "Temperature Performance of Monolithic Passively Mode-Locked Quantum Dot Lasers: Experiments and Analytical Modeling," *IEEE J. Sel. Topics Quantum Electron.,* vol. 19, no. 4, pp. 1101110, 2013.

[65] S. Koenig, D. Lopez-Diaz, J. Antes, F. Boes, R. Henneberger, A. Leuther, A. Tessmann, R. Schmogrow, D. Hillerkuss, R. Palmer, T. Zwick, C. Koos, W. Freude, O. Ambacher, J. Leuthold, and I. Kallfass, "Wireless sub-THz communication system with high data rate," *Nature Photon.,* vol. 7, pp. 977-981, 2013.

[66] S. J. B. Yoo, "Flexible Bandwidth Terabit Coherent Optical Communication Networks by Optical Arbitrary Waveform Generation and Measurement," *IEEE Photonics Society Newsletter,* vol. 25, no. 5, pp. 5-12, 2011.

[67] G. C. Valley, "Photonic analog-to-digital converters," *Opt. Exp.,* vol. 15, no. 5, pp. 1955-1982, 2007.

[68] Z. Lu, J. Liu, S. Raymond, P. Poole, P. Barrios, and D. Poitras, "312-fs pulse generation from a passive C-band InAs/InP quantum dot mode-locked laser," *Opt. Exp.,* vol. 16, pp. 10835-10840, 2008.

[69] Z. Lu, J. Liu, P. Poole, S. Raymond, P. Barrios, D. Poitras, G. Pakulski, P. Grant, and D. Roy-Guay, "An L-band monolithic InAs/InP quantum dot mode-locked laser with femtosecond pulses," *Opt. Exp.,* vol. 17, pp. 13609-13614, 2009.

[70] K. Merghem, A. Akrout, A. Martinez, G. Aubin, and A. Ramdane, "Pulse generation at 346 GHz using a passively mode locked quantum-dash based laser at 1.55 μm," *Appl. Phys. Lett.,* vol. 94, pp. 021107, 2009.

[71] R. Rosales, K. Merghem, A. Martinez, A. Akrout, J. P. Tourrenc, A. Accard, F. Lelarge, and A. Ramdane, "InAs/InP quantum-dot passively mode-locked lasers for 1.55-μm applicatons," *IEEE J. Sel. Topics Quantum Electron.,* vol. 17, no. 5, pp. 1292-1301, 2011.

[72] Z. Lu, J. Liu, P. Poole, Z. Jiao, P. Barrios, D. Poitras, J. Caballero, and X. P. Zhang, "Ultrahigh repetition rate InAs/InP quantum dot mode-locked lasers," *Opt. Commun.,* vol. 284, no. 9, pp. 2323-2326, 2011.

[73] K. Klaime, C. Calò, R. Piron, C. Paranthoen, D. Thiam, T. Batte, O. Dehaese, J. L. Pouliquen, S. Loualiche, A. L. Corre, K. Merghem, and A. M. Ramdane, "23 and 39 GHz low phase noise monosection InAs/InP (113)B quantum dots mode-locked lasers," *Opt. Exp.,* vol. 21, no. 23, pp. 29000-29005, 2013.

[74] R. Rosales, S. G. Murdoch, R. T. Watts, K. Merghem, A. Martinez, F. Lelarge, A. Accard, L. P. Barry, and A. Ramdane, "High performance mode locking characteristics of single section quantum dash lasers," *Opt. Exp.,* vol. 20, no. 8, pp. 8649-8657, 2012.

[75] C. Calò, H. Schmeckebier, K. Merghem, R. Rosales, F. Lelarge, A. Martinez, D. Bimberg, and A. Ramdane, "Frequency resolved optical gating characterization of sub-ps pulses from single-section InAs/InP quantum dash based mode-locked lasers," *Opt. Exp.,* vol. 22, no. 2, pp. 1742-1748, 2014.

[76] A. Akrout, K. Merghem, J. P. Tourrenc, A. Martinez, A. Shen, F. Lelarge, G. H. Duan, and A. Ramdane, "Generation of 10 GHz optical pulses with very low timing jitter using one section passively mode locked quantum dash based lasers operating at 1.55 μm," in Optical Fiber Communication-includes post deadline papers, 2009. OFC 2009. Conference on, San Diego, CA, USA, 2009, pp. 1-3.

[77] Y. Wang, Y. Mao, Y. Chen, X. Wang, and H. Su, "Random population model for self pulsation in single-section quantm-dot lasers," *IEEE Photon. Technol. Lett.,* vol. 25, pp. 389-392, 2013.

[78] D. Mowbray, and M. Solnick, "New physics and devices based on self-assembled semiconductor quantum dots," *J. Phys. D: Appl. Phys.,* vol. 38, pp. 2059-2076, 2005.

[79] B. W. Hakki, and T. L. Paoli, "Gain spectra in GaAs double-hetereojunction injection lasers," *J. Appl. Phys.,* vol. 46, pp. 1299-1306, 1975.

[80] A. Ukhanov, A. Stintz, P. Eliseev, and K. Malloy, "Comparison of the carrier induced refractive index, gain, and linewidth enhancement factor in quantum dot and quantum well lasers," *Appl. Phys. Lett.,* vol. 84, pp. 1058-1060, 2004.

[81] M. Willatzen, D. Horsholm, T. Tanaka, Y. Arakawa, and J. Singh, "Polarization dependence of optoelectronic properties in quantum dots and quantum wires-consequences of valence-band mixing," *IEEE J. Quantum Electron.,* vol. 30, pp. 640-653, 1994.

[82] T. Newell, D. Bossert, A. Stintz, B. Fuchs, K. Malloy, and L. Lester, "Gain and linewidth enhancement factor in InAs quantum-dot laser diodes," *IEEE Photon. Technol. Lett.,* vol. 11, pp. 1527-1529, 1999.

[83] E. Rafailov, M. Cataluna, and W. sibbett, "Mode-locked quantum-dot lasers," *Nature Photon.,* vol. 1, pp. 395-401, 2007.

[84] Z. Lu, J. Liu, S. Raymond, P. Poole, P. Barrios, G. Pakulski, D. Poitras, F. Sun, S. Taebi, and T. Hall, "Ultra-broadband quantum-dot semiconductor optical amplifier and its applications," in Optical Fiber Communication Conference and the National Fiber Optic Engineers Conference, 2007. OFC/NFOEC 2007. Conference on, Ananeim, CA, USA, 2007.

[85] K. Mukai, N. Ohtsuka, H. Shoji, and M. Sugawara, "Phonon bottleneck in self-formed $In_xGa_{1-x}As$/GaAs quantum dots by electroluminescence and time-resolved photoluminescence," *Phys. Rev. B,* vol. 54, pp. R5243-R5246, 1996.

[86] E. U. Rafailov, S. J. Whit, A. A. Lagatsky, A. Miller, W. Sibbett, D. A. Livshits, A. E. Zhukov, and V. M. Ustinov, "Fast quantum-dot saturable absorber for

passive mode-locking of solid-state lasers," *IEEE Photon. Technol. Lett.,* vol. 16, pp. 2439-2441, 2004.

[87] P. Borri, W. Langbein, J. Hvam, F. Heinrichsdor, M. H. Mao, and D. Bimberg, "Spectral hole-burning and carrier-heating dynamics in InGaAs quantum-dot amplifiers," *IEEE J. Sel. Topics Quantum Electron.,* vol. 6, no. 3, pp. 544-551, 2000.

[88] D. B. Malins, A. Gomez-lglesias, S. J. White, W. Sibbett, A. Miller, and E. U. Rafailov, "Ultrafast electroabsorption dynamics in an InAs quantum dot saturable absorber at 1.3 μm," *Appl. Phys. Lett.,* vol. 89, pp. 171111, 2006.

[89] P. Borri, W. Langbein, J. M. Hvam, F. Heinrichsdorff, M. H. Mao, and D. Bimberg, "Ultrafast gain dynamics in InAs-InGaAs quantum-dot amplifiers," *IEEE Photon. Technol. Lett.,* vol. 12, no. 6, pp. 594-596, 2002.

[90] D. F. Geraghty, R. B. Lee, M. Verdiell, M. Ziari, A. Mathur, and K. J. Vahala, "Wavelength conversion for WDM communication systems using four-wave mixing in semiconductor optical amplifiers," *IEEE J. Sel. Topics Quantum Electron.,* vol. 3, no. 5, pp. 1146-1155, 1997.

[91] Z. Lu, J. Liu, S. Raymond, P. Poole, P. Barrios, D. Poitras, F. Sun, G. Pakkulski, P. Bock, and T. Hall, "Highly efficient non-degenerate four-wave mixing process in InAs/InGaAsP quantum dots," *Electron. Lett.,* vol. 42, pp. 1112-1113, 2006.

[92] T. Akiyama, H. Kuwatsuka, N. Hatori, Y. Nakata, H. Ebe, and M. Sugawara, "Symmetric highly efficient (~0 dB) wavelength conversion based on four-wave mixing in quantum dot optical amplifiers," *IEEE Photon. Technol. Lett.,* vol. 14, pp. 1139-1141, 2002.

[93] A. Bilenca, R. Alizon, V. Mikhelashvili, G. Eisenstein, R. Schwertberger, D. Gold, J. Reithmaier, and A. Forchel, "InAs/InP 1550 nm quantum dash semiconductor optical amplifiers," *Electron. Lett.,* vol. 38, pp. 1350-1351, 2002.

[94] F. Lelarge, B. Dagens, J. Reaudier, R. Brenot, A. Accard, F. Dijk, D. Make, O. Gouezigou, J. Provost, F. Poingt, J. Landreau, O. Drisse, E. Derouin, B. Rousseau, F. Pommereau, and G. Duan, "Recent advances on InAs/InP quantum dash based semiconductor lasers and optical amplifiers operating at 1.55 μm," *IEEE J. Sel. Topics Quantum Electron.,* vol. 13, pp. 111-124, 2007.

[95] R.H.Wang, A. Stintz, P. M.Varangis, T. C. Newell, H. Li, K. J.Malloy, and L. F. Lester, "Room-temperature operation of InAs quantum-dash lasers on InP [001]," *IEEE Photon. Technol. Lett.,* vol. 13, pp. 767-769, 2001.

[96] G. H. Duan, A. Shen, A. Akrout, F. V. Dijk, F. Lelarge, F. Pommereau, O. LeGouezigou, J. Provost, H. Gariah, F. Blache, F. Mallecot, K. Merghem, A. Martinez, and A. Ramdane, "High performance InP-based quantum dash semiconductor mode-locked lasers for optical communications," *Bell Labs Technical Journal,* vol. 14, pp. 63-84, 2009.

[97] G. Liu, A. Stintz, H. Li, T. Newell, A. Gray, P. Varangis, K. Malloy, and L. Lester, "The influence of quantum-well composition on the performance of quantum dot lasers using InAs/InGaAs dots-in-a-well (DWELL) structures," *IEEE J. Quantum Electron.,* vol. 36, pp. 1272-1279, 2000.

[98] S. Cortez, O. Krebs, and P. Voisin, "Polarization of the interband optical dipole in InAs/GaAs self-organized quantum dots," *Phys. Rev. B,* vol. 63, pp. 233306, 2001.

[99] K. Silverman, R. Mirin, S. Cundiff, and A. Norman, "Direct measurement of polarization resolved transition dipole moment in InGaAs/GaAs quantum dots," *Appl. Phys. Lett.,* vol. 82, pp. 4552-4554, 2003.

[100] O. Qasaimeh, "Effect of inhomogeneous line broadening on gain and differential gain of quantum dot lasers," *IEEE Transactions on Electron Devices,* vol. 50, pp. 1575-1581, 2003.

[101] A. Sakamoto, and M. Sugawara, "Theoretical calculation of lasing spectra of quantum-dot lasers: effect of homogeneous broadening of optical gain," *IEEE Photon. Technol. Lett.,* vol. 12, pp. 107-109, 2000.

[102] M. Sugawara, K. Mukai, Y. Nakata, H. Ishikawa, and A. Sakamoto, "Effect of homogeneous broadening of optical gain on lasing spectra in self-assembled $In_xGa_{1-x}As$/GaAs quantum dot lasers," *Phys. Rev. B,* vol. 61, pp. 7595-7603, 2000.

[103] M. Gioannini, and I. Montrosset, "Numerical analysis of the frequency chirp in quantum-dot semiconductor lasers," *IEEE J. Quantum Electron.,* vol. 43, pp. 941-949, 2007.

[104] M. Sugawara, T. Akiyama, N. Hatori, Y. Nakata, H. Ebe, and H. Ishikawa, "Quantum-dot semiconductor optical amplifiers for high-bit-rate signal processing up to 160 Gb s^{-1} and a new scheme of 3R regenerators," *Measurement Science and Technology,* vol. 13, no. 11, pp. 1683-1691, 2002.

[105] L. Coldren, and S. Corzine, *Diode lasers and photonic integrated circuits*: Wiley, 1995.

[106] T. W. Berg, S. Bischoff, I. Magnusdottir, and J. Mork, "Ultrafast gain recovery and modulation limitations in self-assembled quantum-dot devices," *IEEE Photon. Technol. Lett.,* vol. 13, pp. 541-543, 2001.

[107] A. Vladimirov, and D. Turaev, "Model for mode locking in semiconductor lasers," *Phys. Rev. A,* vol. 72, pp. 033808, 2005.

[108] E. Viktorov, P. Mandel, A. Vladimirov, and U. Bandelow, "Model for mode locking in quantum dot lasers," *Appl. Phys. Lett.,* vol. 88, pp. 201102, 2006.

[109] M. Rossetti, P. Bardella, and I. Montrosset, "Modeling passive mode-locking in quantum dot lasers: a comparison between a finite difference travelling wave model and a delayed differential equation approach," *IEEE J. Quantum Electron.,* vol. 47, pp. 569-576, 2011.

[110] M. Cataluna, W. Sibbet, D. Livshits, J. Weimert, A. Kovsh, and E. Rafailov, "Stable mode locking via ground- or excited-state transitions in a two-section quantum-dot laser," *Appl. Phys. Lett.,* vol. 89, pp. 081124, 2006.

[111] Y. Kim, Y. Joshi, and A. Fedorov, "Thermally dependent characteristics and spectral hold burning of the double-lasing, edge-emitting quantum-dot laser," *J. Appl. Phys.,* vol. 107, pp. 073104, 2010.

[112] E. Viktorov, P. Mandel, Y. Tanguy, J. Houlihan, and G. Huyet, "Electron-hole asymmetry and two-state lasing in quantum dot lasers," *Appl. Phys. Lett.,* vol. 87, pp. 053113, 2005.

[113] V. Korenev, A. Savelyev, A. Zhukov, A. Omelchenko, and M. Maximov, "Analytical approach to the multi-state lasing phenomenon in quantum dot lasers," *Appl. Phys. Lett.,* vol. 102, pp. 112101, 2013.

[114] J. Kim, M. Choi, and P. Delfyett, "Pulse generation and compression via ground and excited states from a grating coupled passively mode-locked quantum dot two-section diode laser," *Appl. Phys. Lett.,* vol. 89, pp. 261106, 2006.

[115] E. Rafailov, M. Cataluna, W. Sibbett, N. Il'inskaya, Y. Zadiranov, A. Zhukov, V. Ustinov, D. Livshits, A. Kovsh, and N. Ledentsove, "High-power picosecond and femtosecond pulse generation from a two-section mode-locked quantum-dot laser," *Appl. Phys. Lett.,* vol. 87, pp. 081107, 2005.

[116] M. G. Thompson, A. R. Rae, M. Xia, R. V. Penty, and I. H. White, "InGaAs quantum-dot mode-locked laser diodes," *IEEE J. Sel. Topics Quantum Electron.,* vol. 15, pp. 661-672, 2009.

[117] A. Gubenko, D. Livshits, I. Krestnikov, S. Mikhrin, A. Kozhukhov, A. Kovsh, N. Ledentsov, A. Zhukov, and E. Portnoi, "High-power monolithic passively modelocked quantum-dot laser," *Electron. Lett.,* vol. 41, pp. 1124-1125, 2005.

[118] A. Akrout, A. Shen, F. Lelarge, F. Pommereau, H. Gariah, F. Blache, G. Duan, and A. Ramdane, "Spectrum filtering and pulse compression of quantum-dash mode-locked lasers emitting at 1.55 μm," in Optical Communication, 2008. ECOC 2008. 34th European Conference on, Brussels, Belgium, 2008, pp. 1-2.

[119] A. McRobbie, M. Cataluna, S. Zolotovskaya, D. Livshits, W. Sibbett, and E. Rafailov, "High power all-quantum-dot-based external cavity modelocked laser," *Electron. Lett.,* vol. 43, pp. 812-813, 2007.

[120] Y. Ding, M. Cataluna, D. Nikitichev, L. Krestnikov, D. Livshits, and E. Rafailov, "Broad repetition-rate tunable quantum-dot external-cavity passively mode-

locked laser with extremely narrow radio frequency linewidth," *Appl. Phys. Exp.,* vol. 4, pp. 062703, 2011.

[121] M. Thompson, C. Marinelli, X. Zhao, R. Sellin, R. Penty, I. White, I. Kaiander, D. Bimberg, D. Kang, and M. Blamire, "Colliding-pulse modelocked quantum dot lasers," *Electron. Lett.,* vol. 41, pp. 248-249, 2005.

[122] Z. Jiao, J. Liu, Z. Lu, P. Poole, P. Barrios, D. Poitras, and X. Zhang, "437 GHz Optical Pulse Train Generation from a C-Band InAs/InP Quantum Dot Laser," in Optical Fiber Communication Conference and Exposition (OFC/NFOEC), 2011 and the National Fiber Optic Engineers Conference, Los Angeles, CA, USA, 2011, pp. 1-3.

[123] J. Liu, Z. Lu, P. Poole, P. Barrios, D. Poitras, Z. Jiao, and X. Zhang, "THz optical pulses from a coupled-cavity quantum-dot laser," *Opt. Commun.,* vol. 285, pp. 1323-1325, 2012.

[124] T. Habruseva, G. Huyet, and S. Hegarty, "Dynamics of quantum-dot mode-locked lasers with optical injection," *IEEE J. Sel. Topics Quantum Electron.,* vol. 17, pp. 1272-1279, 2011.

[125] J. Kim, A. Ardey, and P. Delfyett, "Coherent spectral bandwidth combing by optical pulse injection locking in quantum dot mode locked semiconductor diode lasers," *Electron. Lett.,* vol. 48, pp. 720-721, 2012.

[126] C. Lin, F. Grillot, N. Naderi, Y. Li, and L. Lester, "RF linewidth reduction in a quantum dot passively mode-locked laser subject to external optical feedback," *Appl. Phys. Lett.,* vol. 96, pp. 051118, 2010.

[127] K. Merghem, R. Rosales, S. Azouigui, A. Akrout, A. Martinez, F. Lelarge, G. Duan, G. Aubin, and A. Ramdane, "Low noise performance of passively mode locked quantum-dash-based lasers under external optical feedback," *Appl. Phys. Lett.,* vol. 95, pp. 131111, 2009.

[128] S. Breuer, W. Elasser, J. G. McInerney, K. Yvind, J. Pozo, E. A. J. M. Bente, M. Yousefi, A. Villafranca, N. Vogiatzis, and J. Rorison, "Investigations of Repetition Rate Stability of a Mode-Locked Quantum Dot Semiconductor Laser in an Auxiliary Optical Fiber Cavity," *IEEE J. Quantum Electron.,* vol. 46, pp. 150-157, 2010.

[129] C. Ribbat, R. Sellin, I. Kaiander, F. Hopfer, N. Ledentsov, D. Bimberg, A. Kovsh, V. stinov, A. Zhukov, and M. Maximov, "Complete suppression of filamentation and superior beam quality in quantum-dot lasers," *Appl. Phys. Exp.,* vol. 82, pp. 952-954, 2003.

[130] D. O'Brien, S. Hegarty, G. Huyet, J. McInerney, T. Kettler, M. Laemmlin, D. Bimberg, V. Ustinov, A. Zhukov, S. Mikhrin, and A. Kovsh, "Feedback sensitivity of 1.3 μm InAs/GaAs quantum dot lasers," *Electron. Lett.,* vol. 41, pp. 244-245, 2005.

[131] G. Liu, X. Jin, and S. Chuang, "Measurement of linewidth enhancement factor of semiconductor lasers using an injection-locking technique," *IEEE Photon. Technol. Lett.,* vol. 470-473, 2001.

[132] K. Kim, I. Han, Y. Yoo, J. Lee, Y. Sung, and T. Kim, "Optical characteristics and the linewidth enhancement factor measured from InAs/GaAs quantum dot laser diodes," *IEEE Photon. Technol. Lett.,* vol. 7, pp. 135-137, 2008.

[133] S. Schneider, P. Borri, W. Langbein, U. Woggon, R. L. Sellin, D. Ouyang, and D. Bimberg, "Linewidth enhancement factor in InAs quantum-dot amplifiers," *IEEE J. Quantum Electron.,* vol. 40, pp. 1423-1429, 2004.

[134] J. R. Liu, Z. G. Lu, S. Raymond, P. J. Poole, P. J. Barrios, and D. Poitras, "1.6-μm multiwavelength emission of an InAs-InGaAsP quantum-dot laser," *IEEE Photon. Technol. Lett.,* vol. 20, pp. 81-83, 2008.

[135] G. Ortner, C. N. Allen, C. Dion, P. Barrios, D. Poitras, D. Dalacu, G. Pakulski, J. Lapointe, P. J. Poole, W. Render, and S. Raymond, "External cavity InAs/InP quantum dot laser with a tuning range of 166 nm," *Appl. Phys. Lett.,* vol. 88, pp. 121119, 2006.

[136] F. Grillot, A. Martinez, K. Merghem, J. Provost, F. Alexandre, R. Piron, O. Dehaese, S. Loualiche, L. Lester, and A. Ramdane, "Stable above-threshold linewidth enhancement factor in a 1.52-μm InAs/InP (311B) quantum dot laser," in IEEE Lasers and Electro-Optics Society, 2008. LEOS 2008. 21st Annual Metting of the Acapulco, 2008, pp. 535-536.

[137] F. Lelarge, B. Rousseau, B. Dagens, F. Poingt, F. Pommereau, and A. Accard, "Room temperature continuous-wave operation of buried ridge stripe lasers using InAs-InP (100) quantum dots as active core," *IEEE Photon. Technol. Lett.,* vol. 17, pp. 1369-1371, 2005.

[138] Z. G. Lu, P. J. Poole, J. R. Liu, P. J. Barrior, Z. J. Jiao, G. Pakulski, D. Poitras, D. Goodchild, B. Rioux, and A. J. SpringThorpe, "High performance 1.52 μm InAs/InP quantum dot distributed feedback laser," *Electron. Lett.,* vol. 47, pp. 818-819, 2011.

[139] Z. G. Lu, J. R. Liu, P. J. Poole, S. Raymond, P. J. Barrios, D. Poitras, G. Pakulski, X. P. Zhang, K. Hinzer, and T. J. Hall, "Low noise InAs/InP quantum dot C-band monolithic multiwavelength lasers for WDM-PONs," in Optical Fiber Communicaion-includes post deadline papers, 2009. OFC. Conference on, San Diego, CA, USA, 2009, pp. 1-3.

[140] S. Azouigui, B. Dagens, F. Lelarge, J. G. Provost, D. Make, O. L. Gouezigou, A. Accard, A. Martinez, K. Merghem, F. Grillot, O. Dehaese, R. Piron, S. Loualiche, Q. Zou, and A. Ramdane, "Optical feedback tolerance of quantum-dot- and quantumd-dash-based semiconductor lasers operating at 1.55 μm," *IEEE J. Sel. Topics Quantum Electron.,* vol. 15, pp. 764-773, 2009.

[141] H. Schmeckebier, G. Fiol, C. Meuer, D. Arsenijevic, and D. Bimberg, "Complete pulse charaterization of quantum-dot mode-locked lasers suitable for optical communication up to 160 Gbit/s," *Opt. Exp.,* vol. 18, pp. 3415-3425, 2010.

[142] P. Poole, K. Kaminska, P. Barrios, Z. Lu, and J. Liu, "Growth of InAs/InP-based quantum dots for 1.55 μm laser applications," *J. Cryst. Growth,* vol. 311, pp. 1482-1486, 2009.

[143] I. Petitbon, P. Gallion, G. Debarge, and C. Chabran, "Locking bandwidth and relaxation oscillations of an injection-locked semiconductor laser," *IEEE J. Quantum Electron.,* vol. 24, pp. 148-154, 1988.

[144] A. Martinez, A. Lemaître, K. Merghem, L. Ferlazzo, C. Dupuis, A. Ramdane, J. G. Provost, B. Dagens, O. L. Gouezigou, and O. Gauthier-Lafaye, "Static and dynamic measurements of the α-factor of five-quantum-dot-layer single-mode lasers emitting at 1.3μm on GaAs," *Appl. Phys. Lett.,* vol. 86, pp. 211115, 2005.

[145] S. Melnik, and G. Huyet, "The linewidth enhancement factor α of quantum dot semiconductor lasers," *Opt. Exp.,* vol. 14, pp. 2950-2955, 2006.

[146] S. Breuer, M. Rossetti, L. Drzewietzki, P. Bardella, I. Montrosset, and W. Elsasser, "Joint experimental and theoretical investigations of twostate mode locking in a strongly chirped reverse-biased monolithic quantum dot laser," *IEEE J. Quantum Electron.,* vol. 47, no. 10, pp. 1320-1329, 2011.

[147] R. Paiella, F. Capasso, C. Gmachl, D. L. Sivco, J. N. Baillargeon, A. L. Hutchinson, A. Y. Cho, and H. C. Liu, "Self-mode-locking of quantum cascade lasers with giant ultrafast optical nonlinearities," *Science,* vol. 290, pp. 1739-1742, 2000.

[148] A. Zilkie, "High-speed properties of 1.55-μm-wavelength quantum dot semiconductor amplifiers and comparison with higher-dimensional structures," dissertation, Dept. Electr. Comput. Eng., Toronto Univ., Toronto, ON, Canada, 2008.

[149] G. Agrawal, *Nonlinear Fiber Optics*, 3rd ed., New York, NY, USA: Academic, 2001.

[150] C. Gosset, K. Merghem, A. Martinez, G. Moreau, G. Patriarche, G. Aubin, A. Ramdane, J. Landreau, and F. Lelarge, "Sub-picosecond pulse generation at 134 GHz using a quantum-dash-based Fabry-Perot laser emitting at 1.56μm," *Appl. Phys. Lett.,* vol. 88, pp. 241105, 2006.

[151] S. Sauvage, P. Boucaud, F. Glotin, R. Prazeres, J. M. Ortega, A. Lemaitre, J. M. Gerard, and V. Thierry-Mieg, "Third-harmonic generaton in InAs/GaAs self-assembled quantum dots," *Phys. Rev. B,* vol. 59, no. 15, pp. 9830-9833, 1999.

[152] D. Nielsen, S. Chuang, N. J. Kim, D. Lee, S. H. Phyn, W. G. Jeong, C. Y. Chen, and T. S. Lay, "Comparison of four-wave mixing in quantum dots and quantum wells for wavelength conversion," in Lasers and Electro-Optics, 2008 and 2008 Conference on Quantum Electronics and Laser Science. CLEO/QELS 2008. Conference on San Jose, CA, 2008, pp. 1-2.

[153] D. Nielsen, S. L. Chuang, N. J. Kim, D. Lee, S. H. Pyun, W. G. Jeong, C. Y. Chen, and T. S. Lay, "High-speed wavelength conversion in quantum dot and quantum well semiconductor optical amplifiers," *Appl. Phys. Lett.,* vol. 92, pp. 211101, 2008.

[154] A. Hugi, G. Villares, S. Blaser, H. C. Liu, and J. Faist, "Mid-infrared frequency comb based on a quantum cascade laser," *Nature,* vol. 492, pp. 229-232, 2012.

[155] P. Friedli, H. Sigg, B. Hinkov, A. Hugi, S. Riedi, M. Beck, and J. Faist, "Four-wave mixing in a quantum cascade laser amplifier," *Appl. Phys. Lett.,* vol. 102, pp. 222104, 2013.

[156] T. Xu, M. Rossetti, P. Bardella, and I. Montrosset, "Simulation and analysis of dynamic regimes involving ground and excited state transitions in quantum dot passively mode-locked lasers," *IEEE J. Quantum Electron.,* vol. 48, no. 9, pp. 1193-1202, 2012.

[157] G. Agrawal, "Population pulsations and nondegenerate four-wave mixing in semiconductor laser and amplifiers," *J. Opt. Soc. Amer. B,* vol. 5, no. 1, pp. 147-159, 1988.

[158] X. Jia, Z. Wu, and G. Xia, "Detailed theoretical investigation on enhanced nondegenerate four-wave mixing in passive mode-locked semiconductor lasers " *IEEE J. Quantum Electron.,* vol. 43, no. 11, pp. 1065-1073, 2007.

[159] H. Simos, M. Rossetti, C. Simos, C. Mesaritakis, T. Xu, P. Bardella, I. Montrosset, and D. Syvridis, "Numerical analysis of passively mode-locked quantum-dot lasers with absorber section at the low-reflectivity output facet," *IEEE J. Quantum Electron.,* vol. 49, pp. 3-10, 2013.

[160] K. L. Hall, G. Lenz, A. M. Darwish, and E. P. Ippen, "Subpicosecond gain and index nonlinearities in InGaAsP diode lasers," *Opt. Commun.,* vol. 111, pp. 589-612, 1994.

[161] M. Hong, Y. Chang, A. Dienes, J. Heritage, P. Delfyett, S. Dijaili, and F. Patterson, "Femtosecond self- and cross-phase modulation in semiconductor laser amplifiers," *IEEE J. Sel. Topics Quantum Electron.,* vol. 2, no. 3, pp. 523-539, 1996.

[162] J. Mork, and J. Mark, "Carrier heating in InGaAsP laser amplifiers due to two-photon absorption," *Appl. Phys. Lett.,* vol. 64, pp. 2206-2208, 1994.

[163] M. Hyodo, K. Abedin, and N. Onodera, "Fourier synthesis of 1.8-THz optical-pulse trains by phase locking of three independent semiconductor lasers," *Opt. Lett.,* vol. 26, pp. 340-342, 2001.

[164] S. Zaitsu, C. Eshima, and K. Ihara, "Generation of a continuous-wave pulse train at a repetition rate of 17.6 THz," *J. Opt. Soc. Amer. B,* vol. 24, pp. 1037-1041, 2007.

[165] S. Osborne, S. O'Brien, E. O'Reilly, P. Huggard, and B. Ellision, "Generation of CW 0.5 THz radiation by photomixing the output of a twocolor 1.49 m Fabry-Perot diode laser," *Electron. Lett.,* vol. 44, pp. 296-297, 2008.

[166] J. Schröder, S. Coen, and F. Vanholsbeeck, "Passively mode-locked Raman fiber laser with 100 GHz repetition rate," *Opt. Lett.,* vol. 31, pp. 3489-3491, 2006.

[167] D. Nielsen, and S. Chuang, "Four-wave mixing and wavelength conversion in quantum dots," *Phys. Rev. B,* vol. 81, pp. 035305, 2010.

[168] R. M. Oldenbeuving, C. J. Lee, P. D. V. Voorst, H. L. Offerhaus, and K.-J. Boller, "Modeling of mode locking in a laser with spatially separate gain media," *Opt. Exp.,* vol. 18, no. 22, pp. 22996-23008, 2010.

[169] K. McIntosh, E. Brown, K. Nichols, O. McMahon, W. DiNatale, and T. Lyszczarz, "Terahertz photomixing with diode lasers in low-temperature grown GaAs," *Appl. Phys. Lett.,* vol. 67, no. 26, pp. 3844-3846, 1995.

[170] N. Onodera, "THz optical beat frequency generation by modelocked semiconductor lasers," *Electron. Lett.,* vol. 32, no. 11, pp. 1013-1014, 1996.

[171] T. Hidaka, S. Matsuura, M. Tani, and K. Sakai, "CW terahertz wave generation by photomixing using a two-longitudinal-mode laser diode," *Electron. Lett.,* vol. 33, no. 24, pp. 2039-2040, 1997.

[172] Y. Matsui, M. Pelusi, S. Arahira, and Y. Ogawa, "Beat frequency generation up to 3.4 THz from simultaneous two-mode lasing operation of sampled-grating DBR laser," *Electron. Lett.,* vol. 35, no. 6, pp. 472-474, 1999.

[173] M. Pelusi, H. Liu, and D. Novak, "THz optical beat frequency generation from a single mode locked semiconductor laser," *Appl. Phys. Lett.,* vol. 71, no. 4, pp. 449-451, 1997.

[174] S. Anzai, Y. Komai, M. Mieno, N. Wada, T. Yoda, T. Miyazaki, and K. Kodate, "Terahertz optical clock generation with tunable repetition rate and central wavelength using variable-bandwidth spectrum shaper," *Opt. Exp.,* vol. 17, no. 7, 2009.

[175] S. Hoffmann, M. Hofmann, E. Bründermann, M. Havenith, M. Matus, J. V. Moloney, A. S. Moskalenko, M. Kira, S. W. Koch, S. Saito, and K. Sakai, "Four-wave mixing and direct terahertz emission with two-color semiconductor lasers," *Appl. Phys. Lett.,* vol. 84, no. 18, pp. 3585-3587, 2004.

[176] S. Hoffmann, M. Hofmann, M. Kira, and S. W. Koch, "Two-colour diode lasers for generation of THz radiation," *Semicond. Sci. Technol.,* vol. 20, no. 7, pp. S205-S210, 2005.

[177] C. Wang, and C. Pan, "Tunable multiterahertz beat signal generation from a two-wavelength laser-diode array," *Opt. Lett.,* vol. 20, no. 11, pp. 1292-1294, 1995.

[178] N. A. Naderi, F. Grillot, K. Yang, J. B. Wright, A. Gin, and L. F. Luke, "Two-color multi-section quantum dot distributed feedback laser," *Opt. Exp.,* vol. 18, no. 26, pp. 27028-27035, 2010.

[179] S. Latkowski, F. Surre, R. Maldonado-Basilio, and P. Landais, "Investigation on the origin of terahertz waves generated by dc-biased multimode semiconductor lasers at room temperature," *Appl. Phys. Lett.,* vol. 93, no. 24, pp. 241110, 2008.

[180] S. Arahira, S. Oshiba, Y. Matsui, T. Kunii, and Y. Ogawa, “Terahertz-rate optical pulse generation from a passively mode-locked semiconductor laser diode,” *Opt. Lett.,* vol. 19, no. 11, pp. 834-836, 1994.

Publications

[1] **Zhejing Jiao**, Rong Zhang, Xiupu Zhang, Jiaren Liu and Zhenguo Lu, "Modeling of single-section quantum dot mode-locked lasers: impact of group velocity dispersion and self-phase modulation," *IEEE J. Quantum Electron.*, vol. 49, pp. 1008-1015, 2013.

[2] **Zhejing Jiao**, Z.G. Lu, J.R. Liu, P.J. Poole, P.J. Barrios, D. Poitras, G. Pakulski, J. Caballero, X.P. Zhang, "Linewidth enhancement factor of InAs/InP quantum dot lasers around 1.5μm," *Opt. Commun.*, vol. 285, pp. 4372-4375, 2012.

[3] **Zhejing Jiao**, Jiaren Liu, Zhenguo Lu, Xiupu Zhang, Philip J. Poole, Pedro J. Barrios, Daniel Poitras, and Juan Caballero, "Tunable terahertz beat signal generation from an InAs/InPquantum dot mode-locked laser combined with external-cavity," *IEEE Photon. Technol. Lett.*, vol. 24, pp. 518-520, 2012.

[4] **Zhejing Jiao**, JiarenLiu, Zhenguo Lu, Xiupu Zhang, Philip J. Poole, Pedro J. Barrios, and Daniel Poitras, "A C-Band InAs/InP quantum dot semiconductor mode-locked laser emitting 403-GHz repetition rate pulses," *IEEE Photon. Technol. Lett.*, vol. 23, pp. 543-545, 2011.

[5] **Z.J. Jiao**, J.R. Liu, Z.G. Lu, P. J. Poole, P. J. Barrios, D. Poitras, and X.P. Zhang, "437 GHz optical pulse train generation from a C-Band InAs/InP quantum dot laser," the Proceeding of Optical Fiber Communications (OFC) 2011, Los Angeles, CA, USA, OThY7, 6-10 March 2011.

[6] **Z.J. Jiao**, Z.G. Lu, J.R. Liu, P. Poole, P.J. Barrios, and X.P. Zhang, "Investigation of linewidth enhancement factor of InAs/InP quantum dot semiconductor lasers," SPIE Proceedings of the Photonics North 2010, Niagara Falls, Ontario, Canada, 250-bVay-291, 1-3 June 2010.

[7] J.R. Liu, Z.G. Lu, P.J. Poole, P.J. Barrios, D. Poitras, **Z.J. Jiao**, and Xiupu Zhang, "THz optical pulses from a coupled-cavity quantum-dot laser," *Opt. Commun.*, vol. 285, pp. 1323-1325, 2012.

[8] Z.G. Lu, J.R. Liu, P.J. Poole, **Z.J. Jiao**, P.J. Barrios, D. Poitras, J. Caballero, and X.P. Zhang, "Ultra-high repetition rate InAs/InP quantum dot mode-locked lasers," *Opt. Commun.*, Vol. 284, pp. 2323-2326 , 2011.

[9] Z.G. Lu, P.J. Poole, J.R. Liu, P.J. Barrior, **Z.J. Jiao**, G. Pakulski, D. Poitras, D. Goodchild, B. Rioux, and A.J. SpringThorpe, "High performance 1.52 μm InAs/InP quantum dot distributed feedback laser," *Electron. Lett.* vol. 47, pp. 818-819, 2011.

[10] P.J. Poole, Z.G. Lu, J.R. Liu, P. Barrios, **Z.J. Jiao**, D. Poitras, A.J. Springthorpe, G. Pakulski, D. Goodchild, and B. Rioux, "Narrow Linewidth 1.52 μm InAs/InP Quantum Dot DFB Lasers," the Proceedings of International Conference on InP and Related Materials (IPRM 2011), Berlin, Germany, 22-26 May, 2011.

[11] Z.G. Lu, P. J. Poole, J.R. Liu, P.J. Barrios, D. Poitras, **Z.J. Jiao**, G. Pakulski, J.A. Caballero, D. Goodchild, B. Rioux, and A.J. SpringThorpe, "InAs/InP quantum dot laser devices around 1550 nm for fiber communications," (invited paper), the Proceedings of the Information Photonics 2011, Ottawa, Ontarion, Canada, 18-20 May 2011.

[12] Z.G. Lu, P.J. Poole, P.J. Barrios, **Z.J. Jiao**, J.R. Liu, G. Pakulski, D. Goodchild, B. Rioux, A.J. SpringThorpe, and D. Poitras, "Single mode 1.52 μmInAs/InP QD DFB lasers," the Proceeding of Optical Fiber Communications (OFC) 2011, Los Angeles, CA, USA, OWD6, 6-10 March 2011

[13] Z.G. Lu, J.R. Liu, **Z.J. Jiao**, P. Poole, P.J. Barrios, D. Poitras, and J. Caballero, "Monolithic InAs/InP quantum dot mode-locked lasers with ultra-high repetition rates," IEEE Proceedings of the Photonics Global Conference 2010, Singapore, 10a588, 14-16 December 2010.

[14] Z.G. Lu, J.R. Liu, P. Poole, P.J. Barrios, D. Poitras, **Z.J. Jiao**, X.P. Zhang, A. Benhsaien, K, Hinzer, and T.J. Hall, "Noise properties of passively InAs/InP quantum dot mode-locked lasers with high repetition rate," SPIE Proceedings of the Photonics North 2010, Niagara Falls, Ontario, Canada, 250-mQW1-311, 1-3 June 2010.